Ph.D. Thesis

Doctoral Program in Aerospace Science & Technology

Contributions to ionospheric electron density retrieval

Angela Aragon-Angel

Advisors:
Dr. J.Miguel Juan Zornoza
Dr. Manuel Hernández Pajares
Research group of Astronomy and Geomatics (gAGE)
Depts. of Applied Mathematics IV and Applied Physics
Universitat Politècnica de Catalunya (UPC), Spain

September 10, 2009

Contents

List of Figures

List of Tables

Introduction

La ciencia es orgullosa por lo mucho que ha aprendido;
la sabiduría es humilde porque no sabe más
William Cowper

Research objectives

The research objectives of this Ph.D. disertation can be summarized in a very general one being to help in the analysis and implementation of tools in order to describe the vertical and global morphology of the ionospheric electron density by means of radio occultation retrievals. In order to achieve this goal, an improvement of the classical Abel inversion has been considered applied to the bending angles of the GPS carrier phase $L1$. The classical Abel inversion is a technique that, in the context of ionospheric retrievals, allows to obtain vertical electron density profiles from GPS observables. The use of such technique assumes that the electron density depends solely on height (spherical symmetry assumption) and can lead to important mismodelings. The main idea of improvement is the inclusion of horizontal gradients in the electron density description (separability hypothesis). With the implementation of separability to bending angles, an observable suitable for troposphere has been obtained, something that was not possible with former uses of the separability when applied to a combination of GPS carrier phase observables. As a result of this study, it has been also possible to define mapping functions associated to each solved radio occultation profile and to point out the importance of the protonospheric contribution.

LEO satellites and the radio occultation technique

Low Earth Orbit (LEO) satellites are generally defined to be up to an altitude of 2000 km above Earth's surface. Given the rapid decay of objects on the

lower altitude range due to the atmospheric drag, it is commonly accepted that a typical LEO height lies between 200 and 2000 km. The first LEO was launched in 1957 (Sputnik) and, from then on, several LEO missions have been orbiting the Earth. Nowadays, this kind of satellites are used in a wide range of fields, such as communications, remote sensing, gravimetric and magnetometric sounding, ocean altimetry, atmospheric retrieval and Search and Rescue alarm operations. Among these applications, atmospheric retrieval becomes crucial for our study. LEO satellites loaded with a GPS on board can be used as scanners of the atmosphere by mean of the Radio Occultation (RO) technique. Deriving ionospheric density profiles from RO measurements has become a useful tool to help determining and study vertical ionospheric 3D structures at global scale, overcoming the limitations of direct measurements, such as ionosonde and digisonde measurements, which can only provide profiles up to the maximum frequency and at localized places. Moreover, the recent deployment of the FORMOSAT-3/COSMIC constellation, 6 LEO (Low Earth Orbit) satellites with GPS receivers on board which could theoretically provide around 2,500 occultations per day, would allow for the first time ever global electron density monitoring (indeed, structures plus time evolution) with high resolution. These data are going to be used to derive a relationship for the effective height in terms of longitude, latitude and time in ordert to feed the mapping function mathematical expression.

Methodology

The methodology used in the development of this thesis consisted in five phases:

1. Identification and critical assessment of the separability concept to bending angles.

2. Identification and critical assessment of a potential improvement to current definitions of mapping fuctions.

3. Design of algorithms and methods implementing the proposed improvement to separability, clock drift removal and mapping functions.

4. Software implementation of the design.

5. Execution of tests using simulated and real data in a variety of cases for different LEO satellite missions, solar cycle epochs, to properly assess the proposed methodology.

The developed software tools have been written in Fortran, C-shell and gawk script under Linux architecture.

Thesis breakdown

This thesis consists on several chapters distributed as follows:

- Chapter 1, *The Global Positioning System*. Introduces the fundamental concepts of the main tool used in this Ph.D. thesis to sound the ionosphere: GPS.
- Chapter 2, *The ionosphere: characteristics and monitoring*. Contains a basic description of the ionosphere.
- Chapter 3, *Introduction to GNSS Radio Occultations*. Introduces the radio occultation technique from an historic point as well as the basic observables to use it.
- Chapter 4, *Mathematical principles of the Abel inverse transform and its application to GNSS RO*. Provides the mathematical tools to performe the classical Abel inversion and the adaptation needed to implement the separability approach to bending angles.
- Chapter 5, *Improved Abel transform inversion: Results*. Presents results of the new implementation of separability to bending angles. Results are compared with the classical approach for bending angles but also an intercomparsion of results using different input observables is provided.
- Chapter 6, *Upper Ionosphere estimation*. Describes several approaches to account for the upper plasmaspheric contribution to electron density derived from radio occultation events.
- Chapter 7, *Towards a mapping function derived from RO*. Introduces a way to derive mapping functions from a given radio occultation. A way to calculate associated heights is also presented. Consequences with respect the contribution of the protonosphere are also discussed.

Chapter 1

The Global Positioning System

Yo amo los mundos sutiles,
ingrávidos y gentiles
como pompas de jabón.
Me gusta verlos pintarse
de sol y grana, volar
bajo el cielo azul, temblar
súbitamente y quebrarse
Proverbios y cantares (I)- Antonio Machado

1.1 Introduction

In recent past years, Global Navigation Satellite Systems (GNSS), in particular, the NAVigation Satellite Timing and Ranging Global Positioning System (NAVSTAR GPS), have led to an increasing number of applications such as tropospheric and ionospheric sounding, precise navigation and timing among many others.

The Global Positioning System (GPS) satellite constellation was originally implemented to provide navigation and tracking information to the United States military branches throughout the world. Today, the GPS system can provide accurate, continuous, worldwide, three-dimensional position and velocity information to any user with the appropriate receiving equipment.

Descriptions of the GPS system can be found at [Wells (1987)], [Seeber (1992)], [Hoffmann-Wellenhof et *al.* (2004)] and [Parkinson and Spilker (1996)].

1.1.1 GPS system description

The GPS system is divided into three segments:

- *Space segment:* Consists of the GPS satellite constellation which is comprised of 24 satellites plus some on-orbit spares, evenly distributed within 6 orbital planes with an inclination to the equator of the Earth

of 55^o and equally spaced 60^o (see Figure 1.1). Their orbits are near-circular with a semi-major axis of about 4.1 times the Earth radii (nominal orbits of 20200km with respect the surface of the Earth). The orbital period is approximately 12 sidereal hours. This configuration guarantees a global 24-hour coverage with, at least, four satellites in view, which is the minimum number of satellites required to solve the position of a GPS receiver.

- *Control segment:* Consists of a network of ground stations, whose functions are:
  - Control and keep the status and configuration of the satellite constellation.
  - Predict satellites ephemeris and onboard clock evolution.
  - Keep the GPS time scale.
  - Periodical update of the navigation message broadcasted by the satellites.
- *User segment:* Consists of all the users of the system. The GPS receivers gather the GPS signal from the satellites and solve the navigation equations in order to obtain its own coordinates and clock error.

Figure 1.1: *The space segment includes the satellite constellation of 24 satellites.*

1.1.2 GPS signal

Each GPS satellite continuously broadcasts a set of square-wave codes by coherently modulating the phase of the carrier of the transmitted radio signal. These codes, which are unique to the broadcasting satellite, are pseudorandom and mutually orthogonal. The codes are also known as Pseudo Random Noise (PRN) codes and there are more codes than potential number of satellites, so each code identifies the satellite. They are used for ranging and for transmitting almanac and timing information. The mutual orthogonality property of the codes enables the receiver to isolate the received signals broadcast by a given satellite from all others by cross-correlation techniques, and to process in parallel the signals from all satellites in view of the receiver. The GPS satellites broadcast ranging codes on a pair of phase coherent L-band carriers, the $L1$ carrier at a frequency of 1575.4 MHz and $L2$ at 1227.6 MHz:

$$f1 = 154 \cdot 10.23\ MHz = 1575.42\ MHz$$
$$f2 = 120 \cdot 10.23\ MHz = 1227.60\ MHz$$

which correspond to approximate wavelengths of 19 cm (λ_1) and 24 cm (λ_2). These include an encrypted precision (P) code with a chip rate of 10.23 MHz on both carriers and the clear access or coarse acquisition (C/A) code at 1.023 MHz on the $L1$ carrier. The dual carriers are needed primarily to eliminate (or determine) the refraction effect from the ionosphere. For a microwave in the ionosphere, the refractivity is very nearly proportional to the local electron density and inversely proportional to the square of the carrier frequency. Therefore, the range and phase information received separately from the two carriers can be applied in concert to nearly completely decouple the ionospheric refraction effect by using this dispersive property of the ionospheric plasma. Newer versions of the GPS satellites forseen for the modernization of GPS, **GPS III**, will have an additional carrier at 1176.45 MHz ($L5$) and a C/A-like code also on $L2$. This will significantly improve receiver tracking operations using clear access ranging codes and increase the accuracy of the ionosphere calibration.

The resulting transmitted signal corresponds to expression 1.1, its schematic interpretation being shown in Figure 1.2.

$$\begin{aligned} S_{GPS}(t) = \; & A_c \cdot C(t) \cdot D(t) \cdot \sin(2\pi f_1 + \phi_c) + \\ & + A_p \cdot P(t) \cdot D(t) \cdot \cos(2\pi f_1 + \phi_{p1}) + \\ & + A_p \cdot P(t) \cdot D(t) \cdot \sin(2\pi f_2 + \phi_{p2}) \end{aligned} \tag{1.1}$$

In order to limit the precision of the position of civilian users calculated

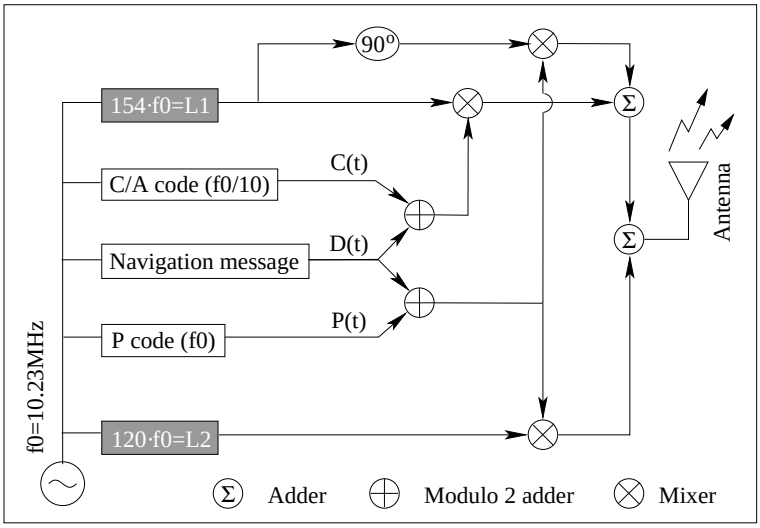

Figure 1.2: *Diagram of the GPS signal structure. Source [García-Fernández (2004)].*

by means of GPS, two modifications were applied to the GPS signal by the Department of Defense of Unites States:

1. *Selective availability* (*SA*) which consists of the intentional manipulation of the satellite clocks. The ephemerides contained in the navigation message are also modified. The resulting effect is an increase in the positioning error from 10m up to more than 100m approximately. On May 1st 2000, the SA was disconnected.

2. *Anti/Spoofing* (*AS*) which consists of the encryption of the precision P-code (into the Y-code) so non-authorized receivers are unable to use it, forcing these users to rely solely in the worse C/A code on f_1, and in an indirect and noisier estimate of a code on f_2.

1.2 GPS observables

In order to obtain the GPS observables that will be used for processing, the GPS receivers correlate (compare) the incoming signal with an internally generated copy. They basically measure the time or phase differences between both signals. If the differences are obtained from the PRN C/A or P codes (time differences) one will obtain the *Code Pseudorange*. Otherwise, by obtaining phase differences of the carrier frequency one will obtain *Phase pseudorange*. *Pseudoranges* are "ranges" because are an estimation of the

geometric distance between the satellite and the receiver (traveling time multiplied by the light speed gives *apparent* distance), and are "pseudo" because this range is not the actual geometric range since it is affected by a set of errors and delays. The *Code Pseudoranges* (expressed in units of length) can be modeled for both frequencies as:

$$\begin{aligned} P1_i^j &= \rho_i^j + c(dt_i - dt^j) + I_{f,i}^j + T_i^j + rel_i^j + K1_i^j + M_{P1,i}^j + \varepsilon_{P1,i}^j \\ P2_i^j &= \rho_i^j + c(dt_i - dt^j) + I_{f,i}^j + T_i^j + rel_i^j + K2_i^j + M_{P2,i}^j + \varepsilon_{P2,i}^j \end{aligned} \tag{1.2}$$

where,

- ρ_i^j is the geometric range between the satellite j and the receiver i at emission and reception time, respectively ($\sim$20000 km).
- c is the speed of light (299792458 m/s is the standard in GPS system).
- dt_i is the offset of the receiver i from GPS time (<300 km).
- dt^j is the offset of the satellite j from GPS time (<300 km).
- rel_i^j is the relativistic effect (<13m).
- T_i^j is the tropospheric effect (2-10m).
- $I_{f,i}^j$ is the ionospheric effect, which can be expressed in first order (more than 99.9% of the total effect) as: $I_{f,i}^j = \alpha_f \cdot STEC$ being $\alpha_f = 40.3/f^2$ (2-50 m) and STEC, the slant Total Electron Content i.e. the line-of-sight integrated electron density.
- K_i^j is the satellite and receiver instrumental delays, also called Total Group Delay or TGD (<2m).
- $M_{P,i}^j$ is the effect of multipath (<15m).
- $\epsilon_{P,i}^j$ is the thermal noise and other unmodeled sources of errors (3m).

Similarly, the *Phase Pseudoranges*, expressed in units of length as well, can be modeled as:

$$\begin{aligned} L1_i^j &= \rho_i^j + c(dt_i - dt^j) - I_{f,i}^j + T_i^j + rel_i^j + B1_i^j + w_{L1} + m_{L1,i}^j + \varepsilon_{L1,i}^j \\ L2_i^j &= \rho_i^j + c(dt_i - dt^j) - I_{f,i}^j + T_i^j + rel_i^j + B2_i^j + w_{L2} + m_{L2,i}^j + \varepsilon_{L2,i}^j \end{aligned} \tag{1.3}$$

where, apart from the notation introduced in the previous expressions, one can find:

- w_L is a term due to the relative rotation of the transmiting and receiving antennas. Known as wind-up, the direct consequence of this effect is that spinning the antenna is understood by the receiver as an apparent variation of distance between satellite and receiver (<20 cm).

- B_i^j is the ambiguity term, including the carrier-phase instrumental delays (∼20000 km), this value is kept constant while the receivers keeps track of the GPS satellite.

- $m_{L,i}^j$ is the effect of multipath. This effect is much smaller than pseudorange multipath (<2 cm).

- $\epsilon_{L,i}^j$ is the thermal noise and other unmodeled sources of errors. Also much smaller than pseudorange $\epsilon_{P,i}^j$ (<1 cm).

These terms are summarized in Table 1.1.

Geometric distance	ρ_i^j	$\simeq 20000km$
Receiver clock offset	dt_i	$< 300km$
Satellite clock offset	dt^j	$< 300km$
Ionospheric delay	I_i^j	1 to 50m
Tropospheric delay	T_i^j	1 to 20m
Relativistic effect	rel_i^j	$\simeq 10m$
Code Multipath effect	M	$0m - 3m$
Phase Multipath effect	m	$0cm - 5cm$
Code Noise	ε_P	$\simeq 3m(C/A)$
		$\simeq 30cm(P)$
Phase Noise	ε_L	$\simeq 3mm$
Wind-up effect (only phase)	w	$\simeq 200cm$
		per antenna rotation

Table 1.1: *Main contributions to Pseudoranges. The multipath errors are difficult to quantify since it highly depends on the environment. Additionally, the a priori broadcasted satellite position and clocks can cause an extra error of 2 m approximately.*

The term Bn_i^j in the phase pseudoranges is defined as $Bn_i^j = b_i + b^j + \lambda N_i^j$, thus including both instrumental delays and *integer ambiguity* term. Phase processing consists basically in measuring the accumulated difference between the incoming GPS signal and the receiver replica. Nevertheless it is not possible to measure the number of cycles between the GPS satellite and the

receiver at the instance of first observation (this unknown quantity is the integer ambiguity). As a consequence, when the receiver loses visibility with the GPS satellite (for instance due to a building or vegetation) and re-locks afterwards, the phase observable shows discontinuities known as *cycle slips* (an example of cycle slips in GPS signal is given in Figure 1.3).

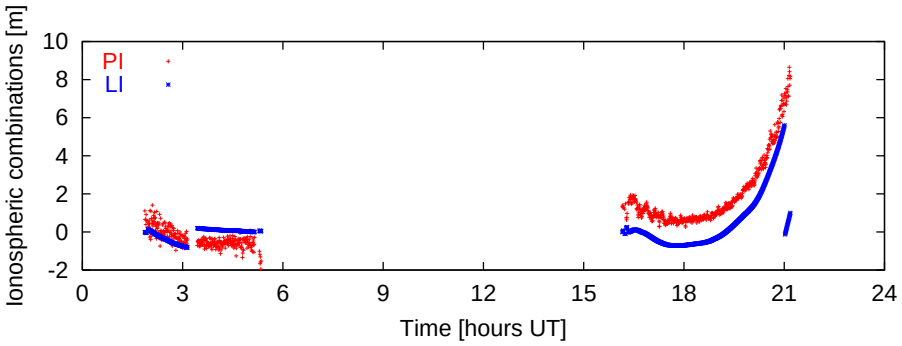

Figure 1.3: *Cycle slips in GPS signal using Ionospheric combination of observables (defined later, it contains essentially the ionospheric delay and the instrumental delays and the additional phase ambiguity term in the case of LI). Note that the phase observable is reinitialized whenever a cycle slip or new signal lock takes place. It can be seen as well that, although being ambiguous, the phase observable is much more precise than the code observable.*

The terms corresponding to clock bias (with respect to the GPS time scale) present large errors unless they are properly accounted for. In the case of the GPS receiver, since it commonly uses a simple quartz clock to generate the replica of the GPS signal, a larger clock bias with respect to the GPS time scale occurs. Therefore, four GPS satellites, at least, are going to be needed to estimate this bias along with the 3D position coordinates of the GPS receiver. In the case of the GPS satellite, satellite clock bias can be mostly corrected with the data included in the navigation message (D(t)). Further details of each pseudorange contribution can be found in [Hoffmann-Wellenhof et *al.* (2004)] and [Parkinson and Spilker (1996)].

Using these basic observables, it is possible to linearly combine them:

Free ionospheric combination (LC and PC): Taking into account that the ionospheric delay depends on the square frequency, it is possible to remove its effect by constructing this combination as follows:

$$Pc = \frac{f_1^2 \cdot P_1 - f_2^2 \cdot P_2}{f_1^2 - f_2^2} \qquad Lc = \frac{f_1^2 \cdot L_1 - f_2^2 \cdot L_2}{f_1^2 - f_2^2} \tag{1.4}$$

Obtaining:

$$Pc_i^j = \rho_i^j + c(dt_i - dt^j) + rel_i^j + T_i^j + M_{Pc,i}^j + \epsilon_{Pc,i}^j$$
$$Lc_i^j = \rho_i^j + c(dt_i - dt^j) + rel_i^j + T_i^j + Bc_i^j + w_{Lc} + m_{Lc,i}^j + \epsilon_{Lc,i}^j$$

This combination is basically used for navigation purposes in receivers that are able to process both GPS frequencies.

Narrow and Wide lane combinations (Pδ and Lδ respectively): The wide lane combination is used for cycle-slips detection since it provides with an effective long wavelength of λ_δ=86.2 cm, which becomes very useful for this purpose. The Lδ and the corresponding combination for the code are constructed as follows:

$$P\delta = \frac{f_1 \cdot P_1 + f_2 \cdot P_2}{f_1 + f_2} \qquad L\delta = \frac{f_1 \cdot L_1 - f_2 \cdot L_2}{f_1 - f_2} \tag{1.5}$$

Obtaining:

$$P\delta_i^j = \rho_i^j + c(dt_i - dt^j) + rel_i^j + T_i^j + \alpha_\delta I_i^j + M_{P\delta,i}^j + \epsilon_{P\delta,i}^j$$
$$L\delta_i^j = \rho_i^j + c(dt_i - dt^j) + rel_i^j + T_i^j + \alpha_\delta I_i^j + B\delta_i^j + w_{L\delta} + m_{L\delta,i}^j + \epsilon_{Lc,i}^j$$

Ionospheric (or geometric free) combination (LI and PI): It cancels all terms that do not depend on frequency such as geometric range, troposphere and so on, leaving the ionospheric contribution, instrumental biases and wind-up among others. This combination is constructed as follows:

$$PI = P_2 - P_1 \qquad LI = L_1 - L_2 \tag{1.6}$$

Obtaining:

$$PI_i^j = \alpha_I I_i^j + K_I{}_i^j + M_{P_I,i}^j + \epsilon_{P_I,i}^j$$
$$LI_i^j = \alpha_I I_i^j + B\delta_i^j - B2_i^j + m_{LI,i}^j + w_{LI} + \epsilon_{LI,i}^j$$

In order to respect the sign convention, the order of the observables are changed since the ionosphere causes a delay in the code and an advance in the phase in the same absolute amount (see Section 2.3). In ionospheric sounding the information given by the ionospheric (or geometric free) observable becomes essential, therefore the next section offers a deeper insight to this combination and the effect of ionosphere to GPS signals.

1.2.1 Ionosphere and GPS: L_I and P_I

As seen in Section 2.3, the STEC plays a key role in determining the delay caused by the ionosphere to electromagnetic signals. From expressions 2.8

and 2.9, a relationship between these quantities can be established:

$$I_{group} = \frac{40.3}{f^2} \cdot STEC \qquad I_{phase} = -\frac{40.3}{f^2} \cdot STEC \tag{1.7}$$

being f the frequency, expressed in Hz, the STEC in $electrons/m^2$ and the ionospheric delay I expressed in units of meters of ionospheric delay.

According to each pseudorange observable (Definitions 1.2 and 1.3) and the definition of the ionospheric combination (Equation 1.6), P_I and L_I observables can be modeled as:

$$\begin{aligned} P_I &= \alpha_I \cdot STEC + K_I + M_{P_I} + \varepsilon_{P_I} \\ L_I &= \alpha_I \cdot STEC + k_I + \lambda_1 \cdot N_1 - \lambda_2 \cdot N_2 + m_{L_I} + w_{L_I} + \varepsilon_{L_I} \simeq \\ &\simeq \alpha_I \cdot STEC + b_I \end{aligned} \tag{1.8}$$

where

$$\alpha_I = \alpha_2 - \alpha_1 = \frac{40.3}{f_2^2} - \frac{40.3}{f_1^2} \simeq 1.05 \frac{m_{L_I}}{10^{17} electron/m^2} = 10.5 \frac{m_{LI}}{TECU} \tag{1.9}$$

and b_I contains the contribution of both the instrumental delays and phase ambiguities. As done in [Blewit (1989)], the terms due to noise, multipath and higher-order ionospheric terms (whose error is less than centimeter) are not explicitly shown in the L_I expression, since the remaining terms are orders of magnitude larger.

Chapter 2

The ionosphere: basic characteristics and monitoring

Hay golpes en la vida, tan fuertes... ¡Yo no sé!
Golpes como del odio de Dios; como si ante ellos,
la resaca de todo lo sufrido
se empozara en el alma... ¡Yo no sé!
Los heraldos negros- César Vallejo

2.1 Morphology of the ionosphere

The atmosphere of the Earth is considered to be divided into several layers, one of them containing enough electrons and ions to effectively interact with electromagnetic fields, subjected to the laws of plasmaphysics that can be referred to as magnetoactive plasma, called ionosphere. The ionosphere of the Earth is a shell of electrons and electrically charged atoms and molecules that surrounds it, generally accepted that stretches from approximately 50 km of the surface of the Earth up to the start of the plasmasphere at around 1000 km.

The origin of the ionosphere is the ionization of several molecular species (O, H ...), being the most important the atomic oxygen (O, ionized to O^+), due to the ultraviolet (UV) and X radiation emitted by the Sun. Since the absorption of this UV radiation increases with decreasing altitude and the density of neutral atmosphere molecules increases towards the surface of the Earth, there is a maximum of absorption, implying a maximum of the concentration of ionization, which is typically found between 250 and 400 km height (depending on geophysical conditions). Considering that the ionosphere is neutrally charged (the overall charge of the ionosphere is zero) and, since the ionization of the oxygen generates a single electron, the number of electron can be considered approximately equal to the ions[1].

According to the ionization source, the ionosphere can be considered to be

[1]This consideration will allow us in Chapter 7 to propose Eq. 7.23 to account for the ionospheric electron density based on the most relevant constituent ions of the ionosphere

divided into several stratified layers (see Figure 2.1). From lowest to highest layer, the distribution is:

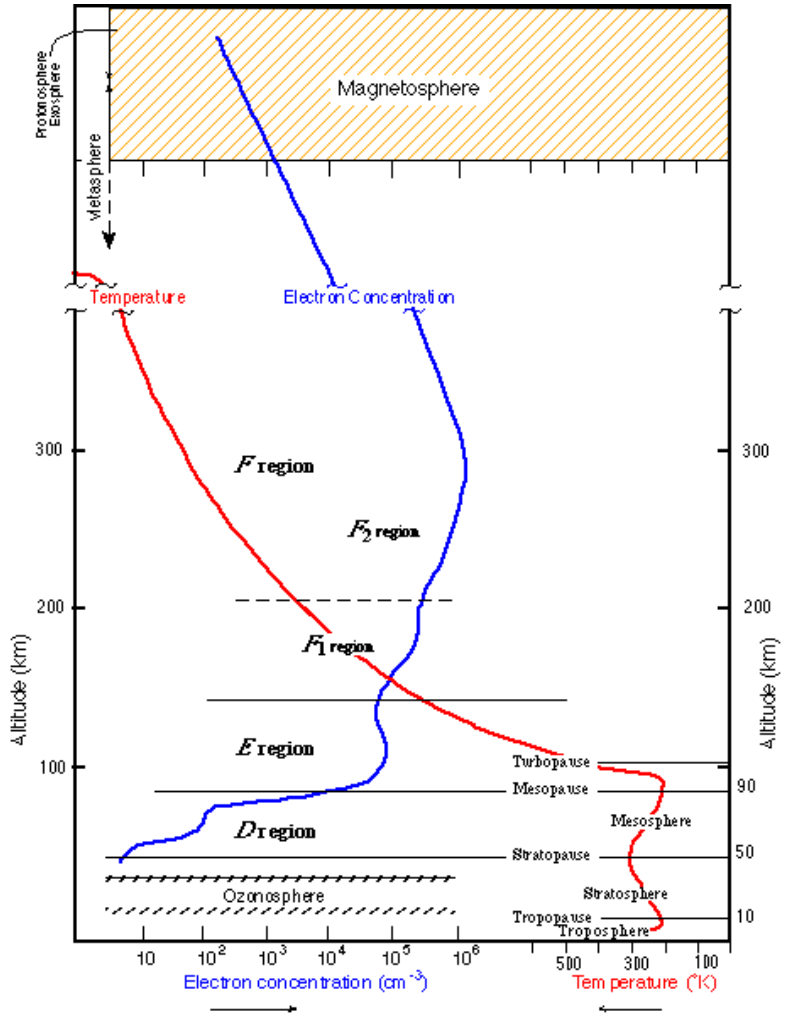

Figure 2.1: *Typical profile of electron density versus height. The corresponding temperatures at each given height are also indicated. E,D,F1 and F2 layers are pointed out. Courtesy of www.k1ttt.net.*

- *D layer*: from 60 to 90km, is basically generated by the hard solar and galactic X-rays. Within the D region, another layer can be formed controlled by the cosmic rays, the *C layer*.

- *E layer*: from 90 km to 130 km, is formed under action of the solar UV radiation (mainly, soft X-rays). During daytime, the behavior of

the E layer is very regular and controlled by the zenith angle of the Sun. During dusk and nighttime, its behavior becomes more complex. Its shape can be only a simple inflexion in the profile, but a valley usually appears, thus marking a local maximum. Inside the E region, very thin layers could be formed, the so called Sporadic E-layer (or E_s layer), showing sometimes large enhancements of electron density.

- *F layer* is the predominant layer in an electron density profile since it contains the majority of the electron density concentration. This layer is divided into two:
  - *F1 layer*: from 160 km to 200 km, which is more likely to appear during summer daytime conditions, and during nighttime it is the cavity (valley) between the E and F2 layers.
  - *F2 layer*: from 210 km to 1000 km. It is is the most dynamical and most dense (from the point of view of plasma density) layer of the ionosphere, containing the maximum of the whole electron density profile.

The electron density maximum ($NmF2$) constitutes the frontier between the Bottomside (lower part of the ionosphere) and the Topside (higher part of the ionosphere).

The electron density above 1000km is mixed up in the plasmasphere, where the majority of ions correspond to ionized H (H^+), hence its name, the protonosphere.

2.2 Variability of Ionosphere

Since the Sun is the main source of ionization of the ionosphere, any variation of the solar radiation or the relative geometry with respect to the Earth produce large dynamics in the electron content either in time and space.

- *Diurnal variation.* Due to the rotation of the Earth, the relative position of the Sun and Earth changes with time, following a daily cycle. This implies that the amount of ionization will be consequently dependent on this cycle.
- *Latitudinal variation.* The ionosphere shows certain behavior that are latitudinal dependent. In low latitudes, near the geomagnetic equator, the occurrence of the Appleton-Hartree anomalies (also known as Equatorial anomalies) take place. These anomalies are characterized

as a depletion of electron density in the geomagnetic equator and large enhancements in the vicinity of $\pm 20^o$. This phenomena is caused by the "*fountain effect*": the presence of an eastward electric field in the geomagnetic equator causes an upward plasma drift, which rises until the pressure and gravity force are high enough and the plasma come back sideways through the magnetic field lines to higher latitudes (tropical ionosphere). In mid-latitudes the variations are lower, but the high latitudes, specially the regions comprised between 60^o and 70^o (i.e. auroral regions) are characterized by short-term variations more important than the lower latitudes. In the auroral regions, an interaction between the geomagnetic lines and the solar particle precipitation takes place. When the geomagnetic field is connected with the southward interplanetary magnetic field, geomagnetic storms are generated after solar ejection events (Coronal Mass Ejection or CME). In the polar caps the variation of the zenith angle of the Sun is much more smaller than other regions, therefore the variations in the electron densities are consequently smaller, although still detectable.

- *Solar cycle variation.* Several measurements of the sunspot number, which is an indicator of the solar activity, show that there is a main periodicity of 11 years (see Figure 2.2 for the sunspot number evolution since year 1995). This periodicity can also be detected studying the variability of the electron density.

Irregularities in the Ionosphere

Besides the expected variations of the electron density mentioned above, there are other unpredictable phenomena related to the Sun activity that depart from the usual state of the ionosphere. An important case are the geomagnetic storms, which are generated by a coupling of the solar wind and the magnetic field of the Earth. This type of storms last from hours to several days and does not necessarily take place at a global scale. The typical geomagnetic storm starts with an abrupt change followed by a recovery period that can last days. Several geomagnetic indices (for instance the K_p, A_p and Dst parameters) allow to monitor the virulence and evolution of a geomagnetic storm [Davies (1990)].

Another type of irregularities are the Traveling Ionospheric Disturbances (TID). These are wave-like irregularities related to perturbations of the neutral atmosphere, and can be classified according to its horizontal wavelengths (from 100km to 1000km), speeds (between $50ms^{-1}$ and $1000ms^{-1}$) and periods (from minutes to hours). In [Hernández-Pajares et *al.* (2006)], a study

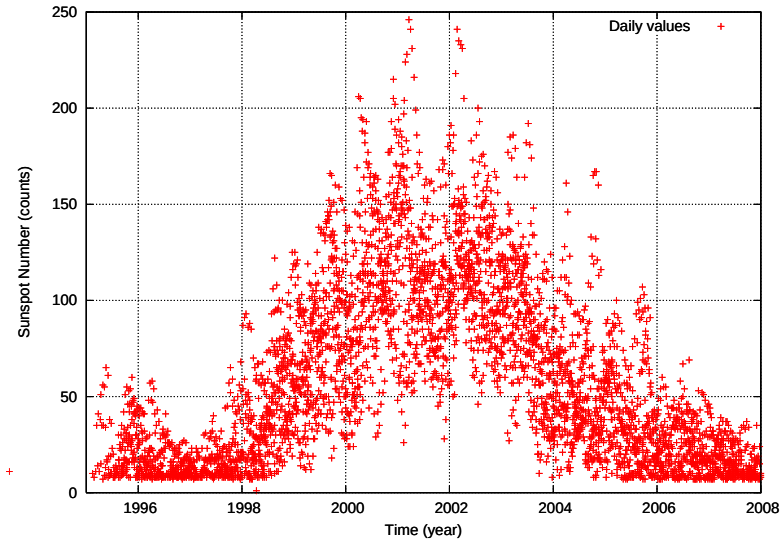

Figure 2.2: *Sunspot Number from 1995 to 2008. The Sunspot number is an indicator of the solar activity. Note that the last maximum was bimodal with maximums placed at mid 2000 and beginning of 2002, while the last minimum is presenting the lowest recordered solar activity. The plot depicts daily measurements of the Sunspot number.*

was presented showing the repeatability of Medium Scale TIDs characteristics, opening the door to simple ways of mitigation, by simple real-time modelling from the reference receiver observables themselves. Using a small network of receivers separated up to few tens of kilometers, well located (poleward-east oriented), were only necessary to estimate the specific MSTID parameters (velocity, propagation azimuth, period) for the network. Moreover, in [Hernández-Pajares et *al.* (2006)], climatological MSTIDs parameters were used to define a simple model (DMTID), capable to mitigate in real-time the MSTIDs effect in precise user navigation.

2.3 Ionosphere and electromagnetic signals

The presence of the ionosphere cause an effect on the electromagnetic signals that travel through it. Its effect will basically depend on the ionospheric free electron density due to its most efficient interaction with electromagnetic signal (caused by the fact that the electron has a very high ratio charge to mass). Another important feature of the effect of the ionosphere on radio signals is that this effect depends as well on the frequency of the signal that

traverses it (i.e. the ionosphere is a *dispersive medium*). This effect modifies the traveling speed of the signals with respect to the light speed, due to the presence of a refractive index different from 1. Depending whether one considers the group (where the information is carried) or the phase of the signal, this refractive index will be different. The following expression relates them both [Davies (1990)]:

$$n_{gr} = n_{ph} + f\frac{dn_{ph}}{df} \tag{2.1}$$

According to [Seeber (1992)] the phase refractive index can be approximated with a series expansion truncated after the quadratic term, therefore:

$$n_{ph} = 1 + \frac{c_2}{f^2} \tag{2.2}$$

Substituting expression 2.2 into relationship 2.1, the group refractive index is also obtained:

$$n_{gr} = 1 - \frac{c_2}{f^2} \tag{2.3}$$

The constant c_2 is a value that depends on the electron density and is defined in [Seeber (1992)] as:

$$c_2 = k \cdot N_e \qquad where\ k = -40.3\ m^3 \cdot s^{-2} \tag{2.4}$$

On the other hand, the range between an emitter (Tx) and a receiver (Rx) is expressed as:

$$s = c\int_{Tx}^{Rx}\frac{dl}{v} = \int_{Tx}^{Rx} ndl \tag{2.5}$$

Assuming n equal to one, the straight line path is obtained instead:

$$s_0 = \int_{Tx}^{Rx} dl \tag{2.6}$$

The ionospheric delay is defined then as the difference between the measured range s and the geometric range s_0:

$$I = s - s_0 = \int_{Tx}^{Rx} ndl - \int_{Tx}^{Rx} dl = \int_{Tx}^{Rx} (n-1)\cdot dl \tag{2.7}$$

According to the definition of n, two different values of ionospheric refraction will be obtained, one for phase and the other for group. Simplifying

the expression by considering the integration along the geometrical path (s_0) instead of the actual path (s), ionospheric contributions become:

$$I_{group} = \frac{40.3}{f^2}\int_{Tx}^{Rx} N_e \; ds_0 \qquad I_{phase} = -\frac{40.3}{f^2}\int_{Tx}^{Rx} N_e \; ds_0 \tag{2.8}$$

Therefore, the ionospheric effect is equal in value for phase and group but of opposite sign, that is an advance in phase and a delay in group.

At this point, the Slant Total Electron Content or STEC is defined as the integral of the electron density along the signal path, that is:

$$STEC = \int_{Tx}^{Rx} N_e \; ds_0 \tag{2.9}$$

The STEC is expressed in units of TEC Units (TECU), where 1TECU is defined as 10^{16} electron contained in a cylinder of cross section of 1 m^2 aligned with the ray path. Therefore the STEC quantities are in fact units of electrons per area unit (i.e. $electron/m^2$). If the STEC is in the vertical direction, one will have the Vertical TEC (VTEC, or simply TEC) instead of STEC.

2.4 Ionospheric measurements

2.4.1 Ionosonde

Since the early soundings of the ionosphere, ionosonde has been one of the most important instruments to obtain accurate description of the electron density distribution. This device relies in the fact that the signals under 20MHz are mainly reflected by the different layers of the ionosphere. The operation of this instrument consists in the emission and reception of signals from 0.1MHz to 30MHz in the vertical direction. Then, it measures for each frequency the travel time that took the signal to go upwards and downwards again due to the reflection of the ionosphere in the different layers.

The electron density present in the ionosphere defines the maximum frequency for which the signals are no longer reflected. This relationship is stated through the following expression:

$$f_c^2 = \frac{e^2}{4\pi^2\epsilon_0 m_e} \cdot N_{max} \tag{2.10}$$

where e is the charge of the electron, m_e the mass of an electron and ϵ_0 the permittivity of free space. The electron density (N_{max}) is expressed in

electrons per cubic meter and the critical frequency (f_c) is in units of Hertz. If the signal has a larger frequency than the critical frequency of the layer (f_c), it will not reflect the signal and therefore it will pass to a denser layer. When the critical frequency of the F2 layer is reached (it corresponds to the maximum of electron density or NmF2), signals with greater frequency will not be reflected anymore and will travel to the outer space (therefore the travel time measured by the ionosonde will be infinite).

With the travel time it is possible to obtain the apparent height of the ionized layer (*virtual height*), defined as:

$$h' = \frac{c\tau}{2} \tag{2.11}$$

where τ is the travel time and c is the speed of light. This height is not real but virtual since the pulse is mainly affected by the ionized layers, instrumental delays and neutral atmosphere. The plots of virtual height against frequency are called *ionograms*.

With the ionogram and the relation 2.10 it is possible to obtain the electron densities of the different layers from the critical frequencies measured by the ionosondes, whose accuracy depends on various factors (see for instance [Piggot and Rawer (1978)] or [World Data Center-A (2003)]): (1) Inherent accuracy of the equipment, (2) accuracy of calibration method and (3) reading accuracy in the reduction of ionograms. The levels of accuracy of the ionosonde measurement of critical frequencies used in this work thesis are better than 5%.

One of the limitations of this instrument is that is not possible to obtain direct measurements of neither the valley between the maximum of the E-layer and the F-layer nor the topside ionosphere (i.e. measurements above the peak of the F2 layer).

Moreover, although the value of the virtual heights offers an orientation about the distribution in height of the ionospheric layers, it is desirable to have the profile of electron density referred to real height or, at least, the principal parameters such as the real height of the F2 layer peak (i.e. hmF2).

M(3000)F2 and hmF2

With the parameters provided by the ionosonde it is possible to apply straightforward expressions to obtain an estimation of the real height of the F2 layer peak using the M(3000)F2. This parameter is the maximum usable frequency for transmissions up to 3000km divided by the foF2 frequency (critical frequency of the F2 layer). In [Shimazaki (1955)] it was introduced

a semi-empirical relation to compute an estimation of the hmF2, expressed in km, based on this parameter:

$$hmF2_{Shimazaki} = \frac{1490}{M(3000)F2} - 176 \qquad [km] \tag{2.12}$$

In fact, this value is an estimation of the hmF2 based on the assumption that the profile of electron density follows a parabola, but the departures to this assumption cause an important mismodelling. Further works ([Bradley and Dudeney (1973)],[Bilitza et *al.* (1979)] and [Dudeney (1983)]) developed more accurate estimations based not only on the M(3000)F2 parameter, but on the ratio between the critical frequencies at the F2 and E layers. In particular, it is possible to obtain an estimation of the hmF2 with an accuracy of 4% or 5% ([Dudeney (1983)]) for good quality ionograms using the following expression:

$$hmF2_{Dudeney} = \frac{1490 \cdot F}{M(3000)F2 + \Delta M} - 176 \qquad [km] \tag{2.13}$$

where

$$F = M(3000)F2 \cdot \sqrt{\frac{0.0196 \cdot M(3000)F2^2 + 1}{1.2967 \cdot M(3000)F2^2 - 1}}$$

and

$$\Delta M = \frac{0.253}{\frac{foF2}{foE} - 1.215} - 0.012$$

being M(3000)F2, foF2 and foE the maximum usable frequency at 3000km divided by the foF2 (thus is an adimensional quantity) and the critical frequencies at the F2 and E layers (both expressed in MHz). Since the E layer is basically a diurnal layer and is difficult to measure during night using ionosonde, several authors apply conditions to this expression in order to obtain reliable values for the hmF2 parameter (see [McNamara et *al.* (1987)] or [Rishbeth et *al.* (2000)]). In particular, [Rishbeth et *al.* (2000)] imposes two conditions:

1. $M(3000)F2 > 2.5$
2. $foF2/foE > 1.7$

This condition diminishes the number of hmF2 values, specially during night periods. It is generally accepted (see for instance [Zhang et *al.* (1999)])

that the expected error in the hmF2 estimation using the Dudeney formula is between 20 and 30km.

The strength of these expressions rely in their straightforwardness. Therefore, since the number of ionosondes, and consequently the number of measured ionospheric parameters, has been increased during the last decades, it is possible to obtain, with a certain degree of sparsity, a high amount and world wide distributed values for hmF2. This allows performing studies about the morphology and temporal trends of the hmF2 parameter (see for instance [Rishbeth et *al.* (2000)] or [Marin et *al.* (2001)]).

True height profiles

The knowledge of the virtual heights is interesting for the applications that use the ionosphere for long-haul communications. Nevertheless, for the description of the ionosphere, it is more than interesting to have the whole vertical profile of electron density referred to real heights rather than virtual heights, at least up to the hmF2. This problem requires an inversion of the raw ionogram given by the ionosonde by applying the *true height analysis*. Tools such as POLAN ([Titheridge (1998)]) or the "μ'fitting" technique ([Tsai et *al.* (2001)]) are more complex approaches than the M(3000)F2 expressions, but allow to process ionogram data, expressed in function of virtual height, to obtain vertical profiles of electron density expressed in function of true height.

The true height analysis consist in the following process: The travel time corresponding to the lowest layers is almost unaffected by the ionization, therefore the deduced virtual height will be almost equal to the real height. As the frequency increases, the electromagnetic pulses will penetrate to denser layers, therefore the amount of ionization will be larger and the differences between the real and virtual height will increase as well. To invert from virtual to real height is necessary to reconstruct the ray in its travel through the ionosphere. To correctly perform this reconstruction is necessary to model (1) at which altitude the electron density becomes significant (*Starting position*) and (2) the valleys between layers that the ionosondes are unable to monitor (*Valley approximation*). These approximations can be performed, for instance, based on the geographical location of the ionosonde and epoch of measurement.

The POLAN method is considered to offer a high degree of accuracy in the true-height profiles, despite their high computational load. Depending on the quality of the ionograms it is generally accepted that the inaccuracies of those methods can be up to 20-30 km. Regarding the inter-comparison between the Dudeney formula and POLAN method, [McNamara et *al.* (1987)] reported

a discrepancy of 10-20 km between these two techniques in the estimation of the hmF2 parameter.

2.4.2 Global ionospheric maps of VTEC

During the recent past years, the availability of a huge number of widely distributed dual frequency GPS receivers over the surface of the Earth has made possible the capability of using such network as a global monitor of the ionosphere by means of computing Global Ionopsheric Maps (GIMs) using such ground GPS data.
On June 1st, 1998, the International GPS Service (IGS) started a project with the aim to compute GIMs with GPS data. Several centers were involved in such computation becoming the so-called Ionosphere Associate Analisys centers (IAACs): CODE (University of Berne, Switzerland), ESA/ESOC (European Space Agency/European Space Operation Center of ESA, Darmstadt, Germany), EMR (Energy, Mines and Resources/NRCan, Otawa, Canada), JPL (Jet Propulsion Laboratory, Pasadena, U.S.A) and UPC (Technical University of Catalonia/gAGE, Barcelona, Spain). On one hand, this working group was mainly created with the aim to compute GIMs with a resolution of 2h x 5^o x 2.5^o in Universal time, longitude and latitude on a daily basis. On the other hand, their task was also to compute accurate sets of GPS satellite hardware differential code biases (DCB) values. Another related goal adopted by IGS was to combine the different Ionospheric maps produced by each IAAC in order to get a common IGS GIM. In this context, new tools to validate GIMs were needed to stress out the differences among the global IAACs ionospheric estimations. As a result, a study with the first 3 years of continuous data [Orus et *al.* (2003)] showed significant intercenter biases. These results suggested the need to improve the different IAACs GIM estimation algorithms in order to fruitfully combine the different computations into a common IGS GIM. The combined product started to be computed at UPC on December 15th, 2002, in a test mode, and after the required validations, the official combined IGS GIM began to be delivered during May 2003. Since this date, users can have an official final IGS GIM with 10 days of latency. As techniques improve and computer capabilities increase, the IGS global VTEC maps can now be computed as well with latencies better than 24 hours (rapid IGS ionospheric products, [Komjathy and Hernández-Pajares (2004)]). The typical error of these maps (compared with external data, in this case of VTEC measurement provided by the TOPEX satellite) is of 15% approximately at northern mid-latitudes (see [Orus et *al.* (2002)] and [Orus et *al.* (2003)]).
An example of GIM maps is shown in Figure 2.3. It can be seen the variation

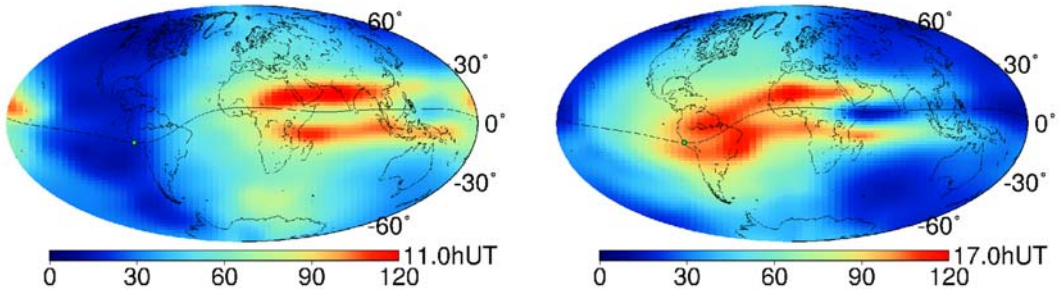

Figure 2.3: *Example of the variability of the electronic distribution around Jicamarca location (marked with a green point): two Global Ionospheric Maps in IONEX format computed and distributed by the Technical University of Catalonia for the day May 16, 2007. On the left, map corresponding to 11h UT. On the right, map corresponding to 17h UT.*

introduced by the rotation of the Earth as well as the latitude dependence, specially the large enhancements of VTEC of the equatorial anomalies above and under the geomagnetic equator.

The IGS GIMs are mainly used in scientific applications such as ionospheric altimeter calibration, ionospheric monitoring to improve and develop theoretical models such as the International Reference Ionosphere (IRI, [Bilitza, 2001]) or the NeQuick model [Hochegger et al., 2000] that will be introduced in Section 2.4.3, to provide navigation users with VTEC information (this type of data allows to correct most part of the ionospheric effect on the GNSS signal and to obtain better precision when positioning), and, most important for this Ph.D. thesis, to help improving the inversion of radio occultation data to obtained more accurate ionospheric electron densities [Aragon-Angel et *al.* (2009)].

VTEC interpolation

In order to obtain the VTEC at a given position from a GIM provided in IONEX format, it is necessary to perform a spatial/temporal interpolation from the IONEX grid at that given position. One way to proceed is to performe the interpolation between the nearest two *rotated* VTEC maps as explained in [Schaer et *al.* (1998)]. This rotation is related with respect to the Z-axis by a figure related to the time difference between the interpolation time and the map epoch. Essentially, it consists of an interpolation in local time instead of longitude, which implies a minimization of the interpolation

error due to the variability in longitude. This is justified by the significant stationarity of the electron content with respect to a Sun fixed reference frame. The interpolated VTEC follows the expression:

$$VTEC(\lambda,\phi,t) = \frac{T_{i+1}-t}{T_{i+1}-T_i} VTEC_i(\lambda'_i,\phi) + \frac{t-T_i}{T_{i+1}-T_i} VTEC_{i+1}(\lambda'_{i+1},\phi) \tag{2.14}$$

where $T_i \leq t < T_{i+1}$ and $\lambda'_i = \lambda + (t - T_i)$, which is the rotation to be applied to each map in order to obtain the *rotated* TEC maps. This expression can be derived from considering equal local times:

$$LT = T + \lambda = LT' = T_i + \lambda'_i \tag{2.15}$$

$VTEC_i(\lambda',\phi)$ corresponds to the nearest *rotated* TEC map (i.e. the map at epoch T_i). The VTEC value for a given latitude and longitude within a map corresponds to a distance weighting of the nearest 4 grid points (see [Schaer et *al.* (1998)]). The interpretation of such interpolation scheme is as follows: For a given latitude ϕ, the VTEC is the average value between the VTEC corresponding to the coordinates $\lambda + (t - T_i)$ at epoch T_i and the one corresponding to $\lambda + (t - T_{i+1})$ at epoch T_{i+1}. A graphical interpretation of this expression is provided in Figure 2.4.

2.4.3 Ionospheric Models

Climatological models become very useful to test ionospheric algorithms since they can provide with a controlled environment in which ionosphere is simulated. With such simulated environments, the underlying difficulties of data from real scenarios are not faced. Among these problems, basically, sparsity of data and instrumental delays are encountered.

IRI

This climatological model comprises several height profiles for a group of plasma parameters: plasma density, plasma temperatures of electrons and ions and ion composition [Bilitza et *al.* (1979)]. The plasma parameters and $M(3000)F2$ (from which $hmF2$ is derived) are obtained from a series of global coefficients: CCIR $foF2$ and $M(3000)F2$ Model Maps [Comité Consultatif International des Radiocommunications (1967)]. The CCIR $foF2$ and $M(3000)F2$ Model Maps consist of a data set containing the coefficients for the $foF2$ and $M(3000)F2$ models recommended by the Comité Consultatif International des Radiocommunications (CCIR), where

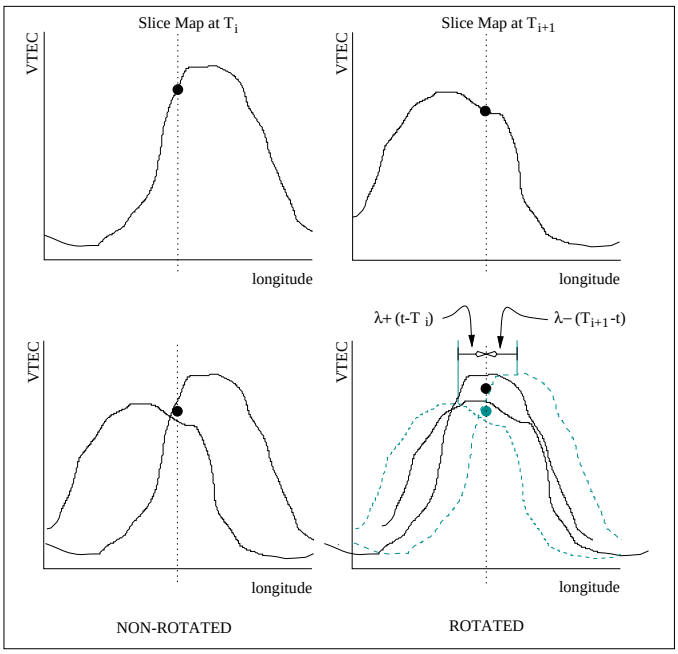

Figure 2.4: *(Upper) VTEC versus longitude (for a fixed latitude) for maps at T_i and T_{i+1}. (Lower) Interpolation at the desired longitude. (Lower-left) Interpolation without rotation, in this case the rotation of the Earth increases the interpolation error. (Lower-right) Interpolation with rotation, the stationarity of the ionosphere in a Sun fixed reference frame aids to decrease the interpolation error.*

$foF2$ is the F2-peak plasma frequency, which is related to the F2-peak density $NmF2$ by:

$$NmF2 = 1.24 \cdot 10^{10} \cdot foF2^2 \tag{2.16}$$

being $NmF2$ expressed in $\frac{e}{m^3}$ and $foF2$ in MHz. Both parameters, $foF2$ and $M(3000)F2$, are routinely scaled from ionograms. The CCIR maps are based on monthly median values obtained by the worldwide network of ionosondes (about 150 stations) during the years 1954 to 1958, altogether about 10000 station-months of data. Following a numerical mapping procedure developed in [Jones and Gallet (1965)], each station data set is first represented by a Fourier time series (in Universal Time), and then a worldwide development in a special form of Legendre functions (in geodetic latitude, longitude, and modified dip latitude) is applied for each Fourier coefficient. Coefficients sets are provided for high and low solar activity. For intermediate levels of solar activity, a linear interpolation is suggested. The whole CCIR model consists of $(988 + 441) \cdot 2 \cdot 12 = 34296$ coefficients, presented into twelve files, each

corresponding to one month within the year.

Standard NeQuick model

The climatologic ionospheric NeQuick model (see [Hochegger et *al.* (2000)]) is an empirical model of the ionosphere that generates profiles of electron densities based on parameters extracted from ionograms, that anchor the model. One of the particularities of this model is that it does not rely on Chapman profiles to construct the topside ionosphere, but uses semi-Epstein functions to model it. NeQuick is capable to reproduce TEC along a given ray path as well as electron density distributions for a given month, geographic latitude and longitude, height and UT, giving the potentiality for ground-satellite as well as satellite-satellite link corrections. As commented above, the model uses the Epstein formulation for the bottom side ionosphere and a simple formulation (Semi-Epstein layer), with a thickness parameter increasing linearly with height. NeQuick is also based on the CCIR coefficients. The two major components of the model are:

- The bottom side model for the height region below the peak of the F2-layer.
- The top side model for the height region above the F2-layer peak.

It also requires the monthly mean of solar radio flux at about 10 cm wavelengths (F10.7) as an additional input parameter. The F10.7 index is a measure of the solar activity, the noise level generated by the sun at a wavelength of 10.7 cm at the Earth's orbit. It has been found to correlate well with the sunspot number (Rz). The sunspot number is defined from counts of the number of individual sunspots as well as the number of sunspot groups. The F10.7 index can be measured relatively easily and quickly and has replaced the sunspot number as an index of solar activity for many purposes. It can be used as a daily index or averaged over longer periods (typically averaged over a month or a year although sometimes a 90 day average is made) to trace out the trends in solar activity. The correlation between these quantities is evident but there is still considerable scatter even for monthly-averaged values. The following equations are useful for converting between the F10.7 index ($F10.7$) and sunspot number (Rz). The equations are valid on a statistical (i.e. average) basis.

$$F10.7 = 67.0 + 0.572 \cdot Rz + (0.0575 \cdot Rz)^2 - (0.0209 \cdot Rz)^3 \tag{2.17}$$

$$Rz = 1.61 \cdot FD - (0.0733 \cdot FD)^2 + (0.0240 \cdot FD)^3 \tag{2.18}$$

where, $FD = F10.7 - 67.0$. A full description of the model can be found in [ITU-R (2000)] as well as the NeQuick model source code.

Regarding the advent of the forthcoming Galileo satellite system, currently being built by the European Union (EU) and the European Space Agency (ESA), the Nequick model has been chosen to generate the ionospheric correction coefficients for the Galileo navigation message. For this reason, a procedure has been designed and should be followed, as proposed by AG-IONO expert team. A description of such procedure is given in Appendix A with an analysis of the expected performance. This work was developed during the stay of the Ph.D. candidate at the European Space Research and Technology Centre (ESTEC) - ESA while performing doctoral research.

Chapter 3

Introduction to GNSS Radio Occultations

Dicen que no hablan las plantas, las fuentes y los pájaros.
Lo dicen pero no es cierto.
Rosalía de Castro

3.1 Introduction

In recent times, the Radio Occultation technique (RO) has become a widely used tool to probe the atmosphere of the Earth, helping in characterizing its most important physical properties, such as pressure, temperature and electron density profiles among others. RO commonly refers to a sounding technique in which a radio signal from a transmitting satellite passes through a planetary atmosphere before arriving at the receiver satellite. Under this configuration, the geometry involving the transmitter, the receiver and the planetary atmosphere changes within time. The use of the RO technique by means of spacecrafts to sound planetary atmospheres began with the first spacecraft to Mars in 1964, Mariner 4, which flew along a trajectory that passed behind Mars (when viewed from Earth) [Kliore et *al.* (1964)] [Fjeldbo et *al.* (1971)]. The word RO has recently become in use for satellite-to-satellite sounding through the atmosphere and, in particular, the ionosphere and the troposphere. From the point of view of the receiver, the transmitter is seen to be either rising or setting with respect to the limb of the occulting planet. As the radio wave from the transmitter passes through the atmosphere, its velocity and direction of propagation are altered by the medium refractivity gradient. The phase and amplitude of the wave at the receiver are consequently altered relative to the measurements that would be tracked without the in-between medium or the occulting planet. As time evolves, profiles of the phase variation and the amplitude variation at the receiver are generated and recorded by the receiver. These profiles provide information about the varying refractive properties of the medium that the signal has just gone through.

3.2 Radio occultations involving Earth satellites

The sounding of the atmosphere and ionosphere of the Earth using the RO technique could theoretically be performed with any pair of transmitter and receiver on board satellites following very few requirements. Prior to GPS becoming operational, a few early RO experiments from a satellite-to-satellite tracking link had been conducted. These included the radio link between GEOS-3 and ATS-6 [Liu et *al.* (1978)] and between the Mir station and a geostationary satellite [Yakovlev et *al.* (1996)]. Nevertheless, this Ph.D. thesis mainly focuses on the carrier phase observables measured by a GPS receiver onboard a low Earth orbiting satellite (LEO) while tracking the signals emitted by a GPS satellite during its occultation by the limb of the Earth. The first ever occultation experiment using GPS was carried out by the GPS/MET (Global Positioning System/Meteorology), an occultation experiment on MicroLab-1. GPS/MET (launched on April 3rd, 1995 and decommissioned in March 1997) had a circular orbit at 730 km of altitude and 60^o of inclination. Although experimental, over 11000 occultations from the whole GPS/MET life time helped recovering refractivity, density, pressure, temperature, and water vapor profiles [Hajj and Romans (1998)] as well as performing ionospheric tomography [Hernández-Pajares et *al.* (1998)]. GPS/MET provided a definitive proof-of-concept of the occultation technique. Since then, many other missions have gathered useful occultation data, such as the Challenging Minisatellite Payload (CHAMP) (2001) and Satellite de Aplicaciones Cientificas-C (SAC-C) (2001), which have contributed with more than 400 daily occultations [Hajj et *al.* (2004)], and Gravity Recovery and Climate Experiment (GRACE) (2002) with around 140 during its active periods. The successful deployment of the the Constellation Observing System for Meteorology, Ionosphere and Climate (FORMOSAT-3/COSMIC) [Lei et *al.* (2007)], which started in April 2006, is currently providing sets of occultation data distributed globally and almost uniformly, thus overcoming two limitations of previous LEO missions: sparcity and scarcity of occultation data (FORMOSAT-3/COSMIC yields about 2000 daily occultations [Anthes et *al.* (2008)]). Moreover, the Russian Global Navigation Satellite System (GLONASS), and future systems, such as the European constellation Galileo, will broaden the current scenario for dedicated satellite-to-satellite occultation missions.

Figure 3.1 depicts in a non-scaled plot a typical occultation scenario involving a LEO and a GPS satellite. For a setting occultation, the about-to-be occulted GPS satellite will be seen from the LEO to be setting with respect

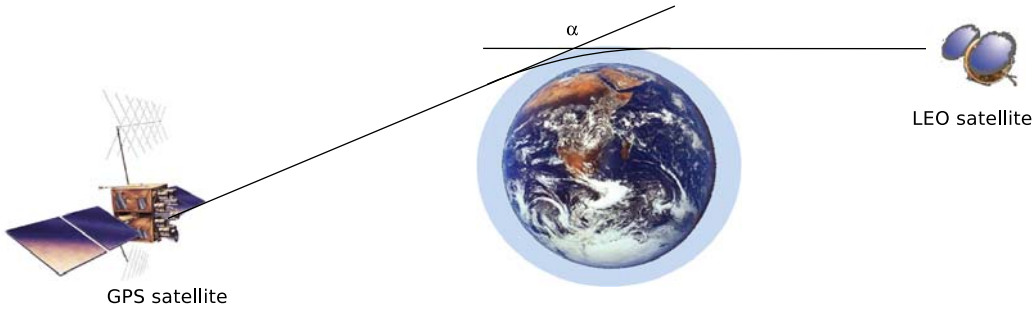

Figure 3.1: *RO geometry.*

to the limb of the Earth. The duration of a typical analyzed occultation through the ionosphere (starting from the LEO altitude to roughly 100 km above the surface of the Earth) is of several minutes. A ray from the GPS satellite passes through the upper layers of the atmosphere of the Earth at a near-horizontal rate of descent, skimming a deepest layer at its tangency point. After the tangency point, the ray begins its near-horizontal rate of ascent through the upper layers, exits the atmosphere, and continues on to the LEO satellite. A very clarifying example is with regard the sun and its shape: At sunset, the apparent sun for an observer on the ground is refracted through its own diameter, about 0.5^o. The secular trend in the refractive gradient of dry air with altitude (which is near-exponential) is evident in the oblate shape of the apparent sun as its lower limb touches the horizon. Rays from the bottom limb usually are bent more than rays from the top limb. The fractured shape of the solar disk at some sunsets is caused by abrupt departures of the refractivity profile at low altitudes from the secular trend. In fact, the sun is below the horizon when is still seen abouve it. The ray arriving at the LEO from the occulted GPS satellite is not necessary unique in the sense that there can be many different possible rays in the same way to the receiver, and might not even exist in a geometric optics context [Melbourne (2004)]. But for practical matters, we will assume in Figure 3.1 that it exists and that it is unique at the epoch of the observation. As time evolves, the tangency point of the ray arriving at the LEO drifts deeper into the atmosphere for a setting occultation. The excess phase delay observed at the LEO, which is simply the extra phase induced by the refracting medium, will continue to increase over the course of the occultation because of the increasing air density with depth or electron density variation with height in the ionosphere. This will end when the tangency point of the ray gets near the planetary surface. In the lower troposhere (which is not the aim of our study), defocusing and multipath reduce the signal am-

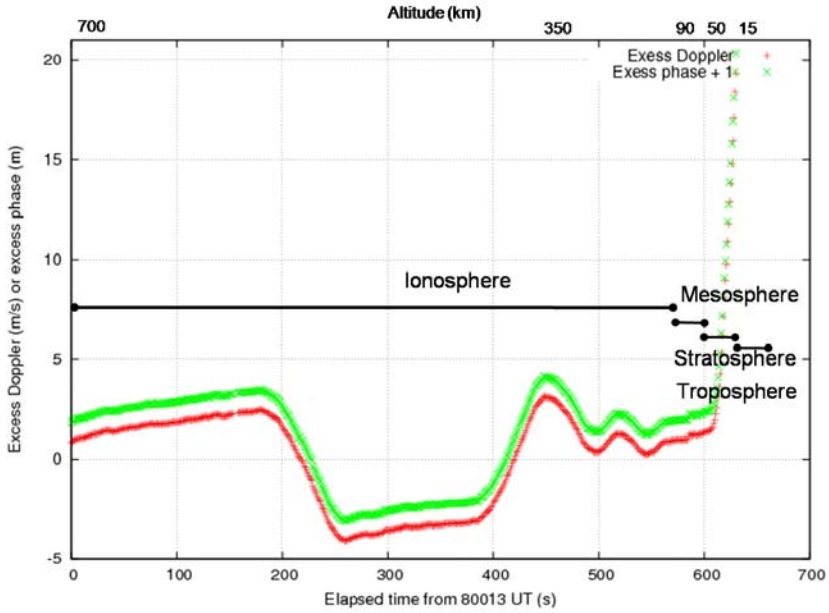

Figure 3.2: *Profile of excess Doppler and phase for a FORMOSAT-3/COSMIC RO during January 7^{th}, 2007, PRN 27, LEO l261 around 22 h UT. Redrawn from [Melbourne (2004)].*

plitude below a detection threshold, finishing the RO episode prematurely [Pavelyev et *al.* (1997)]. But these cases happen at much lower heights than the bottom of the ionosphere limit (> 50 km).

Figure 3.2 shows results from a typical occultation from FORMOSAT-3/COSMIC. The excess phase delay of the $L1$ carrier phase is depicted in meters and its time derivative, the excess Doppler in meters per unit of time, for the duration of a whole RO event. The lower abscissa shows elapsed time from the Universal starting time of the RO. The upper abscissa shows the altitude of the ray path tangency point. It can be seen that for the lowest altitudes, the refractive gradient of the atmosphere (stratosphere and troposphere) increases with depth, slowing down the average rate of descent of the tangency point because the refractive bending angle of the ray increases with depth. Consequently, the LEO satellite must travel farther along its orbit to intercept these progressively deeper penetrating and more refracted rays.

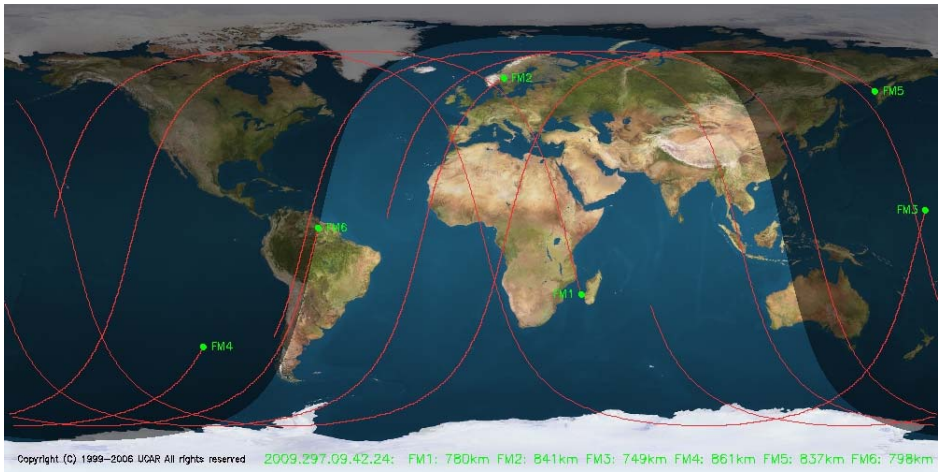

Figure 3.3: *FORMOSAT-3/COSMIC satellite locations for October 24th, 2009, at 09:42:24 UT. Each satellite is located at a different height: FM1 at 780 km, FM2 at 841 km, FM3 at 749 km, FM4 at 861 km, FM5 at 835 km and, FM6 at 798 km. Courtesy of UCAR.*

3.2.1 FORMOSAT-3/COSMIC constellation

The joint Taiwan-US mission FORMOSAT-3/COSMIC was launched on April 17th, 2006, deploying six micro-satellites (see Figure 3.3), approximately 62 kilograms of weight (including fuel), with a circular orbit at altitudes ranging from 700 to 800 km and with inclination angle of 72^{o} in the final mission phase.

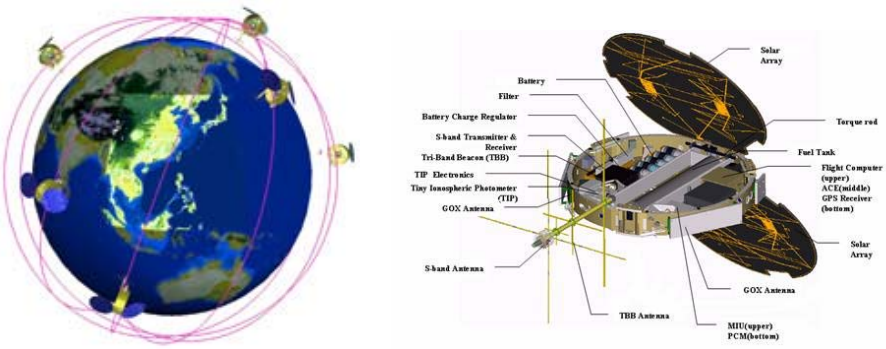

Figure 3.4: *On the right, the FORMOSAT-3/COSMIC constellation. On the left, the FORMOSAT-3/COSMIC spacecraft and payloads. Courtesy of NSPO.*

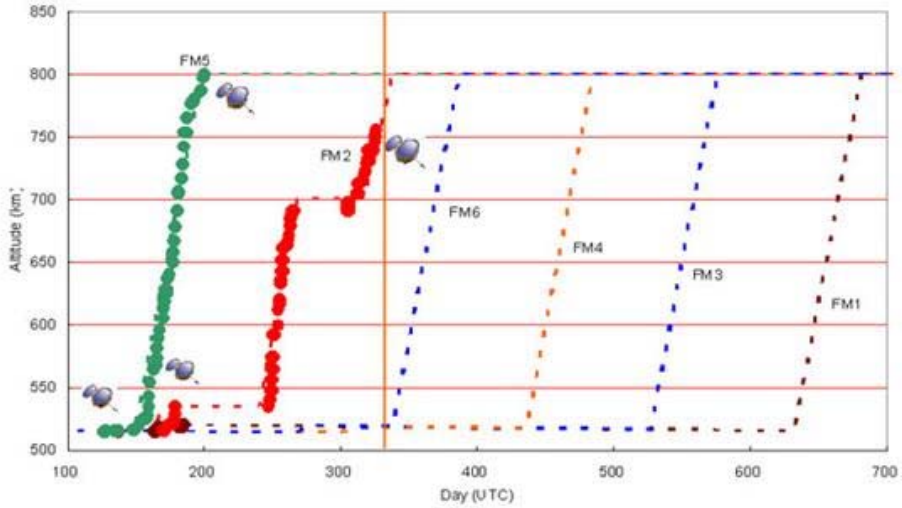

Figure 3.5: *Orbit maneuver schedule for FORMOSAT-3/COSMIC. The day is counted since January 1st, 2006. Courtesy of NSPO.*

The design lifetime is 5 years. Each of the satellites is equipped with a GPS receiver, a tiny ionospheric photometer (TIP) and a tri-band beacon (TBB). The GPS receiver has four antennas installed on the front and back faces of the satellite main frame, which is a ring (see right-hand plot in Figure 3.4). Two single-patch antennas, mounted on the upper part of the main body, are for precise orbit determination (POD). The other two antennas, dedicated to atmospheric occultation research, are mounted on the lower part. Updated and useful information about the status and data acquisition is available at the web site of Taiwan's National Space Organization (NSPO): http://www.nspo.gov.tw.

According to the orbit maneuver schedule given in Figure 3.5, some FORMOSAT-3/COSMIC satellites will stay at a lower altitude of 525 km for about one and a half years before starting raising to the final altitude of 750 km (one satellite) and 800 km (5 remaining satellites). By combining low (525 km) and high (750 to 800 km) orbits, gravity determination can be fulfilled: The lower orbits will be more sensitive to the higher frequency gravity component than the higher ones, but the former will experience a relatively large air drag that might degrade gravity solutions if it not properly modeled. Also, two COSMIC satellites can form a tandem flight separated by few hundreds of km at an altitude 525 km, making it possible to produce GRACE-like range observables using kinematic GPS baseline solutions.

Because of the onboard GPS receiver software design, the number of visible GPS satellites at both POD antennas are not equal. On the left-hand plot of Figure 3.6, one can see the raw ionospheric measurements for all the GPS satellites in view from FORMOSAT-3/COSMIC spacecraft 5 (code name $L25$), for the four antennas (number code from 0 to 3), in terms of the elevation. The useful data for ionospheric occultations comes from antennas 0 and 1 (red and green points, code $L250$ and $L251$ respectively). On the right-hand plot of Figure 3.6, the same raw ionospheric raw measurements are depicted but now as a function of time for both antennas. Looking at the ionospheric data evolution, it is shown that antenna 1 is pointing to the antivelocity direction (setting occultations) while the antenna 0 is pointing at the velocity direction (raising occultations). The GPS and attitude data

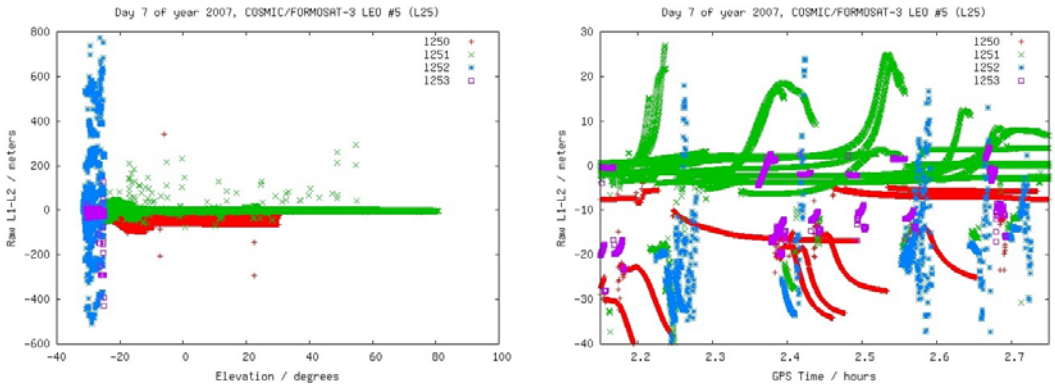

Figure 3.6: *Raw $L1 - L2$ measurements for all GPS in view from FM 5 (code name $L25$) for the 7th of January, 2007. On the left-hand, raw $L1 - L2$ measurements vs. elevation and, on the right-hand, raw $L1 - L2$ measurements vs. GPS time. The measurements are depicted with different colours regarding the receiving antenna (number codes from 0 to 3).*

are available at the TAAC web site of Central Weather Bureau of Taiwan (http://tacc.cwb.gov.tw/cdaac/index.html). Near real-time data are usually available within a few hours. [1]

[1]Request of FORMOSAT-3/COSMIC GPS data should be sent to NSPO.

3.3 Radio Occultation technique: Observables

3.3.1 Previous works: Ionospheric carrier phase as main datum

In previous studies ([Hernández-Pajares et *al.* (2000a)] and [Garcia-Fernández et *al.* (2003)]), the difference between $L1$ and $L2$ GPS carrier phases in length units, i.e. the ionospheric combination LI, has been used as the main input data to derive ionospheric profiles in occulting scenarios. The use of this observable does not require clock calibration and orbit errors since they cancel out when forming the linear combination LI. As introduced in Chapter 1, the ionospheric combination LI is related to the Slant Total Electron Content (STEC) by the following relationship:

$$LI = L1 - L2 = \alpha \cdot STEC + b \tag{3.1}$$

where $\alpha = 0.105 \frac{m}{TECU}$ and b is a bias term (the corresponding combination of $L1$ and $L2$ carrier phase ambiguities, considered constant along each GPS-LEO continuous arch of data). The bias term can be eliminated by making differences with respect to a reference observation in the arch of continuous carrier phase data. Therefore, by means of 3.1, the series of ambiguous STEC values observed at negative elevations can be used to estimate electron densities (N_e), based on the definition of STEC as the line integral of electron density Ne along the ray path:

$$STEC(p) = \int_{LEO}^{GPS} N_e \cdot dl \tag{3.2}$$

where p stands for the impact parameter i.e. the closest point to the Earth centre along the optical ray path. When following this approach and neglecting the small ray curvature, under the assumption of *spherical symmetry* (i.e. Ne only depending on the radial component), STEC can be expressed as the Abel transform of Ne (see [Bracewell (2000)]). Taking into account the geometric display shown in Figure 3.7, it is possible to relate l, r and p:

$$l = \sqrt{r^2 - p^2} \Rightarrow dl = \frac{r}{\sqrt{r^2 - p^2}} dr \tag{3.3}$$

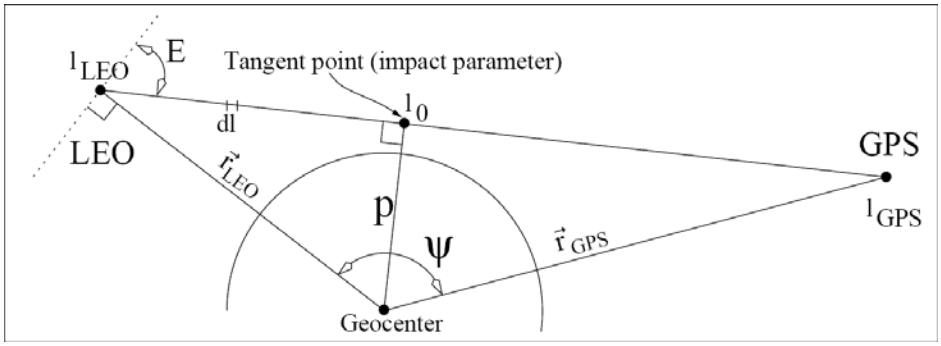

Figure 3.7: *RO geometry assuming straight ray path.*

Thus, Eq. 3.2 can be reinterpreted as:

$$\begin{aligned} STEC(p) &= \int_{l_0}^{l_{LEO}} Ne(r)dl + \int_{l_0}^{l_{GPS}} Ne(r)dl = \\ &= \left[\int_{l_0}^{l_{LEO}} + \int_{l_0}^{l_{GPS}}\right] \frac{Ne(r)r}{\sqrt{r^2-p^2}}dr \approx 2 \cdot \int_{l_0}^{l_{LEO}} \frac{Ne(r)r}{\sqrt{r^2-p^2}}dr \end{aligned} \tag{3.4}$$

where l_0 stands for the impact parameter at the beginning of the occultation, l_{LEO} the LEO position, p the impact parameter and, r the radius. The aproximation symbol is necessary since the electron content above the LEO orbit has been neglected to take advantage of the symmetry of the problem. Therefore, Ne can be now expressed as the inverse Abel transform of Eq. 3.5 (see details of Abel transform inversion in Chapter 4):

$$Ne(r) = -\frac{1}{\pi}\int_{r}^{r_{LEO}} \frac{dSTEC(p)/dp}{\sqrt{p^2-r^2}}dp \tag{3.5}$$

The above mentioned *spherical symmetry* assumption, which lays within the hypothesis of use of the classical Abel inversion needed to derive Eq. 3.5, implies that the only assumed dependence of Ne is with respect to height, not latitudinal nor longitudinal dependence.
An equivalent method to reach the solution in Eq. 3.5 is by using a recursive inversion process applied to a discretised version of Eq. 3.2:

$$STEC(p_n) \approx 2 \cdot \sum_{i=1}^{n} N_e(p_i) \cdot l_{i,n} \tag{3.6}$$

where the recursive process starts from the outer ray inwards during the RO event. Each STEC observation defines a layer in the vertical profile,

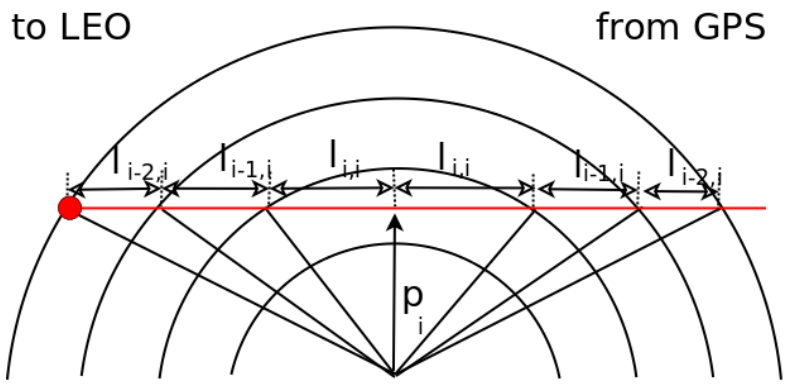

Figure 3.8: *Recursive solution of Abel transform inversion starting from the outer ray. $l_{i,j}$ is the distance travelled by the signal between two consecutive layers. All $l_{i,j}$ contribute to the total distance of the ray with impact parameter p_i. The signal starts at the GPS transmitter and ends at the LEO position (marked whit a red circle). A stright line propagation is assumed.*

therefore, the sampling rate at which the LEO gathers GPS data will determine the vertical resolution of the profile (for instance one sampling each second (1Hz), which is the case of FORMOSAT-3/COSMIC, yields to a vertical resolutions of units of km). At the *ith* step (see Fig. 3.8), the STEC corresponding to the *ith* impact parameter (p_i) would correspond to (see [Hernández-Pajares et *al.* (2000a)]):

$$STEC(p_i) = 2 \cdot l_{ii} \cdot Ne(p_i) + \sum_{j=1}^{j=i-1} 2 \cdot l_{ij} \cdot Ne(p_j) \tag{3.7}$$

By proceeding in this way, a triangular system of linear equations will be had. Starting with the uppermost observation (highest impact parameter) and processing downwards, the electron density Ne can be "inverted" as follows:

$$N_e(p_n) = \frac{STEC(p_n) - 2 \cdot \sum_{i=1}^{n-1} N_e(p_i) \cdot l_{i,n}}{2 \cdot l_{n,n}} \tag{3.8}$$

This electron content retrieval can be performed without any ionospheric background model using just the single occultation data, by means of the classical Abel transform inversion. In this strategy, the data are processed independently for each occultation in order to achieve a better resolution

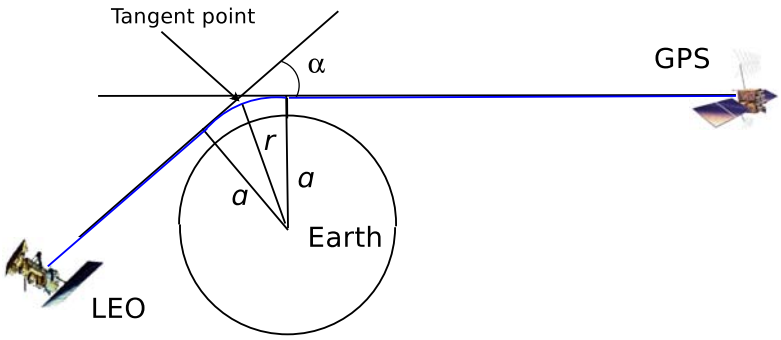

Figure 3.9: *Occultation geometry showing the bending of the signal (α) due to the dispersive nature of the atmosphere where a corresponds to the impact parameter and r to the radius at the tangent point. The geometry of the occultation is assumed to be spherically symmetric.*

with lower computational burden. Nevertheless, by working with LI, it is assumed that the integral path of $L1$ and $L2$ signals is the same, which is not stricly true when the signals are bent during an occultation through the ionosphere (they can differ up to 2km [Schreiner et *al.* (1999)]), but, as it will be shown, the different electron content between both paths is negligible.

This approach presents mainly two missmodelings, the assumption of *spherical symmetry* of the electron content distribution and the neglection of the topside electron content contribution. As shown in [Hernández-Pajares et *al.* (2000a)] and [Garcia-Fernández et *al.* (2003)], they can respectively be mitigated by means of the *Separability concept* and direct estimation.

3.3.2 Working with Doppler shift as main datum

Electron density profiles can also be retrieved applying the classical Abel transform inverse to the bending angles derived from the atmospheric induced Doppler shift in $L1$ (see [Hajj and Romans (1998)]) in occulting scenarios (see sketch representation in Figure 3.9).

The basic observable is the phase path (expressed in meters):

$$L = \int_{GPS}^{LEO} n ds \tag{3.9}$$

where L stands for either $L1$ or $L2$ carrier phase observables, and n is the phase refraction index:

$$n = \frac{c}{v_p} \tag{3.10}$$

being v_p the corresponding carrier phase velocity. The integral extends from the GPS transmitter position up to the LEO receiver one. From the phase path, the excess phase (in meters) is defined as the extra phase change induced by the atmosphere with respect to a straight line propagation:

$$\Delta L = L - \mid \vec{r}_{LEO} - \vec{r}_{GPS} \mid \tag{3.11}$$

and then, from it, define the excess Doppler (f_d) or Doppler shift:

$$f_d = \frac{d\Delta L}{dt} \tag{3.12}$$

The Doppler shift (at both the transmitter and the receiver) is produced by the change of the refraction index while the signal travels through the atmosphere (see Figure 3.10 for a simplistic picture of the measurement). It can be obtained as the carrier phase variation (shift) after subtracting the velocities of both, transmitter and receiver, projected along the actual signal propagation directions. As already pointed out, the signal Doppler shift f_d becomes the fundamental observable. The Doppler shift of the operating frequency f_T can be also derived using:

$$\begin{gathered} f_d = \frac{f_T}{c}(\vec{v_T} \cdot \hat{e_T} + \vec{v_R} \cdot \hat{e_R}) = \\ -\frac{f_T}{c}(v_T^r \cos\phi_T + v_T^\theta \sin\phi_T + v_R^r \cos\phi_R - v_r^\theta \sin\phi_R) \end{gathered} \tag{3.13}$$

where c is the speed of light, $\vec{v_T}$ and $\vec{v_R}$ are the transmitter and receiver velocities, $\hat{e_T}$ and $\hat{e_R}$ are the unit vectors tangent to the optical ray path at the transmitter and receiver positions. The symbols ϕ_T and ϕ_T denote the angles between $\vec{v_T}$ and $\hat{e_T}$ and $\vec{v_R}$ and $\hat{e_R}$, respectively, v_T^r and v_T^θ represent the radial and azimutal components of the transmitting spacecraft velocity and, respectively, v_R^r and v_R^θ for the LEO receiver (see Figure 3.11).

The signal path is curved according to Snell's law due to the changes in the index of refraction along the signal path. By assuming a medium having local spherical symmetric, Snell's law becomes Bouger's law leading to an extra constraint for the system to be solved:

$$a = n(\vec{r}) \cdot r \cdot sin\phi \tag{3.14}$$

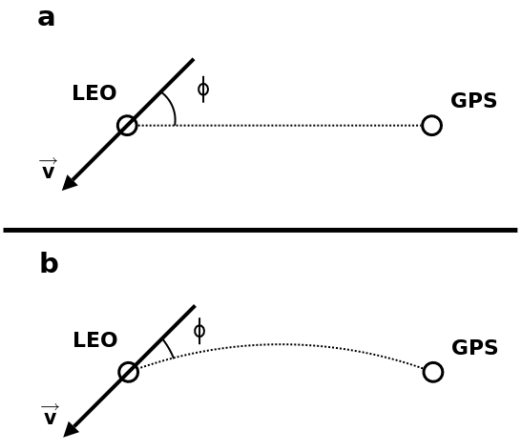

Figure 3.10: *Case **a**: In a vacuum, the Doppler shift depends on the relative velocities of transmitter and receiver of the radio wave, including incident angle ϕ, between the radio wave direction and the LEO velocity direction. Case **b**: For waves that propagate in a medium, such as the atmosphere, the ray is bend due to atmospheric refraction, the Doppler shift due to the relative movement of transmitter and receiver is different from expected. Illustrative example redrawn from [Syndergaard (1999)].*

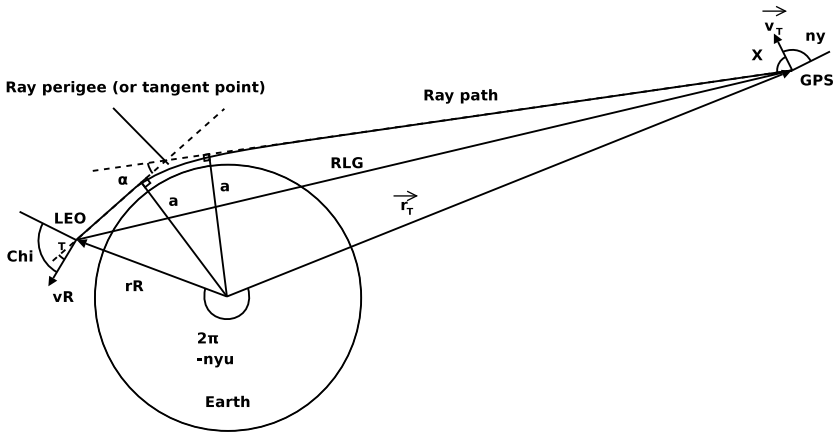

Figure 3.11: *Geometry of an occultation where parameters used in Eq. 3.13 are depicted. Adapted from [Melbourne (2004)].*

where a is a constant value, r is the module of the coordinate $\vec{r}$ of any point along the ray between transmitter and receiver, ξ the angle of the refracted ray with respect vertical. In particular, Eq. 3.14 is verified along the whole optic path of the ray. In particular:

$$a = n(\vec{r_T}) \cdot \| \vec{r_T} \times \hat{k_T} \| = n(\vec{r_R}) \cdot \| \vec{r_R} \times \hat{k_R} \| \tag{3.15}$$

being $\vec{r_T}$ and $\vec{r_R}$ represent the coordinates of the transmitter and receiver,n is the refraction index at the specified coordinates, and $\hat{k_T}$ and $\hat{k_R}$ are the unit vectors in the direction of the straight line connecting the transmitter to the receiver. To obtain the total atmospheric bending, Eq. 3.13 and 3.15 are solved simultaneously. However, the knowledge of n at $\vec{r_T}$ and $\vec{r_R}$ is required. To overcome this issue, in a first iteration, the following approximation is made, which overestimates the electron density not more than 0.5% ([Hajj and Romans (1998)]).

$$n(\vec{r_T}) = n(\vec{r_R}) = 1 \tag{3.16}$$

Actually, the higher the altitude of the LEO is, the more reasonable the approximation in Eq. 3.16 becomes. In a spherical symmetric medium, the bending of the signal can be related to the index of refraction by means of the following integral (see deduction details in Chapter 4):

$$\alpha(a) = -2a \int_0^\infty \frac{1}{\sqrt{a'^2 - a^2}} \frac{dln(n)}{da'} da' \tag{3.17}$$

whrere α stands for the bending angle, a for the impact parameter, and n, the refractive index. In this expression, the bending towards the Earth is counted positive. The bending angle α is connected to an impact parameter a which is invariant for a given ray path (see Figure 3.9). The tangent radius r in Figure 3.9 is the radial distance from the centre to the tangent point. By using an Abel integral transform, Eq. 3.17 can be inverted (see [Tricomi (1985)] and Chapter 4 for further details), obtaining the refraction index as a function of the impact parameter a:

$$ln(n(a)) = -\frac{1}{\pi} \int_a^\infty \frac{\alpha(a')}{\sqrt{a'^2 - a^2}} da' \tag{3.18}$$

The upper limit of the integral in Eq. 3.18 requires knowledge of the bending α as function of a up to the top of the atmosphere. For practical matters, the bending angles above the LEO can either be neglected, extrapolated somehow or replaced by a climatological model ([Schreiner et *al.* (1999)]). In the current study, this integral is solved,

firstly up to the LEO height, neglecting the bendings angles above the LEO orbit, secondly, using a climatological model and, thirdly, an extrapolation scheme is also explored (see Chapter 6).

3.4 Clock drift

A key factor for an accurate phase delay modeling is the epoch of the measurement. The measured phase at the receiver depends on the true phase accumulation between the emitter and the receiver, which is obtained from the difference between the clock epochs of the emitter and receiver. Knowing the offset in time between the two clocks at a given instant is essential. More precisely, knowing the variability of this offset with time is essential. A constant offset is of no theoretical consequence (but it can be an operational problem) because the refraction information in the phase measurements is contained in their change with time. Therefore, in order to compute accurate radio occultation inversions, the clock drifts of the GPS transmitter and receiver clocks should be removed from the raw phase data, otherwise, the clock drifts could contribute to the major part of the excess Doppler when solving bending angles derived from the Doppler $L1$ phase excess. A completely unrealistic result (several orders of magnitude higher) would be obtained as depicted in Figure 3.12, where there is an example of a non-calibrated excess Doppler calculated from Eq. 3.12. Indeed, the most relevant terms when modeling the carrier phase observable L_i^j between a LEO receiver (i) and the GPS transmitter (j) for an ionospheric occultation are (the tropospheric delay is negligible at such heights):

$$L_i^j = c(T_{rec} - T^{trans}) = c(t_{rec} - t^{trans}) + c(T_i - T^j) + rel_i^j - Ion_i^j + B_i^j \quad (3.19)$$

where T_{rec} and T^{trans} are the instrumental times at receiver and transmitter, t_{rec} and t^{trans} are the actual times, T_i and T^j stand for the clock offsets of the LEO and the GPS satellite, rel_i^j is the relativistic effect, Ion_i^j is the ionospheric delay and B_i^j is the phase ambiguity. Actually, $c(t_{rec} - t^{trans})$ gives the geometric distance between GPS and LEO $\mid \vec{r}^j - \vec{r}_i \mid$. When taking the time derivatives of this expression, the first two terms are the most significat, i.e.

$$\frac{dL_i^j}{dt} = \frac{d \mid \vec{r}^j - \vec{r}_i \mid}{dt} + c\frac{d(T_i - T^j)}{dt} \quad (3.20)$$

If the clock errors are not properly treated, the main contribution could come from the last term in Eq. 3.20. It also follows from Eq. 3.20 that it is

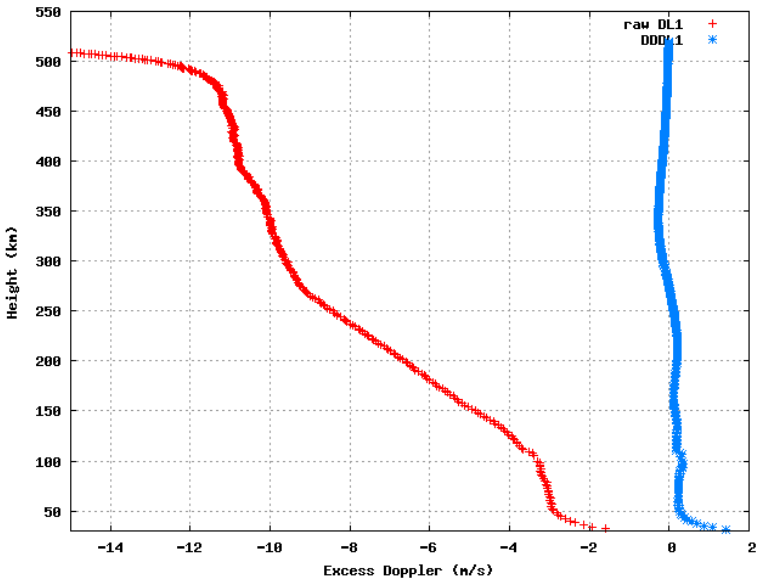

Figure 3.12: *FORMOSAT-3/COSMIC occultation on January 6th, 2007, PRN 17 (where PRN stands for GPS satellite identification number), LEO l241, 04h 25min UT: raw excess Doppler (without removing clock drifts) derived from FORMOSAT-3/COSMIC observables versus doubled differenced excess Doppler (DDDL1). The unrealistic values of the raw excess Doppler, which are a result of the clock drifts, can readily be seen. For graphical purposes, the excess Doppler values are denoted by DL1.*

necessary to remove the geometrical effects due to the motion of the satellites and properly calibrate the transmitter and receiver clocks.

In the case of GPS satellites, they are equipped with atomic clocks (rubidium, cesium) which have a very high stability (see Table 3.1). Each GPS satellite carries onboard up to four very precise cesium and/or rubidium frequency standards for controlling time and time intervals. In addition to the GPS clock errors, the clock error in the LEO receiver also must be taken into account and eliminated. However, the LEO usually carries an inferior frequency standard, which requires some strategy for eliminating this error source. Using these tracking data and applying a "single-differencing" or equivalent scheme among the tracked phase measurements referenced to common transmit epochs, one can eliminate clock offset errors among the GPS satellites. This configuration is depicted in Figure 3.13, which shows the LEO satellite (with GPS receiver onboard) observing the setting GPS

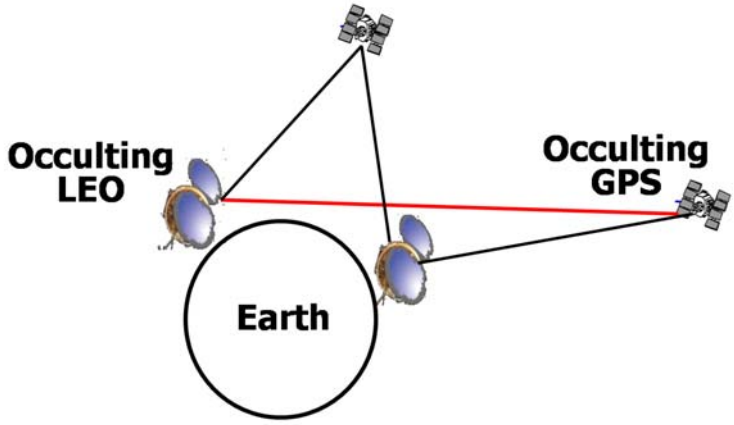

Figure 3.13: *Double difference configuration: a pair of LEO-GPS satellites in occulting geometry (red link) with another pair of non-occulting LEO and GPS satellites.*

Table 3.1: *Clock stabilities. Source [Leick (1994)]*

Clock types	Daily stability	Elapsed time to deviate a second
Quarz crystal	10^{-9}	30 years
Rubidium	10^{-12}	30000 years
Cesium	10^{-13}	300000 years
Hydrogen	10^{-15}	30000000 years

satellite and simultaneously a second GPS satellite clear of any intervening medium, a so-called reference satellite. Differencing the phase measurements from concurrent tracking of these two (now synchronized) GPS satellites at the same reception epoch eliminates the LEO clock error. The cost of this strategy in measurement precision is essentially an increase by a factor two in data noise, usually not a significant limitation except in threshold detection situations. Another way to proceed would be by applying a "double-differencing" scheme. This can be done either by:

1. Working with double-differences (noted as DD) of the phase measurements from the onboard GPS receiver regarding to a fiducial ground station in common viewing of the occulting LEO and GPS, and another non-occulting GPS [Wickert et *al.* (2001)]. Nevertheless, there is the drawback of the potential presence of high frequency multipath when using ground based GPS data to remove clock drifts (see [Ogaja and Satirapod (2007)]) and, in order to have global coverage for all occultation measurements, a global ground network would be required.

2. Thanks to the FORMOSAT-3/COSMIC constellation configuration, a six evenly distributed LEO network of satellites, it is possible to use a second non-occulting LEO satellite to perform the double differences (see Figure 3.13) as suggested on [Rocken et *al.* (2000)] since complete double difference coverage is provided by such constellation (see Figure 3.15 -red-). Before the advent of the FORMOSAT-3/COSMIC constellation, the double differencing would have involved a ground station.

In this thesis, a novel approach to double-differencing has been explored for which no extra GPS or LEO satellites (apart from the ones involved in the RO event) are require to remove the drifts due to the receiver's and transmitter's clock. The selected strategy has been to use the fact that the Doppler shift, which causes the ray bending due to rafractivity gradients (hence the bending angle), can be deduced to be proportional to the electron density gradient (see deduction below) under some assumptions (simply considering the nominal value of L_1 GPS frequency, f_1 (1575.42 MHz), being considerably bigger than the plasma frequency fc (20 MHz)). Using the relationship between the bending angle α and the refraction index n that will be introduced in Chapter 4:

$$\Delta\alpha \propto \Delta f_i \propto \frac{\Delta Ne}{f_i^2} \tag{3.21}$$

using Δf_i to denote the excess Doppler of L_i with its corresponding frequency f_i. From this relationship, it can be derived that:

$$\Delta f_1 \cdot f_1^2 = \Delta f_2 \cdot f_2^2 = K \cdot \Delta Ne \tag{3.22}$$

being K the proportionality constant equal to $\frac{e^2 tan\phi}{2\varepsilon_0 m_e}$ (for a given LEO-GPS geometry, ϕ is common for frequencies), e the electron charge, m_e the rest mass of an electron, ε_0 the permitivity of free space. For both transmitting frequencies, the excess Doppler (Δf_i) is defined as the time derivative of the excess phase (ΔL_i) with the corresponding removal of the clock drift ($\frac{dT}{dt}$):

$$\Delta f_i \propto \frac{d\Delta L_i}{dt} - \frac{dT}{dt} \tag{3.23}$$

Let A be the proportionality factor for dimensionality matters in Eq. 3.24. It can then be rewritten as:

$$\Delta f_i A = \frac{d}{dt}[\Delta L_i - T] \tag{3.24}$$

Manipulating Eq. 3.22, it is possible to derive:

$$\begin{gathered} 0 = \Delta f_1 \cdot f_1^2 - \Delta f_2 \cdot f_2^2 = \frac{A}{f_1^2 - f_2^2}(\Delta f_1 \cdot f_1^2 - \Delta f_2 \cdot f_2^2) = \\ \frac{\Delta f_1 \cdot f_1^2 A - \Delta f_2 \cdot f_2^2 A}{f_1^2 - f_2^2} = \frac{\frac{d}{dt}[\Delta L_1 - T] f_1^2 - \frac{d}{dt}[\Delta L_2 - T] f_2^2}{f_1^2 - f_2^2} = \\ \frac{\frac{d}{dt}[\Delta L_1 f_1^2] - \frac{d}{dt}[\Delta L_2 f_2^2] - (f_1^2 - f_2^2)\frac{dT}{dt}}{f_1^2 - f_2^2} = \\ \frac{\frac{d}{dt}[\Delta (L_1 f_1^2 - L_2 f_2^2)] - (f_1^2 - f_2^2)\frac{dT}{dt}}{f_1^2 - f_2^2} = \\ \frac{d}{dt}[\Delta Lc - T] \end{gathered} \tag{3.25}$$

Hence:

$$\frac{dT}{dt} = \frac{d}{dt}[\Delta Lc] \tag{3.26}$$

Therefore, it has just been shown that it is equivalent to remove the clock drift to subtract the Lc drift to the carrier phase data.
In Figure 3.14, the excess phase for L_1 and L_2 are compared (red pluses and green crosses, respectively). It can be seen that both excess phase are inversaly proportional to their respective frequencies as stated in Eq. 3.21 (notice that the excess phase of L_2 has been multiplied by the factor $\frac{f_2^2}{f_1^2}$ that allows its direct comparison with the excess phase of L_1). This implies that the ray paths of both signals are essentially the same. Therefore, when combined with the same combination of coefficients used to derive the ionospheric free combination, $Lc = \frac{f_1^2 L_1 - f_2^2 L_2}{f_1^2 - f_2^2}$, an observable with no bending is obtained and,

when no double difference is performed, this particular observable would take into account only the clock drift at ionospheric heights (see Figure 3.14 for further examples at different locations and local times confirming the results) as finally deduced in Eq. 3.26. In Figure 3.15, an example of such equivalence at ionospheric heights is provided: the excess phase has been calculated using both, the double differencing approach using a second pair of non-occulting GPS to LEO rays and, using the new observable with no bending to remove the clock drift. Note that not only the observable are equivalent but their noise are compatible. The noticeable discrepancies at bottom heights reflect the tropospheric delay signature, which affects only the double difference method and at non intersecting heights between ionosphere and troposphere. Hence, the clock calibration method of this work will be valid for ionospheric radio occultation processing but, for tropospheric retrievals, double differencing will be required. Under this approach, no extra GPS transmitters or LEO receivers but the ones involved in the radio occultation event are required to calibrate the clocks. Consequently, more occultations can be inverted with less data processing and computational load.

3.5 Raytracing technique

In this secction, a detailed description of the ray-tracing technique used to compute the refractive index is discussed. From the Doppler data, the function $\alpha(a)$ relating the impact parameter and the bending angle is derived in the manner described in the previous section. The atmosphere is considered to be consisting of several spherical layers. For each layer, to avoid mathematical complexity, constant refractivity has been considered within the layer. One ray passes tangentially through the middle of each layer. The radius of each layer is deduced from the previous and following impact parameters of the function $\alpha(a)$:

$$r_i = \frac{1}{2}(a_{i-1} + a_i) \tag{3.27}$$

being the initial radius r_1 the one given by the LEO position at the starting epoch of the RO. To keep track of the rays, the angle of incidence and the angle of refraction need to be determined for the boundary of each layer.

Due to symmetry, no additional calculations are necessary in order to analyse the tracking of the ray out on the other side of the atmosphere.

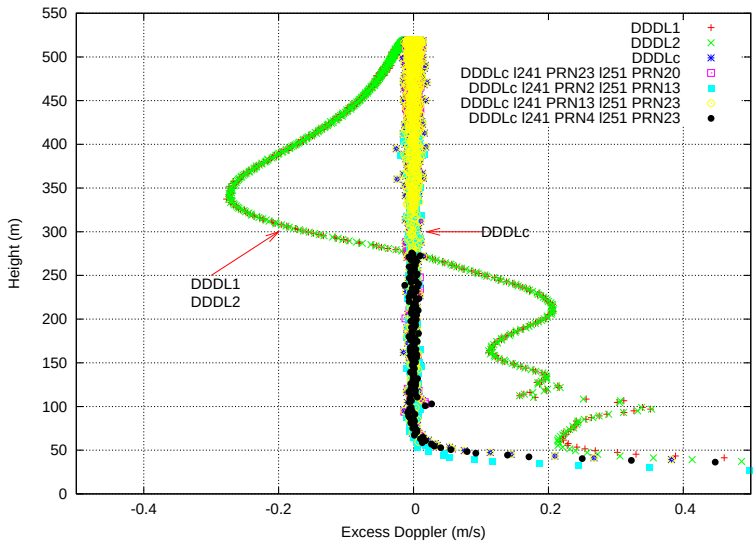

Figure 3.14: *The first three lines in this figure show an example of the equivalence of L1 and L2 phase rate excess for a given occultation: L1 phase rate excess with red pluses, L2 phase rate excess with green crosses multiplied by the corresponding factor in order to be directly compared with the red-crossed curve, and Lc phase rate excess with blue asterisks (basically vertically distributed). The following four lines give additional examples of Lc phase rate excess for several occultations with different LEO and GPS satellites involved and different locations and time occurrences.*

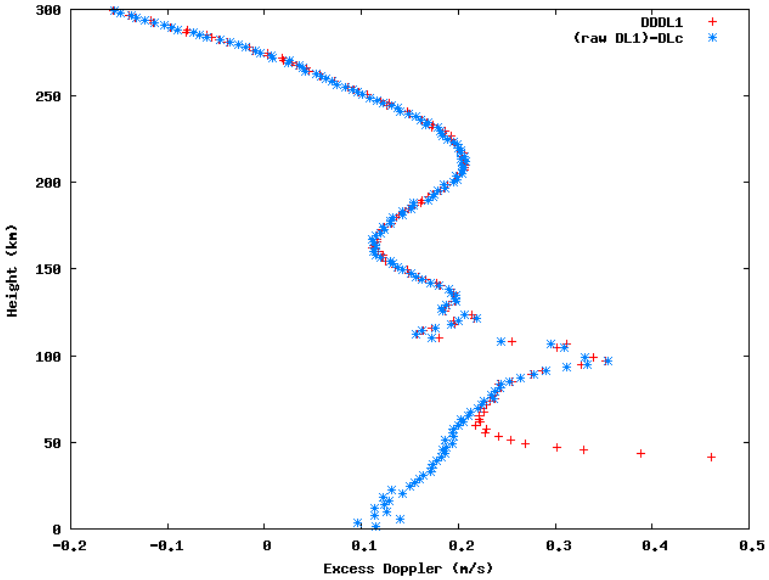

Figure 3.15: *FORMOSAT-3/COSMIC occultation for January 8th, 2007, PRN 13, LEO l241, 04h 32min UT: Equivalence of clock calibration strategies: The red cross symbols, L1 excess Doppler (represented by DL1) without clock drifts by double differencing (noted with DD) using a second pair of non-occulting LEO and GPS satellites. The blue asterisk symbols, L1 excess Doppler without clock drifts by subtracting Lc observable to L1 (represented by (raw DL1)-DLc). An agreement of both approaches is shown at ionospheric heights, as expected, while the double differencing (red) curve shows the remaining tropospheric bending at heights below 60km, which does not cancel out in this case.*

Chapter 4

Mathematical principles of the Abel inverse transform and its application to GNSS RO

Se puede tener, en lo más profundo del alma, un corazón cálido y, sin embargo, puede que nadie acuda jamás a acogerse en él
Cartas a Theo- Vincent van Gogh

4.1 Introduction

As explained in previous chapters, a function relating impact parameters and bending angles $\alpha(a)$ can be derived from the excess phase excess and POD information from both GPS and LEO satellites. The main goal of this chapter is to explain how the classical Abel inverse transform is used in the context of GNSS RO. Furthermore, the adaptation of an improvement of the classical Abel inversion to bending angles is going to be presented, which overcomes the spherical symmetry hypothesis required in the classical approach.

4.2 Abel inverse transform

4.2.1 General approach

Among the many mathematical tools useful for analyzing linear systems, one can find linear transforms. In physical systems, it is usual to encounter pairs of functions which are related by an integral relationship such as the ones presented in previous chapters for $STEC$ and electron density N_e:

$$STEC(p) = 2\int_{l_0}^{\infty} \frac{Ne(r)r}{\sqrt{r^2 - p^2}} dr \tag{4.1}$$

and, for bending angle α and refraction index n:

$$\alpha(a) = 2a \int_{a'=a}^{\infty} \frac{dn}{da'} \frac{da'}{n\sqrt{(a')^2 - a^2}} \tag{4.2}$$

where the integration variable is $a' = nr$. In a more general way, the integral relationship between the functions in 4.1 and 4.2 can be presented in the following form:

$$f(a) = \int_a^b g(t)K(w,t)dt \tag{4.3}$$

The function $f(a)$ is called the integral transform of the function $g(t)$ by the kernel $K(w,t)$. In general, it cannot be expected that the inverse of an integral of the kind of 4.3 exists. Nevertheless, there is a special subset among the equations having this form, and whose inverse transform exists:

$$g(t) = \int_\alpha^\beta f(a)k(w,t)da \tag{4.4}$$

The relationship of the kernel function $k(w,t)$ of the inverse transform of the kernel $K(w,t)$ is straight-forward, but it is dependant on the nature of the transform. In particular, the Abel transform can be strictly defined as:

$$f(a) = \int_0^\infty g(r)K(r,a)dr \tag{4.5}$$

where:

$$K(r,a) = \begin{cases} \frac{2r}{\sqrt{r^2-a^2}} & \text{if} \quad r > a \\ 0 \quad \text{otherwise} \end{cases} \tag{4.6}$$

or, alternatively, as:

$$f(a) = \int_a^\infty g(r) \frac{2r}{\sqrt{r^2 - a^2}} dr \tag{4.7}$$

The inverse Abel transform exists for this particular case of kernel and integral relationship, provided the function f is differentiable, adopting the followings form:

$$g(r) = -\frac{1}{\pi} \int_r^\infty \frac{f'(a)}{\sqrt{a^2 - r^2}} da \tag{4.8}$$

or, after performing an integration by parts:

$$g(r) = -\frac{1}{\pi} \int_r^\infty (a^2 - r^2)^{\frac{1}{2}} \frac{d}{da} \left[\frac{f'(a)}{a} \right] da \tag{4.9}$$

If the integral would become zero beyond some value of r (let's assume r_0 being such value), Eq.4.9 could be rewritten as follows:

$$g(r) = -\frac{1}{\pi} \int_r^{r_0} (a^2 - r^2)^{\frac{1}{2}} \frac{d}{da} \left[\frac{f'(a)}{a} \right] da - \frac{f'(r_0)}{\pi r_0} (r_0^2 - r^2)^{\frac{1}{2}} \tag{4.10}$$

4.2.2 Application of the Abel transform to RO

In [Fjeldbo et *al.* (1971)], it was shown that the derivation of the refractive index $n(r)$ from bending angles $\alpha(a)$ is a particular case of Abel inversion. For a radio signal travelling through the atmosphere, the bending angle can be expressed as:

$$\alpha(a) = 2a \int_{a'=a}^{\infty} \frac{dr}{da'} \frac{da'}{(r(a')^2 - a^2)^{\frac{1}{2}}} \tag{4.11}$$

where the integration variable is $a' = nr$. This relationship can be derived as follows:
When considering the geometry of a refracting ray, spherical coordinates can be used to represent all the involved parameters. The centre of the Earth is considered to be the centre of the coordinate system. Let us suppose that the distance r to a ray increases by the distance dr as the position vector to the ray sweeps through the angle $d\varphi$. The angle of incidence i can be expressed using the polar ray path coordiantes (r, φ) as:

$$tan(i) = r\frac{d\varphi}{dr} \tag{4.12}$$

In this coordinates, the general form of Bouger's law [Born and Wolf (1980)] becomes:

$$a = nr \cdot \sin(i) \tag{4.13}$$

Looking at the geometric representation of the occultation geometry in Figure 4.1, it can be stated that the relationship among the three angles φ, i and ψ is that their sum is equal to a right angle:

$$\varphi + i + \psi = \frac{\pi}{2} \tag{4.14}$$

Differenting this expression, the differentials of these parameters are related by:

$$d\varphi + di + d\psi = 0 \tag{4.15}$$

From here, $d\psi$ can be isolated:

$$d\psi = -d\varphi - di \tag{4.16}$$

At this point, we would like to develop expressions for $d\varphi$ and di to use in 4.13, thus deriving an expression for $d\psi$ that can be integrated to account for the total bending angle α. Begining by taking the derivative of 4.13 with respect to r:

$$0 = \frac{dn}{dr} r \cdot sin(i) + n \cdot sin(i) + nr \cdot cos(i)\frac{di}{dr} \tag{4.17}$$

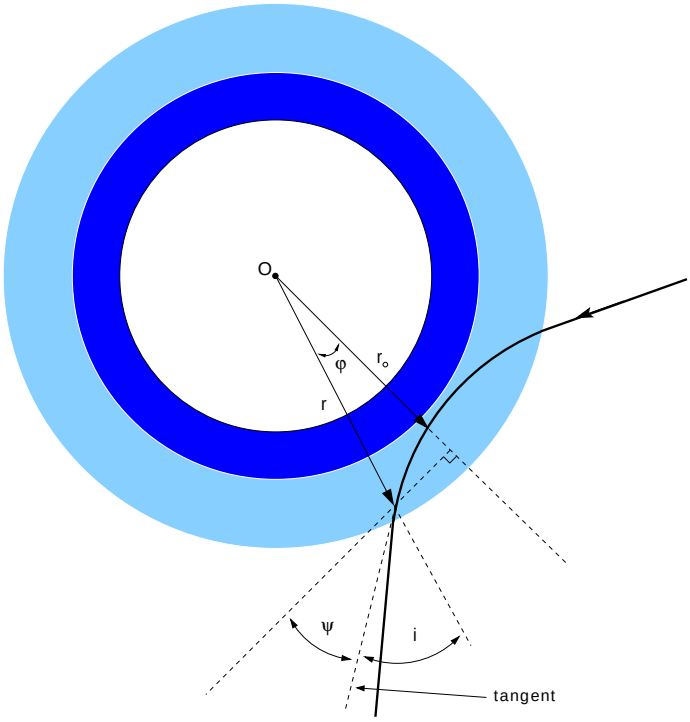

Figure 4.1: *Geometric representation of the ray path geometry during an occultation event.*

and solving for di, it is obtained:

$$di = \frac{-(\frac{dn}{dr} \cdot sin(i) + n \cdot sin(i))}{nr \cdot cos(i)} dr \tag{4.18}$$

Using Bouger's law:

$$sin(i) = \frac{a}{nr} \tag{4.19}$$

and taking into account the fundamental trigonometric relationship between sine and cosine of a given angle, it is possible to derive:

$$cos(i) = \sqrt{1 - sin^2(i)} = \frac{\sqrt{nr^2 - a^2}}{nr} \tag{4.20}$$

The expression in 4.18 for di simplifies to:

$$di = -\frac{a(n + \frac{dn}{dr} r)dr}{nr\sqrt{(nr)^2 - a^2}} \tag{4.21}$$

Turning to the expression in 4.12 for $tan(i)$ and solving for $d\varphi$:

$$r\frac{d\varphi}{dr} = tan(i) = \frac{sin(i)}{cos(i)} = \frac{\frac{a}{nr}}{\frac{\sqrt{((nr)^2 - a^2)}}{nr}} \tag{4.22}$$

Simplifying:

$$d\varphi = \frac{dr}{r} \frac{a}{\sqrt{(nr)^2 - a^2}} \tag{4.23}$$

Combining the expressions for $d\varphi$ and di, we can obtain an expression for $d\psi$:

$$d\psi = \frac{a(n + \frac{dn}{dr} r)dr}{nr\sqrt{(nr)^2 - a^2}} - \frac{dr}{r} \frac{a}{\sqrt{(nr)^2 - a^2}} \tag{4.24}$$

A final simplification provides an expression for $d\psi$ in therms of a, n and r:

$$d\psi = \frac{a}{\sqrt{(nr)^2 - a^2}} (\frac{dn}{dr}) \frac{r}{n} \tag{4.25}$$

The integration of $d\psi$ along the entire ray path yields the angular deflection of the beam i.e. the total bending angle α in the following way:

$$\alpha(a) = 2 \int_{r=r_0}^{\infty} d\psi = 2a \int_{r=r_0}^{\infty} \frac{dn}{ndr} \frac{dr}{\sqrt{(nr)^2 - a^2}} \tag{4.26}$$

Eq. 4.26 may be inverted by using a substitution of variables in the integration of $a' = nr$, leading to a form of the integral which is consistent with a standard Abel transform formulation:

$$\alpha(a) = 2a \int_{a'=a}^{\infty} \frac{dn}{nda'} \frac{da'}{\sqrt{(a')^2 - a^2}} \tag{4.27}$$

as presented at the beginning of this chapter. Inverting Eq. 4.27, we obtain:

$$ln(n(a)) = \frac{1}{\pi} \int_{a}^{\infty} \frac{\alpha(a')}{\sqrt{(a')^2 - a^2}} da' \tag{4.28}$$

Under the assumption of spherical symmetric and continuous atmosphere, the impact parameter a is related to r by:

$$r = \frac{a}{n(a)} \tag{4.29}$$

From Eq. 4.28 and Eq. 4.29, the refractive index $n(r)$ is obtained as a function of the radius r. From here, refractivity N can be calculated via the formula:

$$N(r) = (n(r) - 1) \cdot 10^6 \tag{4.30}$$

Refractivity can be used to derive electron density content, temperature and pressure profiles for the atmosphere of the Earth. These profiles are the usual products provided by atmospheric RO experiments. In our case, we are deeply interested in deriving and analyzing electron density profiles at ionospheric heights.

Note: We could find in literature an integral equation only differing in a sing with regards Eq. 4.26, a fact that is due to the difference in the sense of curvature of the ray. Strictly speaking, Eq. 4.26 applies to the ionosphere, where the bending is away from the Earth, while the opposite one to neutral atmosphere, where the ray bending is towards the Earth.

4.2.3 Integral discretization

In the current thesis, Eq. 4.26 is discretized and a recursive solution for the refractive index n is obtained. This discretization procedure is valid for classical Abel and, at some point, with some extra approximations, will lead to the implementation of separability to bending angles. Starting from the outer ray inwards (see Figure4.2):

$$\alpha_i = \sum_{j=1}^{i-1} \alpha_j^{LEO} + \sum_{j=1}^{i-1} \alpha_j^{GPS} - tan\varphi_i \cdot \frac{n_i - n_{i-1}}{n_{i-1}} \tag{4.31}$$

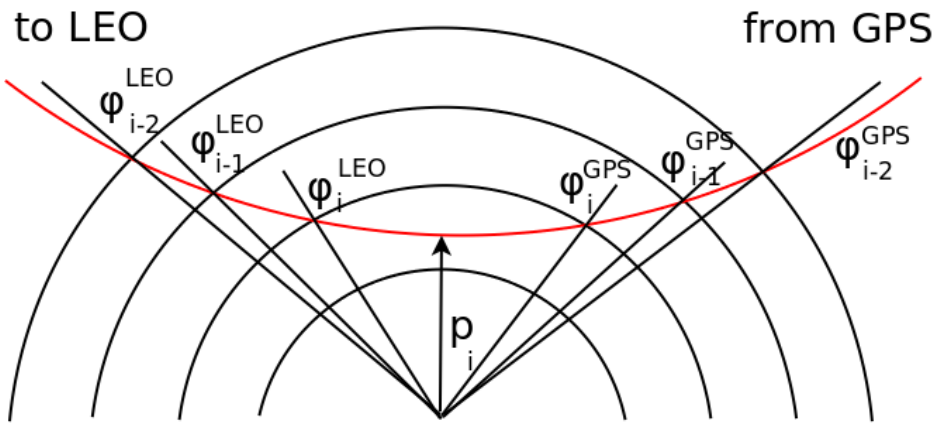

Figure 4.2: *Recursive solution starting from the outer ray. φ_i is the angle between the radial and the ray propagation directions for each layer. Both φ_i^{GPS} and φ_i^{LEO} contribute to the total bending angle α_i of the ray with impact parameter p_i. The bending of the signal in this figure would correspond to bending at ionospheric heights and has been exaggerated.*

$$\alpha_j^{satellite} = -tan\varphi_j^{satellite} \cdot \frac{n_j - n_{j-1}}{n_{j-1}} \tag{4.32}$$

where α_j^{LEO} and α_j^{GPS} represent the bending angle of the LEO satellite, respectively the GPS satellite, at the *jth* layer and φ_i is the angle at the *ith* layer intersection with the radial vector from the centre of the Earth to the GPS satellite, respectively the LEO satellite. The resulting system can be "inverted" (solved recursively) obtaining the refractive index n_i for each layer in which the atmosphere has been divided into:

$$n_1 = 1 - \frac{\alpha_1}{tan\varphi_1} \tag{4.33}$$

$$n_i = n_{i-1}(1 + \frac{\sum_{j=1}^{i-1} \alpha_j^1 + \sum_{j=1}^{i-1} \alpha_j^2 - \alpha_i}{tan\varphi_i}) \tag{4.34}$$

The solution given by Eq. 4.33 and 4.34 corresponds to classical Abel inversion in a discreet way. At this point, and in order to solve electron densities from the obtained refractive indexes, the following relationship is used, valid for GPS frequencies (see [Parkinson and Spilker (1996)]):

$$n = 1 - \frac{40.3 \cdot Ne}{f^2} \tag{4.35}$$

where f stands for the carrier frequency of the transmitted signal in Hertz ($L1$ in this case), and Ne is given in $\frac{e}{m^3}$. Eq. 4.35 only considers main terms in the dependency of the Earth's ionosphere on electron density Ne (ions and the Earth's magnetic field are neglected).
One new contribution of this work is the implementation of the *Separability concept* to Eq. 4.35, that is to say, to substitute Ne by the expression given in Eq. 4.37 and solving for the new unknown, the shape function. Nevertheless, the approximation in Eq. 4.35 is not enough to linealize the problem when solving the refraction index under the *Separability hypothesis*. An extra approximation is needed regarding the working system frequency versus the plasma frequency, which rarely exceeds 20 MHz. The latter is neglected to obtain the final linearized expression relating n and Ne at two consecutive layers:

$$\frac{n_j - n_{j-1}}{n_{j-1}} \propto Ne_j - Ne_{j-1} = \Delta Ne_j \tag{4.36}$$

From this expression, and substituting Eq. 4.37, electron density profiles can be derived with separability implemented to bending angle.

4.3 Improved Abel inversion

As mention in Sect. 4.2, the classical Abel transform assumes spherical symmetry in the neighbouring area of an occultation when retrieving electron density profiles. In order to correct the error due to this assumption, the separability concept was developed in [Hernández-Pajares et *al.* (2000a)] for the LI combination helping mitigating this drawback considering that the electron density can be expressed by a combination of $VTEC$ data assuming the horizontal dependency and a shape function assuming the height dependency:

$$N_e(\lambda, \varphi, h) = VTEC(\lambda, \varphi) \cdot F(h) \tag{4.37}$$

being λ longitude and φ latitude, respectively. The $VTEC$ information is externally provided either by a model or real data computed from ground receiver measurements (see, for instance, [Hernández-Pajares et *al.* (1999)]). Therefore, the shape function becomes the new unknown to solve. Notice that the hypothesis of sharing the same shape function in the neighbouring area of the occultation is less restrictive than sharing the same electron density (as the spherical symmetry assumption would imply). In this thesis, unless stated specifically, the $VTEC$ information has been spatially/temporally extrapolated following [Schaer et *al.* (1998)] procedure at each (λ, φ) location from the Ionospheric product IONEX computed for IGS at the Techni-

cal University of Catalonia (UPC). The implementation of separability when working with bending angles as main input is not straightforward, since the relationship between refractive index and electron density is not of proportionality. For two consecutive layers, when considering the atmosphere to be built up with concentric layers each with its corresponding refractive index, and taken into account the relationship between n and Ne, the following expression would be obtained:

$$\frac{n_i - n_{i-1}}{n_{i-1}} = \frac{40.3(Ne^{i-1} - Ne^i)}{f^2 - 40.3 \cdot Ne^{i-1}} \tag{4.38}$$

and no "separability" between n and Ne is found. The required relationship between n and Ne to allow so would be one of the kind:

$$\frac{n_i - n_{i-1}}{n_{i-1}} \propto Ne^{i-1} - Ne^i = \Delta Ne^i \tag{4.39}$$

in order to allow the "separability" of the fuctions involved. Fortunately, it has been possible to obtain a linear relationship by means of some approximations. The details of this adaptation of the improved Abel inversion to bending angles are provided in next section.

4.3.1 Adaptation of IAI to bending angles

In order to implement separability to bending angles, it would be required to have a proportional relationship between bending angles and electron densities that would allow, for two consecutive concentric spherical layers, to write the increment of bending angles as the corresponding increment of electron densities withing the two layers. Unfortunately, this is not the case (see 4.38) and some approximations are needed to derive such proportionality.
We start from the definition of the ionosphere's refractive index n derived by Appleton and Hartree, and accept that it can be approximated by first-order form with an accuracy better than 0.1% [Davies (1990)] (which is enough to analyze most of the effects on GPS signals):

$$n^2 = 1 - \frac{f_p^2}{f^2} \tag{4.40}$$

where f is the system operating frequency and f_p, the plasma frequency that is defined by:

$$f_p = \sqrt{\frac{N_e \cdot e^2}{\varepsilon_0 m (2\pi)^2}} \tag{4.41}$$

where e stands for the electron charge, ε_0 the permittivity of free space and, m the rest mass of a electron. Hence, the expression in Eq. 4.40 now becomes:

$$n^2 = 1 - \frac{N_e \cdot e^2}{\varepsilon_0 m (2\pi f)^2} \tag{4.42}$$

Differenciating the latter equation gives:

$$2ndn = -\frac{e^2}{\varepsilon_0 m (2\pi f)^2} dN_e \tag{4.43}$$

$$\frac{dn}{n} = -\frac{1}{2} \frac{e^2}{\varepsilon_0 m (2\pi)^2 (f^2 - f_p^2)} dN_e \tag{4.44}$$

Considering the nominal value of GPS frequency L_1 ($f1$=1575.42 MHz) and the plasma frequency (f_p=20 MHz), the denominator in Eq. 4.44 can be approximated by:

$$f^2 - f_p^2 \simeq f^2 \tag{4.45}$$

Substituting Eq. 4.45 in Eq. 4.44 leads to:

$$\frac{dn}{n} \simeq -\frac{1}{2} \frac{e^2}{\varepsilon_0 m (2\pi)^2 f^2} dN_e \tag{4.46}$$

The latter equation provides the key to separability implementation when using the L_1 bending angle α_1 as input data for the inversion since it will give the proportionality relatioship between bending angle and electron density. Using Bouguer's formula, which is the extension of Snell's law in a spherically symmetric medium, we can stablish the relationship of bending angle α and the refractive index n:

$$nrsin\theta = a \tag{4.47}$$

where r stands for the geocentric distance, θ the zenith angle of the LOS vector and a the impact parameter. Considering a layered ionsphere, the change between different layers is obtained by differentiating Eq. 4.47:

$$\triangle nrsin\theta + n \triangle rsin\theta + nrcos\theta \triangle \theta = 0 \tag{4.48}$$

Rearranging the terms in previous equation gives:

$$\triangle\theta = -\frac{\triangle n}{n} tan\theta - \frac{\triangle r}{r} tan\theta \tag{4.49}$$

The first term in Eq. 4.48 takes into account the change in the ray path due to the changes in the refractive index while the second depends on the

geometric variations. Actually, the first term provides the definition of the bending angle change in terms of n:

$$\triangle\alpha = -\frac{\triangle n}{n} tan\theta \tag{4.50}$$

Recalling the expression in Eq. 4.46, it can be derived that the increment of bending angle between to consecutive layers with different refractive index can be expressed as:

$$\triangle\alpha = -\frac{\triangle n}{n} tan\varphi = \frac{1}{2}\frac{e^2}{\varepsilon_0 m(2\pi f)^2} \triangle N_e tan\varphi \tag{4.51}$$

Therefore, the total bending angle for one ray path would be obtained by adding up all bending angle contributions:

$$\alpha = \sum \triangle\alpha_i = \frac{1}{2}\frac{e^2}{\varepsilon_0 m(2\pi f)^2} \sum \triangle N_{ei} tan\varphi_i \tag{4.52}$$

and, now, recalling the expression of separability in Eq. 4.37, we can finally write:

$$\alpha = \frac{1}{2}\frac{e^2}{\varepsilon_0 m(2\pi f)^2} \sum VTEC(\lambda_i, \varphi_i) \triangle F(h_i) tan\varphi_i \tag{4.53}$$

which will enable us to implement separability to bending angles.
The implementation of separability to bending angles provides an inverting method that could allow its extension to neutral atmosphere, extension that is not feasible when working with occultation data derived from the LI observable (because the tropospheric signature cancels out when forming $LI = L1 - L2$).

Chapter 5

Improved Abel transform inversion: Results

Retoñarán aladas de savia sin otoño
reliquias de mi cuerpo que pierdo en cada herida.
Porque soy como el árbol talado, que retoño:
porque aún tengo la vida.
El hombre acecha- Miguel Hernández

5.1 Introduction

The FORMOSAT-3/COSMIC satellite constellation has become an important tool towards providing global remote sensing methods for sounding of the Earth's atmosphere and ionosphere. In this chapter, some drawbacks of the Abel transform inversion in LEO GPS sounding are overcome by considering the separability concept: horizontal gradients of Vertical Total Electron Content ($VTEC$) information is ingested by the inversion method, providing more accurate density determinations. The novelty presented in this chapter with respect to previous works is the use of the excess phase rate as main observable instead of the ionospheric combination observable for the implementation of separability in the inversion process. Some of the characteriscs of the method when applied to the phase excess are discussed. The obtained results show the equivalence of both approaches but the method exposed in this work has the potentiality to be used to neutral atmosphere. Recently available FORMOSAT-3/COSMIC data have been processed both with the classical Abel inversion and the separability approach, and evaluated versus collocated ionosonde data.

5.2 Proof-of-concept: First results using FORMOSAT-3/COSMIC data

The FORMOSAT-3/COSMIC constellation provides global observations of refractivity, pressure, temperature, humidity, TEC, ionospheric electron den-

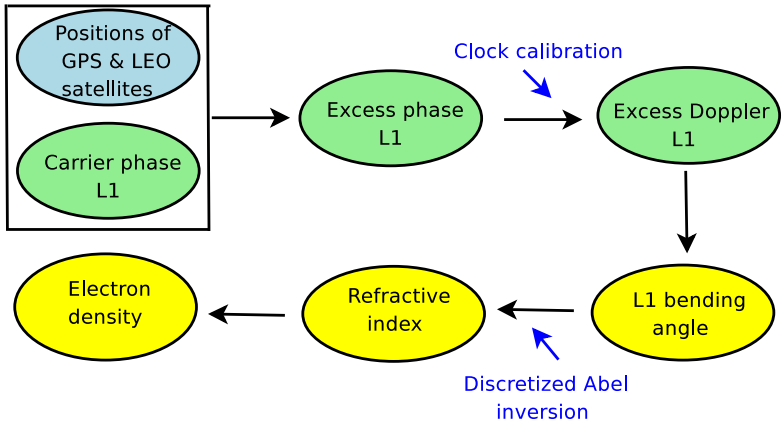

Figure 5.1: *Overall methodology to calculate the input observable (bending angle) from measurements (carrier phase) corrected from clock drifts and application of discritized Abel inversion as described in Figure 4.2. and Eq. 4.32.*

sity, ionospheric scintillation climate monitoring, geodetic research. As already stated, the recent deployment of such constellation has opened new opportunities not only to test different electron density retrieval aspects (old and new implementations) in order to improve radio occultation techniques but also the vast amount of worldwide electron density profiles, about 2500 per day, in front of 500 or 250 approximately per day from previous missions. Electron density profiles can be derived with separability implemented to bending angle. A general overall of the global procedure in provided in Figure 5.1. This method could allow its extension to neutral atmosphere, which is not possible with occultations derived from LI observable. One first result from this study is regarding the excess ionospheric phase calibration, already presented in the previous section. Classically, the clock drift has been removed by double differencing using a fiducial site on the Earth's surface. The suggested double differences by means of a second LEO satellite ([Rocken et *al.* (2000)]) instead of a ground site have been implemented. Nevertheless, subtracting the Lc observable to the main input data, $L1$, is the one finally implemented once their equivalence at ionospheric heights has been shown in Section 3 (see an example in Figure 3.15).

On the other hand, Abel inversion improved with the *Separability* approach can also provide significantly different results even under the present Solar Minimum conditions, compared with spherical symmetry, indicating the convenience of applying such improved technique in any part of the Solar

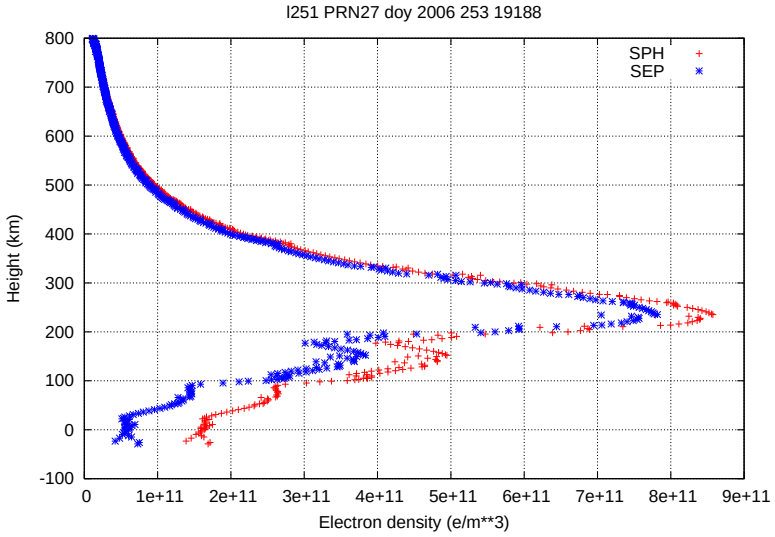

Figure 5.2: *FORMOSAT-3/COSMIC occultation: day 253 of 2006, FORMOSAT-3/COSMIC data, PRN 02 (where PRN stands for GPS satellite identification number), 04h27m UT approx. Improved Abel (with separability) applied to bending angle in blue versus ordinary bending angle approach (spherical symmetry). Note the significantly different results even under the present Solar Minimum conditions.*

cycle (see Figure 5.2).

5.3 Validation of the separability hypothesis

One way to confirm the validity of the separability hypothesis would be to invert series of occultation observations and compare the stability of their electron density profiles versus their shape functions. Such example is provided within the following case study. Let's take into account the situation displayed in Figure5.3, where the map corresponds to $VTEC$ gradients for the 8th of January 2007 depicted over a region around Ascension Island. Co-located density profiles from FORMOSAT-3/COSMIC occultations are also marked in Figure5.3 (12h UT, 13h LT approximately). The corresponding electron density profiles to these occultations are depicted in Figure5.4 (right-hand plot). Notice that such density profiles follow the $VTEC$ behaviour (i.e. higher $VTEC$ gradients lead to higher electron densities). Discrepancies among the profiles shapes are significant. Nevertheless, in the right-hand plot of Figure5.4, when considering the shape functions corre-

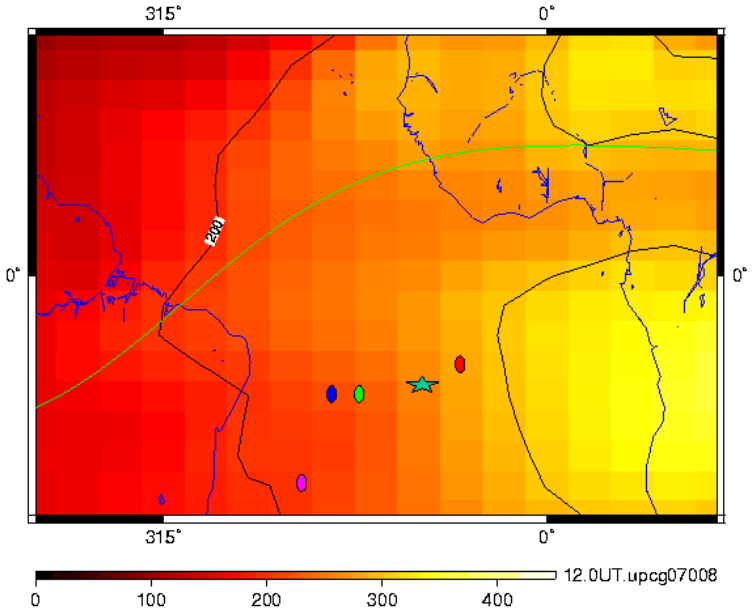

Figure 5.3: *Map of VTEC gradients with co-located vertical electron density profiles from FORMOSAT-3/COSMIC over a region in the vicinity of Ascension Island at 12h UT (13h LT approximately) on January 8, 2007.*

sponding to these profiles, the shapes become closer in value. This fact can be interpreted as the horizontal variations of shape functions are lower than the horizontal variations of electron densities, confirming the suitability of the separability hypothesis. Actually, separability can help mitigate the error in the frequency peak estimation but no the error in height.

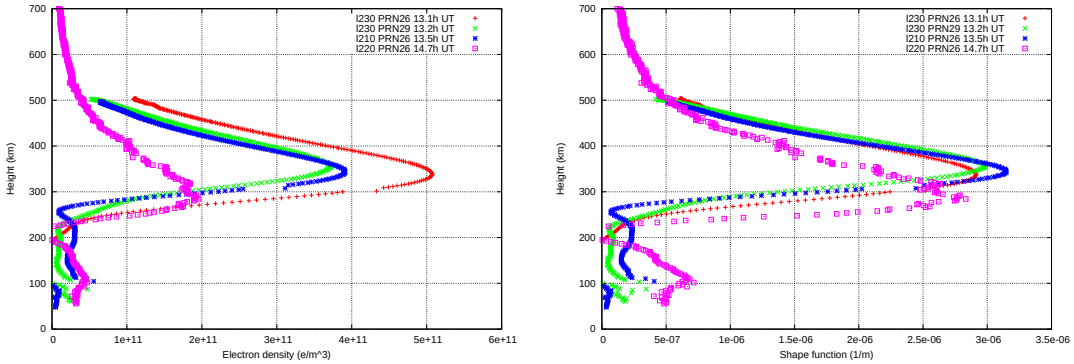

Figure 5.4: *On the left, co-located vertical profiles of electron density from FORMOSAT-3/COSMIC over Ascension Island on January 8, 2007. On the right, shape functions corresponding to co-located vertical profiles of electron density shown on the left-hand plot. For each occultation, in the figure caption, the LEO and GPS satellites involved are given as well as the occurence time.*

5.4 Scenario

The chosen scenario for the analysis of FORMOSAT-3/COSMIC data with the new improved Abel inversion approach spans from January 6th to 15th 2007. By the time the experiment data were gathered, spacecraft 5 and 2 (FM5 and FM2 respectively) were raising their orbits from parking orbit to their final altitude while the other four remained in a parking orbit about 500 km from the surface of the Earth (see Figure5.5). The number of processed occultations per day is provided in Figure5.7 (red line in right-hand plot). Some criteria have been applied to disregard solved occultations as non valid; for instance, the presence of cycle-slips in the retrieved electron density profile, see for instance, the blue density profile in Figure5.13 corresponding to FORMOSAT-3/COSMIC observations is 2006. According to Figure 2.2, which represents the Solar Activity, it corresponds to minimum in values within the solar cycle. The Kp index corresponding to the chosen

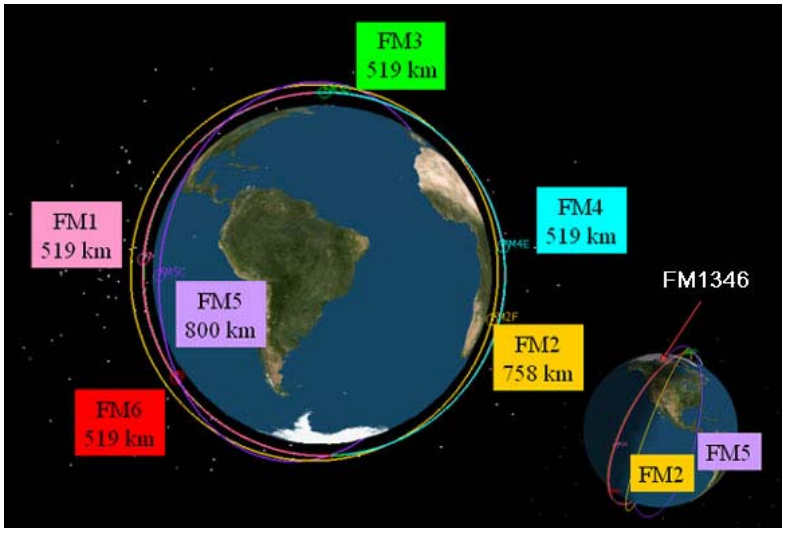

Figure 5.5: *FORMOSAT-3/COSMIC constellation configuration at the time the experiment took place (Jan 6-15, 2007). Courtesy of NSPO.*

period is depicted in Figure 5.6, showing that this period was relatively quiet in terms of geomagnetic disturbances ($Kp < 3$, in the 0 to 10 kp logarithmic scale of geomagnetic activity).

To validate the retrieved electron density profiles from the occulting data, a comparison with parameters provided by direct ionosonde measurements has been performed for frequencies and heights of the $F2$ layer critical frequency, $foF2$, and for frequencies of the E layer critical frequency, foE. The reference data used have been downloaded from the Space Physics Interactive Data Resource (SPIDR) website, available at:
http://spidr2.ngdc.noaa.gov/spidr/. In order to filter and rule out doubtful comparisons, the slab thickness (τ) parameter has been used. It can be considered as a a measurement of the inverse of the shape of the electron density profiles at the $F2$ layer peak and, it is calculated combining $VTEC$ information with ionosonde derived $F2$ layer peak electron density ($NmF2$):

$$\tau = \frac{VTEC}{NmF2} \tag{5.1}$$

Ionosonde measurements with non-realistic values of $NmF2$ have been disregarded. The dispersion of the slab thickness values versus local time is shown in the left-hand plot of Figure 5.7. The valid threshold of slab thickness values has been set from 175 km up to 800 km following similar criteria

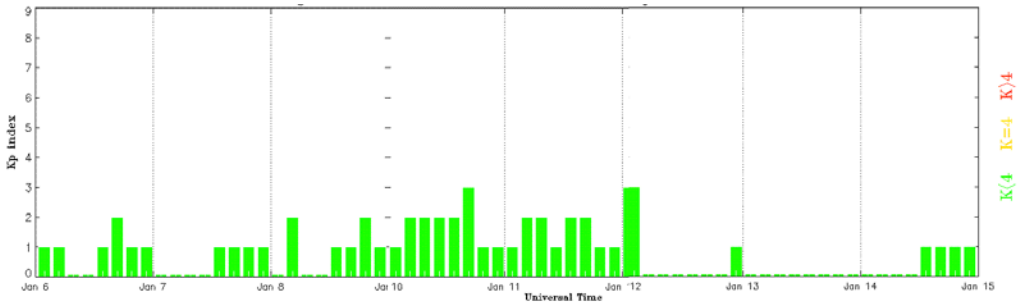

Figure 5.6: *Kp index from January 6th to 15th 2007. Source: NOAA/National Weather Service.*

as in [García-Fernández (2004)]. Recalling the expressions in Eq. 5.1 and Eq. 4.37, it is possible to assign a slab thickness value for a solved occultation at the profile $F2$ peak:

$$\tau = \frac{VTEC}{NmF2} = \frac{VTEC}{VTEC \cdot F(hmF2)} = \frac{1}{F(hmF2)} \tag{5.2}$$

The consistency between ionosonde values of $foF2$ and computed $VTEC$ has been checked.

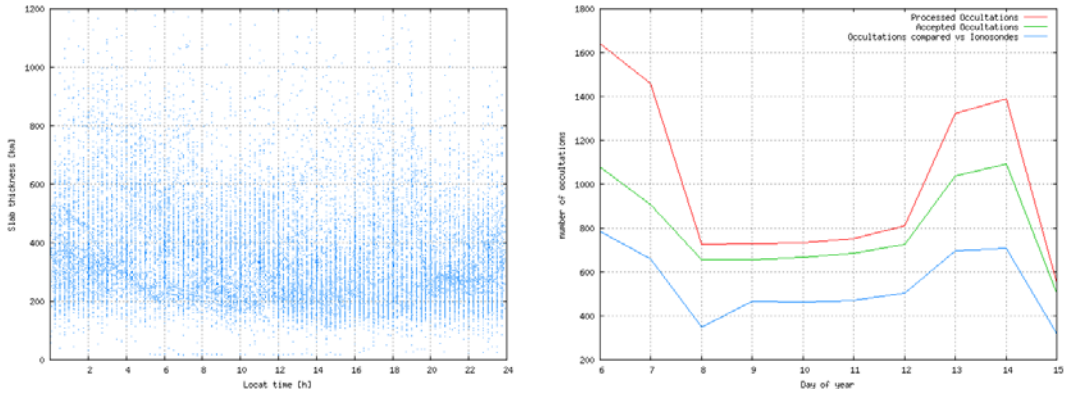

Figure 5.7: *On the left, slab thickness distribution for the period Jan 6-15, 2007. The highest values are found at sunrise and sunset. On the right, number of processed occultations vs. accepted occultations (filtering using slab thickness) vs. final comparisons with ionosondes per day.*

Once filtered by slab thickness, accepted occultations and ionosonde data have been compared with ionosonde measurements co-located in time and

space (see right-hand plot in Figure5.7 for number of final intercomparisons once filtered by slab thickness and co-located with ionosonde): in time, one hour centered at the epoch that the occultation took place and, in space, a maximum co-location distance of 2000km has been considered. Since the subpoints of an ionospheric occultation are scattered over large distances (for a LEO satellite of height $h = 800km$ the maximum lenth of the occultation region is about 3000 km), the co-location is considered at the ray tangent point with the maximum electron density, i.e., maximum frequency $foF2$.

5.5 Experiment results

In the following subsections, the results concerning the comparisons between retreived parameters from radio occultations versus ionosonde measurements are going to be analyzed. Firstly, a local study regarding the use of calibrated data and non calibrated data is going to be presented for occultations in the neighbouring area of Ascension Island. Secondly, global results are shown for frequency and height estimations.

5.5.1 Frequency comparisons: $F2$ layer

Regarding the estimation of the $F2$ layer critical frequency, $foF2$, before attempting global intercomparisons, the availability of manualy calibrated data from Ascension Island ionosonde (code name: AS00Q) has made possible an intercomparison of radio occultations $foF2$ derived frequencies with both, calibrated and non calibrated data in order to validate the expected error for ionosonde data. That is to say, a quantification of the difference in data sources has been possible. Notice that all the intercomparisons that will be presented later in Sect. 5.5.2, Sect. 5.5.3 and the current section for parameters derived from radio occultations density profiles were carried out with ionosonde data from the SPIDR website, in principle, non calibrated.

In Figure 5.8, the relative difference between $F2$ layer critical frequency values is depicted against local time for the analyzed period. It can be observed that the major discrepancies are found during dusk, dawn and at night in agreement with ionosonde worst expected performances.

Figure 5.9 summarizes the comparison of the performance between the spherical symmetry approach of the classical Abel inversion and the separability approach versus non calibrated ionosonda data (considered as reference truth). The results in Figure 5.9 show that the global performance of the separability approach when inverting proofs to be 45% better in average for $foF2$ than the classical Abel transform. Therefore, the introduction of

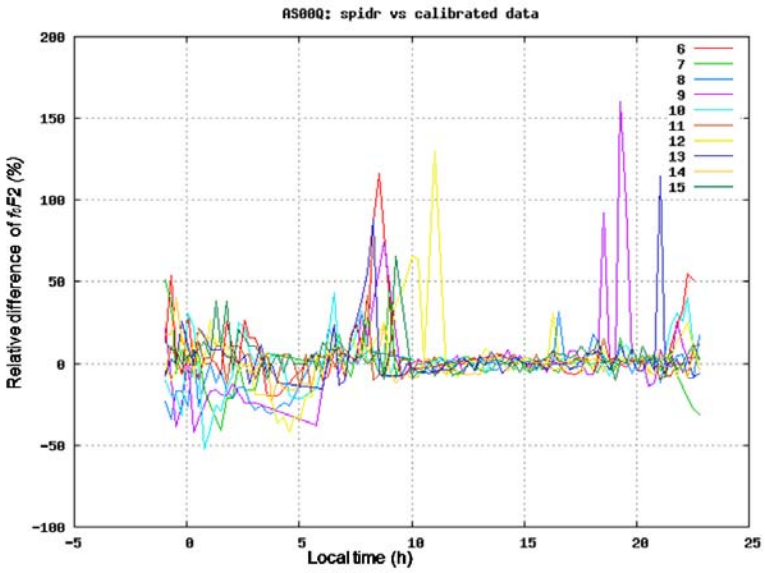

Figure 5.8: *Differences of $foF2$ values in percent versus local time as computed from calibrated and non-calibrated ionosonde data for the period Jan 6-15, 2007.*

$VTEC$ information when retreiving profiles improves the estimations from the ones obtained assuming spherical symmetry, confirming previous results in [Hernández-Pajares et *al.* (2000a)] and [García-Fernández (2004)].

5.5.2 Frequency comparisons: E layer

Regarding the estimation of the E layer critical frequency, foE, the comparative of the two Abel approaches has been studied as well. The E layer is a region of the ionosphere, tipically extending from about 90km to 150km above the Earth's surface which influences long-distance communications by strongly reflecting radio waves in the range from one to three MHz. On frequencies above 10 MHz, it partially absorbs of these waves. In [**?**], it is noted that the E layer appears at sunrise and essentially disappears at sunset (it basically disappears since the primary source of ionization is no longer present). For such reason, the E layer detection has been restricted to check only daytime (local times spanning from 7h up to 17h) electron density profiles, looking for occultations with the presence of a peak in the height interval ranging from 90km up to 130km. A degradation with respect of the $foF2$ results is expected due to the recursive nature of the inversion method:

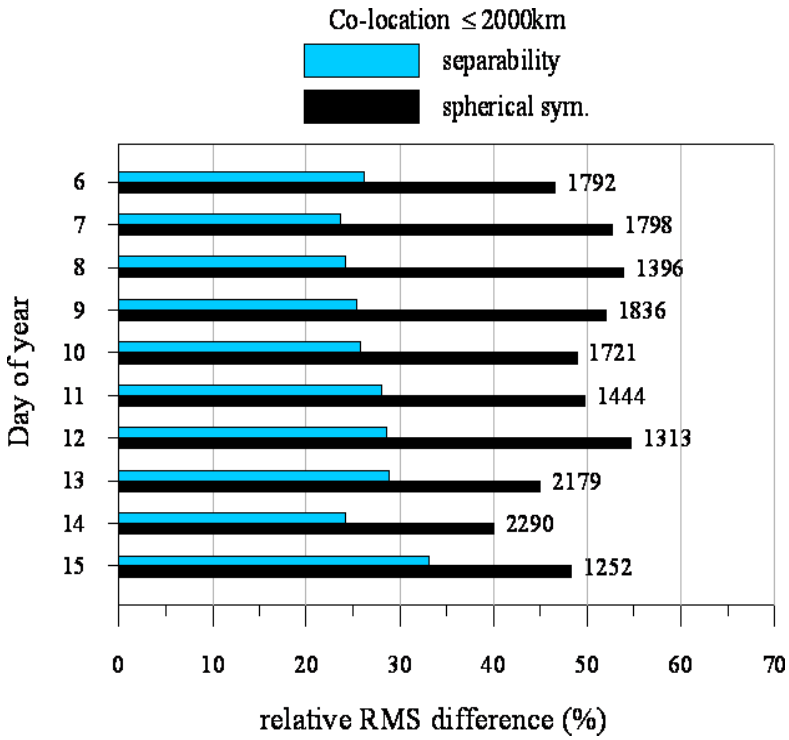

Figure 5.9: *Relative RMS differences for the F2 critical layer frequency comparisons derived from FORMOSAT-3/COSMIC GPS occultation data with ionosonde data colocated at distances up to 2000 km and 1 h time span in local time for the period January 6-15, 2007. Black and blue refer to spherical symmetry and separability, respectively. The numbers of intercomparisons are indicated.*

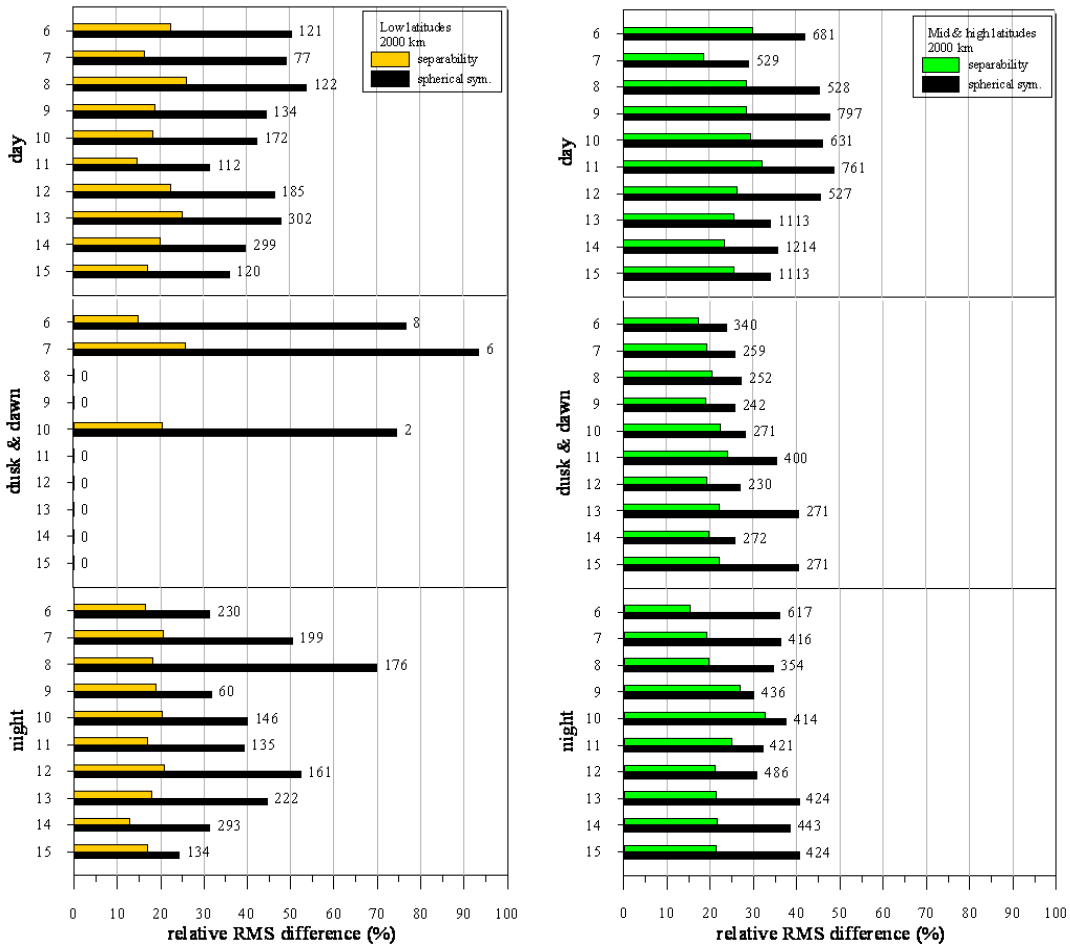

Figure 5.10: *F2 critical layer frequency comparisons versus ionosonde of relative error with co-location distances up to 2000 km for low latitudes (latitude ranges from -30^o to 30^o) -left handside plot- and for mid and high latitudes (latitude ranges from -90^o to -30^o and from 30^o to 90^o) -right handside plot- for each analyzed day. The number of intercomparisons is also provided.*

the errors are acumulated downwards, hence, the lower the layer, the bigger the error in determining its characteristic parameters. Table 5.1 and 5.2 provide global statistics for the analyzed period for co-location distances up to 2000km. Tables 5.1 and 5.2 present the absolute RMS in MHz and the relative RMS difference in square brackets. The number of comparisons is also provided. The average improvement for low latitudes is 32% whereas the average improvement for mid and high latitudes is around 21%.

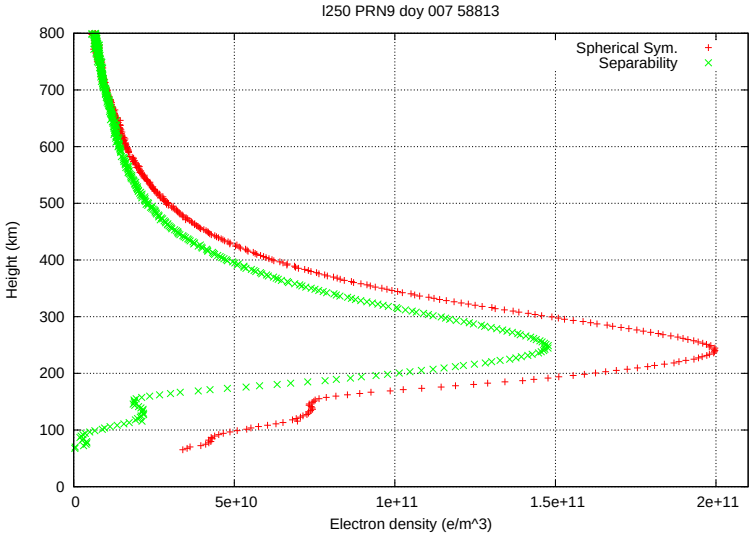

Figure 5.11: *Example of foE frequency peak at latitudes in the neighbourhood of Ascension Island.*

Table 5.1: ***Low latitude*** *comparison of RMS of* ***foE*** *errors for* ***classical Abel*** *(SPH)* ***and separability*** *(SEP) with respect to ionosonde direct measurements for the data period during daytime. The error is the absolute RMS expressed in MHz, and the percentage relative RMS difference is provided in brackets. The number of intercomparisons is also included.*

DOY	Nr. comp.	$RMS_{SPH.}$ [%]	$RMS_{SEP.}$ [%]
006 2007	086	1.51 [47.8]	0.77 [24.2]
007 2007	072	1.85 [51.6]	0.91 [25.4]
008 2007	101	1.59 [45.9]	1.13 [32.7]
009 2007	049	1.53 [43.9]	0.88 [25.2]
010 2007	097	1.63 [49.6]	1.19 [36.2]
011 2007	056	1.32 [40.2]	1.26 [38.2]
012 2007	108	1.75 [52.6]	0.92 [27.8]
013 2007	178	1.50 [44.4]	1.25 [37.0]
014 2007	196	1.59 [47.1]	1.15 [34.2]
015 2007	069	1.18 [35.9]	0.62 [19.0]

Table 5.2: ***Mid and high latitude*** *comparison of RMS of* ***foE*** *errors for* ***classical Abel*** *(SPH)* ***and separability*** *(SEP) with respect to ionosonde direct measurements for the data period during daytime. The error is the absolute RMS expressed in MHz, and the percentage relative RMS difference is provided in brackets. The number of intercomparisons is also included.*

DOY	Nr. comp.	$RMS_{SPH.}$ [%]	$RMS_{SEP.}$ [%]
006 2007	0441	0.84 [32.5]	0.99 [38.0]
007 2007	0599	1.55 [57.3]	1.36 [50.2]
008 2007	0322	1.34 [49.6]	0.88 [32.7]
009 2007	0525	1.33 [46.1]	0.93 [32.2]
010 2007	0411	1.26 [44.7]	1.15 [40.8]
011 2007	0581	1.22 [45.5]	1.03 [38.3]
012 2007	0637	1.32 [49.0]	1.03 [38.3]
013 2007	0846	1.29 [46.8]	0.96 [34.8]
014 2007	1268	1.24 [47.0]	0.82 [31.2]
015 2007	0681	1.21 [46.4]	0.97 [37.4]

5.5.3 Height comparisons

Empirical equations can be applied to some measured ionospheric characteristics in order to derive $hmF2$ values or use $hmF2$ from the true-height analysis of ionosonde measurements. In our study, Dudeney's formula has been used. According to this relationship, $M(3000)F2$ and the ratio $foF2/foE$ are the driver parameters of Dudeneys's $hmF2$ approximation. Such parameters have been also extracted from the SPIDR website. It should be pointed out that the E layer is mainly a day-time ionospheric layer due, basically, to the ionization of the atmosphere caused by solar EUV emission. For such reason, as already mentioned in Chapter 2, some authors restrict the use of expression in Eq. 2.13 to guarantee reliable results for $hmF2$. In this work, the two restrictions imposed in [Rishbeth et *al.* (2000)] have been adopted:

- $M(3000)F2 > 2.5$
- $foF2/foE > 1.7$

which are limiting the number of input ionosonde data for which the $M(3000)F2$ values have acceptable quality (values are especially bad during night time). It is due to this restrictions that the intercomparisons are only provided for daytime. Table 5.3 and 5.4 summarize the results for the

Table 5.3: ***Low latitude*** *comparison of* ***F2*** *layer critical* ***peak height*** *as derived from FORMOSAT-3/COSMIC radio occultations* ***and Dudeney formula*** *for the data period during day time. The results show bias and σ (both expressed in km) for the separability approach versus ionosonde data.*

DOY	Nr. comp.	Bias [km]	σ [km]
006 2007	240	-5.85	20.0
007 2007	214	6.31	12.9
008 2007	245	-18.10	19.5
009 2007	162	14.80	17.4
010 2007	157	18.75	16.1
011 2007	080	25.11	18.4
012 2007	129	12.45	20.5
013 2007	202	-10.98	26.1
014 2007	247	-10.69	17.4
015 2007	114	-7.04	21.0

height comparisons of the $foF2$ peak versus ionosonde data. These results are in agreement with the generally accepted error of the Dudeney formula when applied to ionosonde data (discrepancies of the $hmF2$ estimation below 30km [Zhang et *al.* (1999)]).

The discrepancies in the $hmF2$ determination when using the classical Abel approach are not significative with respect to separability.

5.5.4 LI versus bending angle

The results presented in Tables 5.5 and 5.6 state the equivalence of using any of the two proposed observables for inverting RO data: the linear combination of dual GPS frequencies LI and bending angles (see an example in Figure 5.12) in the case of classical Abel inversion and the improved Abel inversion, respectively. The compatibility of results can be shown for both, classical and improved Abel inversions. This would imply that the assumption of $L1$ and $L2$ travel the same ray path while crossing the ionosphere is not critical for inversion matters (confirmed in comparisons and statistics performed in [Aragon-Angel (2008)]). Nevertheless, the number of successfully solved occultations with bending angle as main datum is much higher than the ones solved with LI due to the presence of cycle-slips. While both techniques are conceptually rather simple, one issue that has to be carefully considered is the detection and correction of measurement errors, such as cycle-slips. Under

Table 5.4: ***Mid and high latitude*** *comparison of* ***F2*** *layer critical* ***peak height*** *derived from FORMOSAT-3/COSMIC radio occultations* ***and Dudeney formula*** *for the data period during day time. The results show bias and σ (both expressed in km) for the separability approach.*

DOY	Nr. comp.	Bias [km]	σ [km]
006 2007	0866	12.13	29.6
007 2007	0680	06.00	25.2
008 2007	0677	10.37	23.4
009 2007	1001	22.72	20.2
010 2007	1053	14.29	26.0
011 2007	1134	06.51	25.5
012 2007	0996	01.70	26.5
013 2007	1709	06.56	33.8
014 2007	1862	05.95	22.2
015 2007	1114	04.57	27.1

Table 5.5: *Global comparisons of* ***F2*** *layer* ***critical frequency*** *discrepancies with ionosondes for co-location distance up to 2000 km for* ***LI vs. bending angles*** *(α)* ***for classical Abel*** *inversion.*

		Nr. comp.	*LI* RMS[%]	α RMS[%]
	Day	216	3.39 [42.7]	3.45 [43.3]
Low	D&D	2	2.15 [56.8]	2.21 [58.4]
latitudes	Night	154	1.87 [44.5]	1.90 [45.4]
	Day	975	2.49 [41.2]	2.57 [42.7]
Mid&high	D&D	144	2.16 [51.1]	2.12 [51.2]
latitudes	Night	730	2.59 [72.7]	2.61 [74.6]

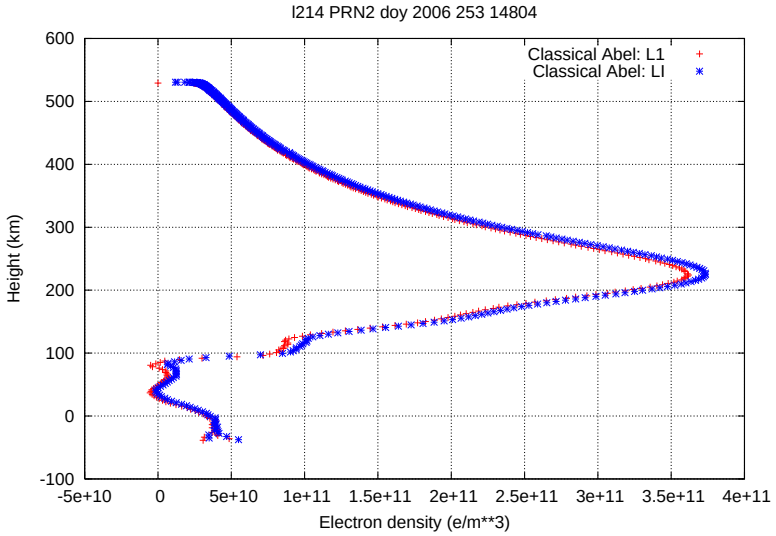

Figure 5.12: *FORMOSAT-3/COSMIC occultation: day 253 of 2006, FORMOSAT-3/COSMIC data, PRN 02 (where PRN stands for GPS satellite identification number), 04h27m UT approx. Abel tranform inverse from LI, and from L1 bending provide compatible electron density profiles.*

Table 5.6: *Global comparisons of **F2** layer **critical frequency** discrepancies with ionosondes for co-location distance up to 2000 km for **LI vs. bending angles** (α) **for improved Abel** inversion.*

		Nr. comp.	*LI* RMS[%]	α RMS[%]
	Day	216	1.53 [19.2]	1.46 [18.4]
Low	D&D	2	0.77 [20.3]	0.78 [20.6]
latitudes	Night	154	0.67 [16.1]	0.70 [16.7]
	Day	975	1.73 [28.7]	1.63 [27.0]
Mid&high	D&D	144	1.44 [34.9]	1.01 [23.9]
latitudes	Night	730	0.84 [24.0]	0.83 [23.2]

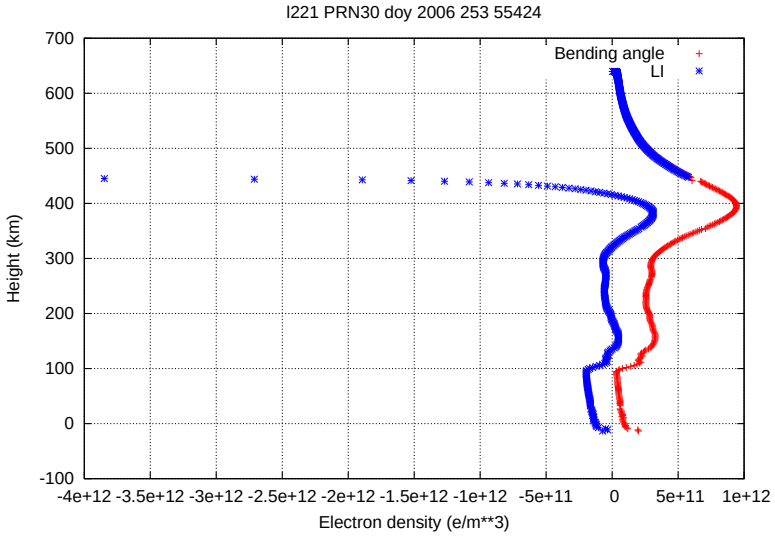

Figure 5.13: *Same occultation solved by using both LI and bending angle: the non-detected cycle-slip does not represent a problem for solving the density profile using the bending angle observable.*

carrier phase cycle-slips, using the bending approach, it is easier to detect and correct them rather than in the case of the LI method because the undetected cycle-slip affect to all the following series of phase measurements, but only to the affected single phase derivation observables (Doppler measurements). For instance, in Figure 5.13, both algorithms have been fed with the same input data, contaminated with one non-detected (hence, not repaired) cycle-slip and the resulting profiles show the robustness of the bending approach. When using the bending angle, even under the presence of a cycle-slip, since the geometry is not varying, the method is able to 'ingest' the cycle slip while when working with LI, a new bias should be calculated (the first observation when performing the recursive solution, is used to determine the bias of LI) or, equivalently, the cycle-slip should be repaired. If the cycle-slip detector in the processing algorithm is too "strict", occultations that could be solved with the bending angle would be rejected.

Chapter 6

Upper Ionosphere estimation

el girasol
no conoce de eclipses
siempre te alumbra
Rincón de haikus- Mario Benedetti

6.1 Introduction

In this chapter, the contribution of the electron content above the LEO orbit is tackled in the inversion process to get the electron density profiles. Actually, it is one important matter that has to be taken into account when inverting RO measurements. One first approximation to the problem is to consider that there is no electron content above the LEO orbit which, for the case of working with the excess Doppler observable as main input, implies that the gradient of the refractive index above the LEO position remains constant and, equals to one at the LEO height, as assumed in previous chapters (see Section 3.3.2):

$$Ne(\vec{r} \geq \vec{r}_{LEO}) = 0 \Longleftrightarrow n(\vec{r} \geq \vec{r}_{LEO}) = 1 \tag{6.1}$$

As already stressed out, to retrieve *accurate* density profiles from ionospheric RO, the contribution of the electron density above the LEO orbit has to be taken into consideration (see Figure 6.1).

This upper electron contribution should be accounted for in a simple but accurate way in order further improve the inversion of the bending angles derived from the GPS observations tracked by the LEO satellite. Although this issue may not be critical for LEOs with nominal orbits above 700 km, it is a crucial point to be considered with lower Earth orbiters. For instance, within the FORMOSAT-3/COSMIC constellation, not all six satellites have been at the same nominal altitude at all times, since, after the launching, some of them remained in a parking orbit while the others were reaching their final destination orbit at about 800 km (see Figure 3.5). Thus the lower the LEO altitude, the bigger the mismodeling error introduced by assuming 6.1.

Another example of Earth orbiter, CHAMP, having an initial nominal orbit of 450 km, it is gradually descending towards 300 km during the mission

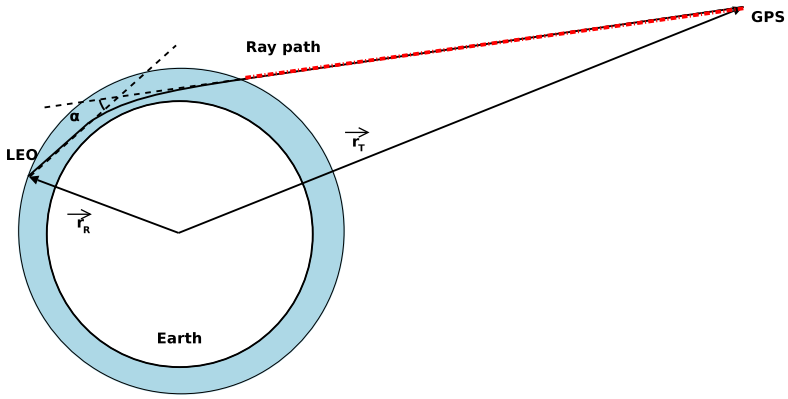

Figure 6.1: *Schematic representation of the upper ionospheric contribution (red) in a RO scenario.*

life-cycle due to the atmospheric drag and, therefore, the upper ionosphere estimation is a decisive matter to consider (see Figure 6.2).

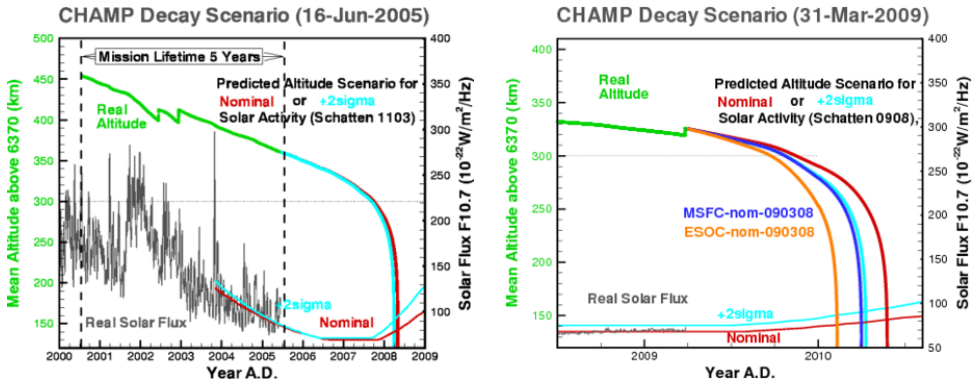

Figure 6.2: *Champ decay scenario: On the left, initial real altitude of CHAMP satellite with life mission prediction. On the right side, updated altitude to year 2009 and expected evolution. Courtesy of GFZ (German Research Centre for Geosciences).*

In the following sections, three approaches to overcome this issue are going to be proposed: firstly, the usage of a climatological model, secondly, an exponential decay, and thirdly, exploiting the separability hypothesis. First of all, a very "controlled" scenario is going to be introduded to test such approaches.

6.2 Scenario: FORMOSAT-3/COSMIC versus Jicamarca DPS

In order to conduct the intercomparisons between results obtained with the two former approaches for the upper electron content contribution, a reliable reference source for electron densities was required. In this sense, supervised Digisonde Portable Sounder (DPS) measurements at Jicamarca $(76.9^oW, 12^oS)$ were available for the whole year 2007 with a sample rate of fifteen minutes. This high quality real data offers a valuable possibility to perform the proof of concept and the comparison of the inverted electron density profiles using the presented approaches for the upper ionosphere estimation. Moreover, there is practically no co-location error with respect location since the ionospheric profiles from Jicamarca DPS have been compared with extremely close co-located FORMOSAT-3/COSMIC profiles: Only when the tangent point of the FORMOSAT-3/COSMIC profile is located in the range of $9-15^oS$ and $73.9-79.9^oW$, then the FORMOSAT-3/COSMIC profile is selected to be compared with the corresponding digisonde profile (see Fig. 6.3). By tangent point it is understood the tangent point at the F2-peak height of the FORMOSAT-3/COSMIC profile. Regarding temporal co-location, a time span of 15 minutes has been considered around the RO time of occurrence to allow comparisons with Jicamarca DPS measurements.

Three consequences of this tight co-location are derived:

- There is no spatial mismatch error with respect to the truth to compare.
- There is a temporal mismatch error limited by the fifteen minute co-location with respect to the truth to compare.
- The truth comes from calibrated real data helping to assess the performances under real circumstances.

Consequently, since the most important sources of errors are not present in this environment, this study will give an overview of the goodness of each approach itself (i.e. the best performance one can expect from each of them).

The experiment data correspond to a one year period, 2007 (approximately 220 highly co-located occultations have been deeply studied). GPS data from FORMOSAT-3/COSMIC satellites were processed with the aid of the global VTEC maps computed and distributed at UPC in IONEX format for such period. These maps provide the required information of the horizontal variation of the electron density to perform improved Abel inversion.

For Jicamarca:

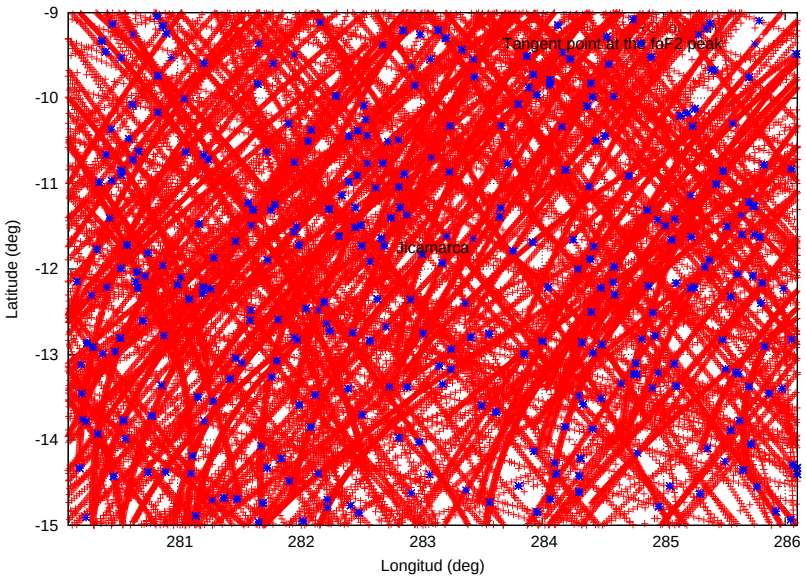

Figure 6.3: *In red, footprints of FORMOSAT-3/COSMIC radio occultation data corresponding to the selected profiles. In blue, tangent points at the F2-peak height of the selected FORMOSAT-3/COSMIC profiles. Jicamarca DPS (*76.9^oW*,* 12^oS*, dip latitude:* 1^oN*) is located in the center of the lattice.*

- Daytime is approximately from 6 to 18h LT (11-23 UT)
- Post-sunset period is approximately from 19 to 21h LT (24-02 UT)
- Nighttime is approximately from 22 to 5h LT (03-10 UT)

In order to rule out doubtful intercomparisons, the slab thickness (τ) parameter has been used. For the ionosonde measurements, it is calculted combining the corresponding VTEC information with the ionosonde derived $F2$ layer peak electron density, $NmF2$. For a solved occultation, it is also possible to assign a slab thickness value recalling the expression in Eq. 5.2. In the lower pannel of Fig. 6.4, it is shown the consistency between the slab thickness derived from ionosonde and radio occultation measurements for all year 2007. Note the dependency on the local time: there is a marked peak around 4h LT and both derived slab thicknesses follow the same oscillation pattern along the year. In the upper pannel of Fig. 6.4, it is shown the consistency for all year 2007 between $foF2$ measurements from ionosonde and derived from inverted radio occultation measurements (with both, classical (green) and improved (red) Abel inversions). Note again the dependency on

Table 6.1: *Neglected upper contribution: Global comparisons of $F2$ layer critical frequency discrepancies with ionosondes for co-located RO with Jicamarca DPS: bending angles (α) using separability vs. classical Abel inversion.*

	Nr. comp.	Improved Abel inversion Bias +/- σ [Rel. RMS %]	Classical Abel inversion Bias +/- σ [Rel. RMS %]
Day	102	-0.2 +/- 0.4 [6.3]	-0.1 +/- 0.4 [6.4]
D&D	22	0.1 +/- 0.5 [9.2]	-0.1 +/- 0.5 [9.7]
Night	15	0.0 +/- 0.4 [8.8]	-0.1 +/- 0.6 [13.3]
Global	139	-0.1 +/- 0.4 [6.9]	-0.1 +/- 0.5 [7.4]

local time: there is a marked valley around 4h LT. Also notice the opposite behaviour of the slab thickness and $foF2$ dependency with respect local time around 4h LT.

6.3 No upper ionospheric contribution

Table 6.1 summarizes the frequency comparison with the $F2$ peak layer when neglecting the upper electron content above the LEO orbit (see Eq. 6.1). In all cases, the improved Abel transform inversion improves the results of the classical Abel inversion, specially during local night time. There is a negative bias always present in the classical Abel inversion results. In Figure 6.5, some examples of electron density profiles derived from FORMOSAT-3/COSMIC data versus co-located Jicamarca digisonde measurements are provided. No upper ionospheric contribution has been considered to invert the RO data.

6.4 First approach: Climatological model

A possible solution to the upper ionosphere and plasmasphere issue is found in [Jakowski et al., 2002] or [Jakowski et al., 2003], where the inversion is assisted with a "first" guess extracted by a Chapman layer model for the topside ionosphere. In this study, the NeQuick model is going to be used in order to provide the first value of electron density at the starting point of the radio occultation, which will be conveniently transformed into the corresponding refractive index value.
Procedure: Considering the actual geometry and epoch of the occultations (i.e real line-of-sights), the NeQuick model is run for the upper observation

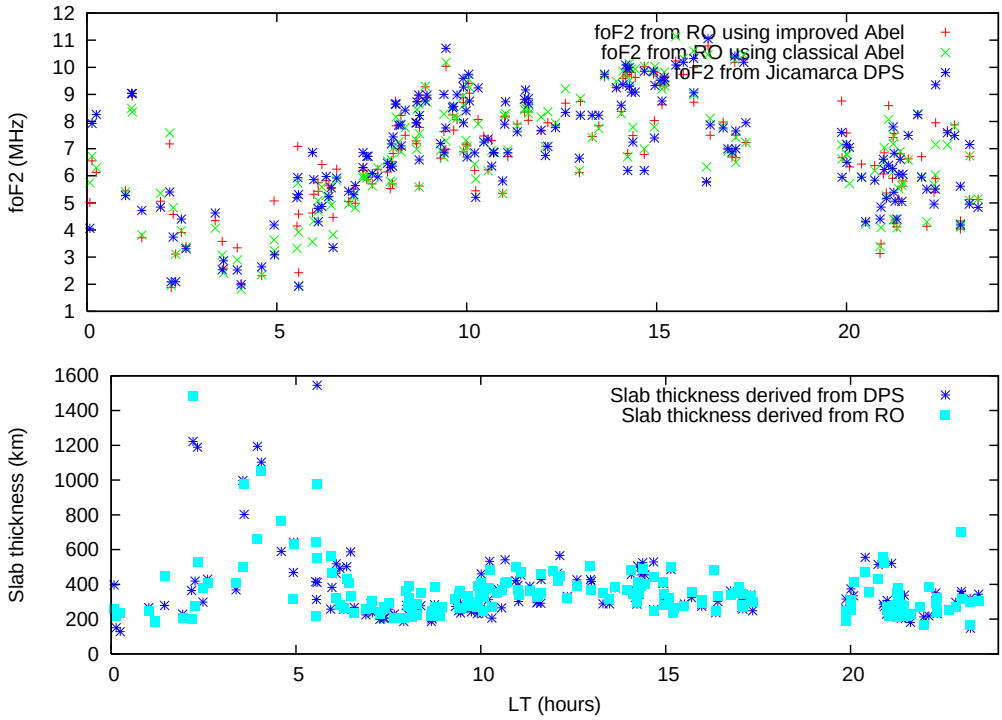

Figure 6.4: *Upper plot: Dispersion of the critical frequency of the F2 layer versus local time throughout 2007 at the neighbourhood of Jicamarca: In red, $foF2$ derived from FORMOSAT-3/COSMIC radio occultations by means of the improved Abel inversion. In green, $foF2$ derived from FORMOSAT-3/COSMIC radio occultations by means of the classical Abel inversion. In blue, Jicamarca DPS $foF2$ measurements. Lower plot: Dispersion of the slab thickness versus local time throughout 2007 at the neighbourhood of Jicamarca: In light blue, slab thickness values derived from radio occultation inverted profiles. In dark blue, slab thickness values derived from Jicamarca DPS measurements.*

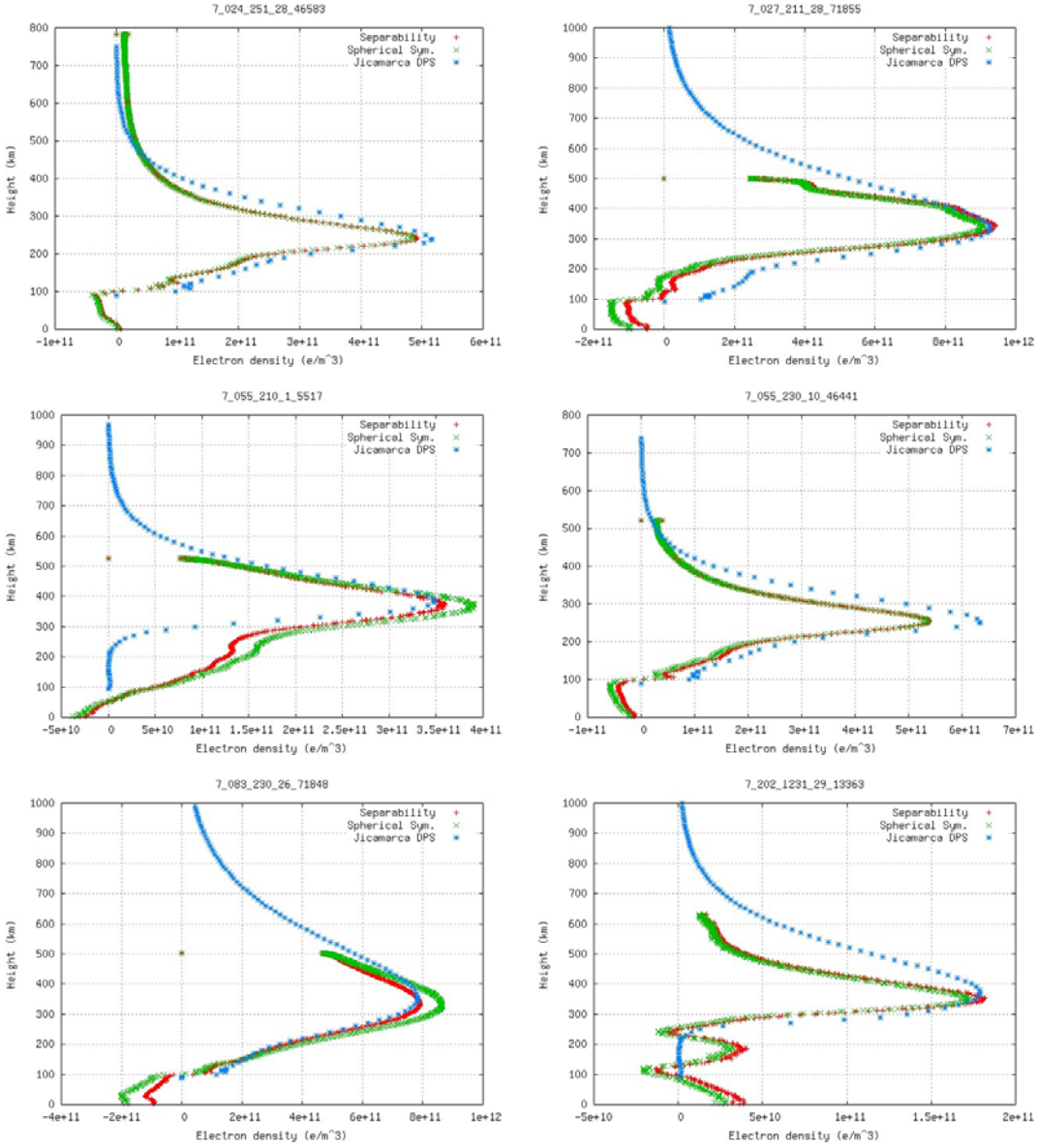

Figure 6.5: *Examples of electron density profiles derived from FORMOSAT-3/COSMIC data versus co-located Jicamarca digisonde measurements. These series belong to the whole year* 2007 *intercomparison introduced in Section 6.2. with no upper ionospheric contribution considered.*

(the one corresponding to the hightest impact parameter) and the electron density for such point is obtained. Once this initial value is calculated, the

Table 6.2: *Climatological model: Global comparisons of F2 layer critical frequency discrepancies with ionosondes for co-located RO with Jicamarca DPS: bending angles (α) using separability vs. classical Abel inversion.*

	Nr. comp.	Improved Abel inversion Bias +/- σ [Rel. RMS %]	Classical Abel inversion Bias +/- σ [Rel. RMS %]
Day	93	-0.1 +/- 0.4 [6.0]	0.0 +/- 0.5 [6.5]
D&D	20	0.0 +/- 0.5 [8.4]	-0.1 +/- 0.6 [11.4]
Night	18	0.0 +/- 0.4 [9.7]	0.0 +/- 0.6 [13.0]
Global	131	0.0 +/- 0.4 [6.7]	0.0 +/- 0.5 [7.8]

inversion is performed by means of both, classical Abel inversion and Improved Abel inversion and the global profile of electron density is retrieved. The peak of the electron density (i.e. NmF2) and its corresponding height (i.e. hmF2) are extracted from these new profiles and compared with the co-located values provided by Jicamarca. These results can be also directly compared with the original inversion presented in Section 6.2 with the a priori assumption of no upper contribution from the ionosphere above the LEO position. Table 6.2 summarizes the frequency comparison with the $F2$ peak layer. In all cases, the improved Abel transform inversion improves the results of the classical Abel inversion. There is a slight improvement regarding results in Table 6.1 during local day and dusk/dawn, although they worsen during local night for separability. The opposite behaviour is found for spherical symmetry results. The negative bias always present in the classical Abel inversion results has now been compensated.

6.5 Second approach: Exponential decay

Another approach to the problem of determining the upper contribution of the ionosphere to the derived profiles would be by performing an exponential extrapolation of the profile as done in [Hernandez-Pajares et al., 2000] or, alternatively, in the input data as in [Hajj and Romans, 1998]. According to [Schreiner et al., 1999] this approach of exponential extrapolation is more appropriate than the use of a climatological model since this may not be accurate enough. The extrapolation that has been performed to the shape functions $F(h)$ is by means of an exponential decay:

$$F(h) = A \cdot e^{-\frac{h}{h_m}} + B \tag{6.2}$$

Table 6.3: *Exponential decay: Global comparisons of $F2$ layer critical frequency discrepancies with ionosondes for co-located RO with Jicamarca DPS: bending angles (α) using separability vs. classical Abel inversion. RMS thershold set to $4e^{-8}$.*

	Nr. comp.	Improved Abel inversion Bias +/- σ [Rel. RMS %]	Classical Abel inversion Bias +/- σ [Rel. RMS %]
Day	83	-0.2 +/- 0.4 [6.0]	-0.1 +/- 0.4 [6.2]
D&D	12	0.1 +/- 0.5 [9.1]	-0.1 +/- 0.5 [9.4]
Night	14	0.2 +/- 0.3 [8.1]	0.0 +/- 0.6 [13.5]
Global	109	-0.1 +/- 0.4 [6.6]	-0.1 +/- 0.5 [7.5]

where h_m stands for the *scale height* and is the factor that controls the rate of decrease and, B stands for a bias. In principle, since the shape function has to become zero when the height h tends to infinite, the constant B should be subtracted from the original profile and the exponential fit to guarantee the resulting shape function has a vertical asymptote.This bias B is thought to take into account the fact that the topside (protonospheric contribution) is basically constant and would not contribute to the bending since it is based on increments of refractive index. As first trial, three equidistant points from the original profile (located above the F2-layer peak) were used to perform the extrapolation. Nevertheless, due to sudden changes in convexity/concavity of the profiles, the lack of data or abrupt jumps, the success of the extrapolation was not guaranteed for a reasonable number of profiles. For this reason, the strategy to extrapolated was made more robust by performing several extrapolations to the same profile using different triad of points to anchor the extrapolation. A RMS value was assigned to each of these extrapolations, and by setting a threshold to the RMS, a program would statistically best fit them into one final solution of parameters A, h_m and B for the given initial profile.

Table 6.3 summarizes the frequency comparison with the $F2$ peak layer. In all cases, the improved Abel transform inversion improves the results of the classical Abel inversion. It should be noted that there is a worsening for the classical Abel performance when becoming more restrictive with the RMS threshold.

6.6 Third approach: using the separability nature of the electron density

The fact that the electron density can be expressed by means of a shape function F assuming the height dependency and the VTEC associated to the corresponding horizontal coordinates as reflected in Eq. 4.37, implicitly implies that the integral value of the shape function along the ray path should be one:

$$\int F(h)dh = 1 \tag{6.3}$$

This integral expression can be discretized, hence becoming:

$$\sum F(h)\Delta h = 1 \tag{6.4}$$

It should be pointed out that, if no scheme for the upper plasmaspheric contribution is used, some error is introduced (it could reach up to several TECU, $\lessapprox$ 10 TECU). When using separability by means of Eq. 4.37, the unknown to be solved is F and, actually, when working with the bending angle, the solution to the system is not F but ΔF, that can be solved recursively after providing an initial value of F at the highest height. For a first approach to the problem, the initial value is set to zero, that is to say, the gradient of the refractive index is considered to remain constant in the upper layers of the ionosphere. Nevertheless, the current aim is to provide a more realistic initial value for the recursive solution. Taking into account that ΔF is a discrete function, consecutive differencing of F values can expressed as:

$$\Delta F_i = F(h_{i+1}) - F(h_i) \tag{6.5}$$

assuming in this expression that $h_1 > h_2 > ... > h_n$ being n the total number of input data. Therefore, the actual $F(h_i)$ values can be derived from the knowledge of ΔF and the initial $F(h_1)$:

$$F(h_i) = F(h_{i-1}) + \Delta F_{i-1} = F(h_1) + \sum_{k=1}^{i-1} \Delta F_k \tag{6.6}$$

Using this expression for each $F(h_i)$ and replacing them into Eq.6.4, consecutive terms with opposite signs will be cancelled out, remaining only the ones appearing in the following expression:

$$F(h_1)(h_1 - h_n) + \Delta F_1(h_2 - h_n) + ... + \Delta F_{n-2}(h_{n-1} - h_n) = 1 \tag{6.7}$$

Form this expression, $F(h_1)$ value can be deduced:

$$F(h_1) = \frac{1}{h_1 - h_n}[1 - \sum_{i=1}^{n-2} \Delta F_i(h_{i+1} - h_n)] \tag{6.8}$$

Applying this constraint to RO measurements, the statistical results showed no agreement with digisonde data. In Figure 6.6, it is depicted the resulting profile using Eq. 6.8 for a previously solved density profile. The new profile (red) is far to the right, meaning that the initial value for the shape function was too big. This red profile would lead to unrealistic TEC values for the profile when integrated. The conclusion is that the integral value of the shapes functions is quite smaller than one as assumed in Eq. 7.7. At this

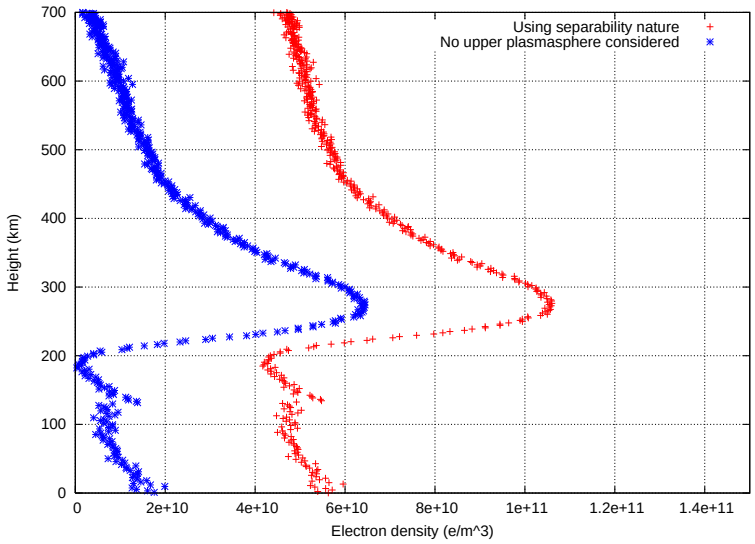

Figure 6.6: *Example of profiles with no plasmasphere vs. using nature of separability.*

point, we questioned how the distribution of the integral values of the shape functions was for the analyzed data set in Chapter 5 (more than 17000 solved RO). In Figure 6.7, a histogram with the value of the integral expressed in Eq. 7.7 is depicted for the shape functions of derived density profiles from FORMOSAT-3/COSMIC corresponding to several days in January 2007. As one can see, most of the integrals values are far from the hypothetical value of one. As commented before, there are LEO satellites from the FORMOSAT-3/COSMIC constellation at different orbits. One first interpretation of Figure 6.7 could be that the lower LEOs are the ones presenting the lower values of the integral. Nevertheless, Figure 6.8 shows that, independently of the LEO

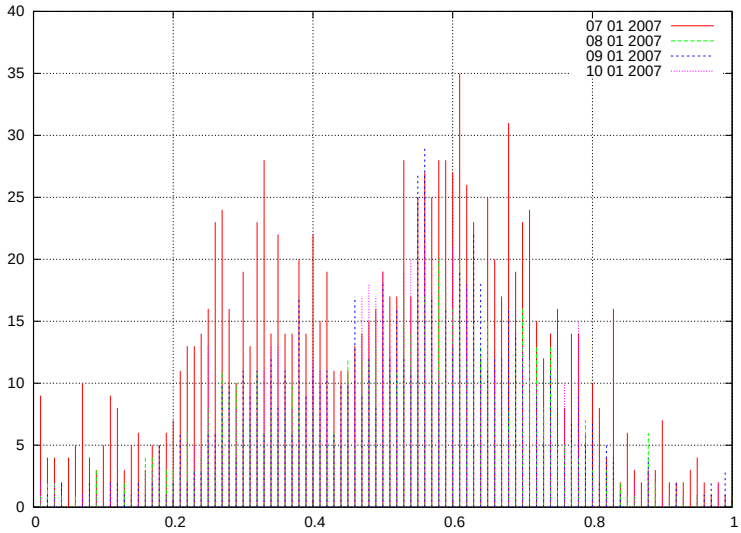

Figure 6.7: *Histogram of the values of the integral of the shape function for several days in January 2007 from data of the FORMOSAT-3/COSMIC constellation .*

satellite, the distribution of the integral values still ranges from the lowest values up to the highest, not explaining the unexpected lower values for the integral. Looking back at Figure 6.7, an underdetermination of the integral values is evident. Since the separability hypothesis related shape function and VTEC, an underdetermination of the shape function could be driven by high VTEC. For this reason, in the IONEX maps, which originally the effective height is set to 450 km for the STEC deprojection, we tried some other possibilities: 300 and 200 km respectively. The resulting VTEC were used to feed the inversion process of RO in the data set of Chapter 5. The results are shown in Figure 6.9 where it can be stated a little drift to higher values of the integral of the shape function when using lower effective heights when projecting from STEC to VTEC.

Trying to understand the two modal distribution of the values of the integrals of the shape function in Figure 6.7, they were plotted versus longitude and latitude. No clear dependendy was found with respect longitude (uppler plot in Figure 6.10), whereas a clear marked latitudinal dependence was found (lower plot in Figure 6.10). At this point, we also questioned if it could have any seasonal dependence. For this reason, for a given day (January $6^{th}, 2007$), it was considered the day half a year later. Figure 6.11 shows the clear seasonal dependence found. This opened a new lead to our research that will be analysed in next chapter.

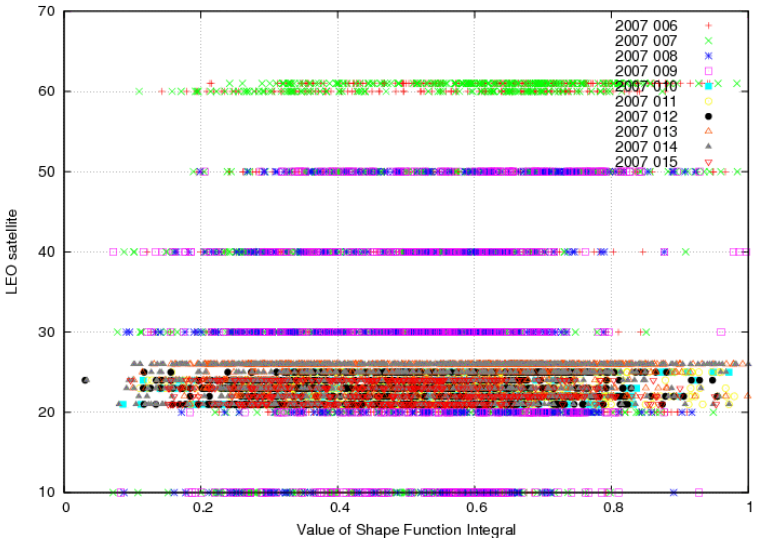

Figure 6.8: *Histogram of the values of the integral of the shape function with respect the different LEO heights in the FORMOSAT-3/COSMIC constellation for several days in January 2007.*

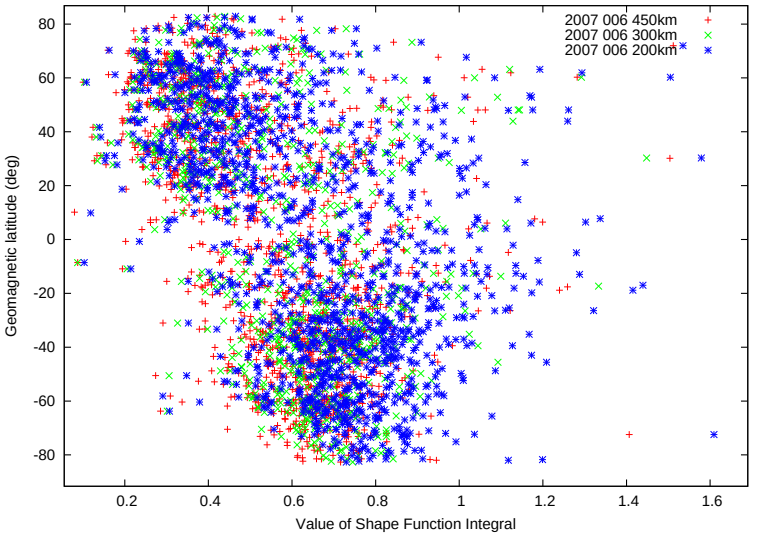

Figure 6.9: *Comparative of the values of the integral of the shape function for different heights (200, 300 and 450 km respectively) when projecting from STEC to VTEC.*

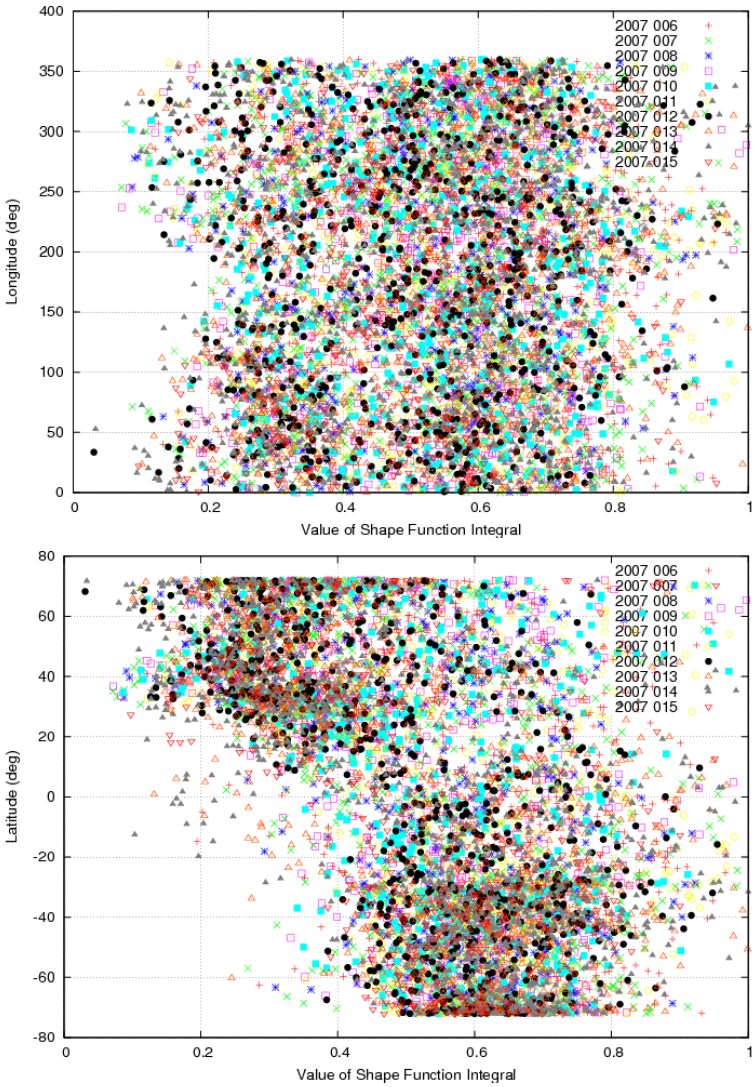

Figure 6.10: *Comparative of the values of the integral of the shape function versus longitude and latitude. There is no clear dependency with respect longitude (upper plot), while there is a marked latitudinal dependence (lower plot).*

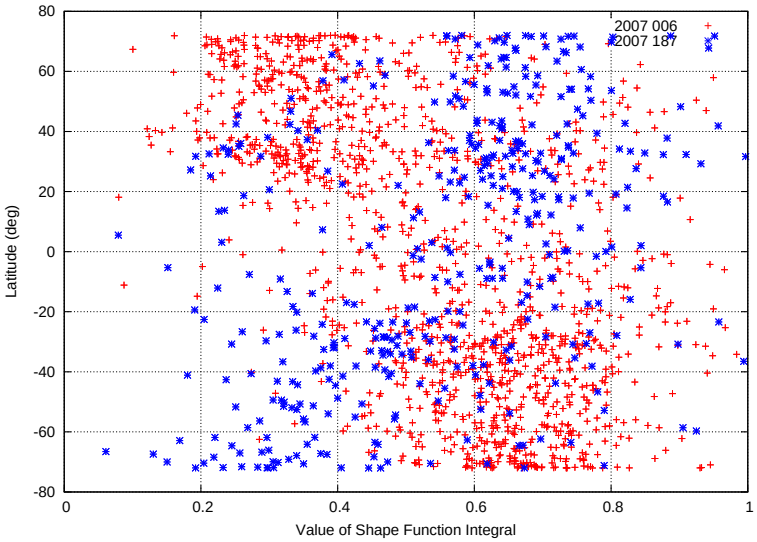

Figure 6.11: *Seasonal dependence of the integral of shape functions. The figure depicts the values of the integral of the shape functions for January* $6^{th}, 2007$ *and half a year later.*

Chapter 7

Towards a mapping function derived from RO

Los niños hallan el todo en la nada;
los hombres, la nada en el todo
Giacomo Leopardi

7.1 Introduction

Due to the inconsistency found at the end of previous chapter, a study of ionospheric mapping function (effective heights) is going to be performed to try and analyse the problem. Based on shape functions derived from GNSS RO data, it is possible to derive mapping functions, the obliquity factor that allows converting VTEC into STEC.
In this chapter, a simple improvement to geometric mapping functions has been developed where the only free parameter (besides the elevation angle) is the ionospheric effective height (h_{eff}). The effective height can be defined as the height of an infinitessimal virtual thin layer that contains all the electron density and can model the STEC from VTEC. The proposed new mapping function basicaly consists of adjusting h_{eff} to what would correspond to the user's time and location (longitude and latitude) instead of using a fixed height as in most current approaches.

7.2 Mapping functions: Overview

By mapping function is understood the obliquity factor that allows converting VTEC into STEC:

$$M = \frac{STEC}{VTEC} \tag{7.1}$$

where STEC is the TEC along the slanted line from the receiver (below the ionosphere) to the transmitter (above it) and VTEC corresponds to the special case of STEC where the ray travels through the ionosphere along the radial direction.

In practice, the conversion from VTEC to STEC is fulfilled by means of a mathematical expression. Actually, the use of an analytical mapping function is clearly an approximation, and can lead to errors of several TECU when applied to regions of large horizontal electron density gradients ([Klobuchar et *al.* (1993)], [Tsedilina and Weitsman (1992)]). Mapping to vertical is necessary if the radial electron density structure is not modeled.

One simple way to define a mapping function is to assume that the overall electron content is concentrated in an infinitesimal thin shell. This is supported by the fact that, although the ionosphere is a highly complex field, it generally tends to have a denser central layer around 400 km above the surface of the Earth. The infinitesimal thin shell would be located above the mean Earth radius and close to the height where the ionosondes detect the higher electron density, the $F2$ region (see Figure 7.1). This approach corresponds to the widely used *thin shell* obliquity factor ([Lanyi and Roth (1988)], [Coco et *al.* (1991)], [Brunini et *al.* (2004)]) to relate slant and vertical TEC:

$$M = \frac{STEC}{VTEC} \approxeq \frac{1}{cosX} = \frac{1}{\sqrt{1 - sin^2 X}} = \frac{1}{\sqrt{1 - (\frac{R_{Earth}}{R_{Earth}+h_m} cos(\epsilon))^2}} \quad (7.2)$$

where ϵ is the elevation angle of the satellite, R_{Earth} is the mean radius of the Earth and h_m is the height of the shell that is usually fixed at a height between 300 and 500 km (for instance, 450 km as in the global ionospheric maps provided by IGS in IONEX format). In this case, M does not depend on ionospheric data, it is purely geometric since it is based on geometrical considerations of the ray path between the transmitter and the receiver. The central approximation of the shell-ionosphere model is to assume that there are no horizontal variations of the electron distribution along the ray-path of the signal from satellite to receiver. The errors involved in this approximation may worsen for low-elevation observations, particularly during dusk local times or in the equatorial regions. In order to map the VTEC over the shell, a sun-fixed coordinate system is adopted. This system is geocentric and rotates westward is such a way that the Sun is contained in the x-z plane, by using local time, latitude and height coordinates. Using this coordinate system, the variability of the ionosphere seen from an Earth fixed coordinate system is almost eliminated [Schaer et *al.* (1998)].

The use of a single shell-ionosphere can introduce a significant and, some times very important, mismodelling that can affect to different applications of GNSS data such as global VTEC determination and precise navigation. For such reason, a tomographic approach to mapping functions was studied in [Hernández-Pajares et *al.* (2005)]. In this work, the feasibility of estimating

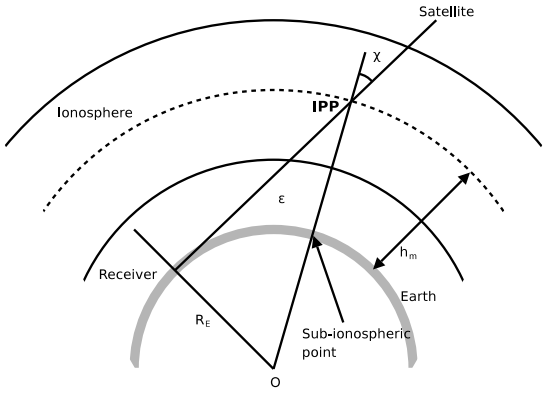

Figure 7.1: *Schematic representation of the single shell-ionosphere located at height h_m above the Earth. The Ionospheric Pierce Point (IPP) corresponds to the point within the transmitter-receiver raypath where the TEC is assigned.*

a more realistic (and accurate) mapping function at global scale was shown, in terms of variable GPS ionospheric effective height derived from data belonging to dual frequency GPS ground stations. An Ionospheric Voxel model (IVM) fed with ground data was used, with several layers (shells), solved by means of Kalman filtering of geometry-free carrier phase measurements. Under this approach, for a given ray of impact parameter p (where p corresponds to a receiver elevation of 20^o):

$$M \approxeq \sum \frac{P_i}{VTEC} \frac{r_i}{\sqrt{r_i^2 - p^2}} \tag{7.3}$$

being P_i and r_i the partial TEC and geocentric distance corresponding to the ith layer. From here, it was possible to derive an effective height, actually, an ionospheric shell height, corresponding to a thin layer fitting to the estimated mapping given in Eq. 7.3, as follows:

$$h = \frac{M}{\sqrt{M^2 - 1}} p - R_{Earth} \tag{7.4}$$

The effective heights derived using this tomographic technique are typically higher than $hmF2$ values due to the asymmetry of the typical vertical profile of electron densities, in particular when considering the topside electron content included in h definition [Hernández-Pajares et *al.* (2005)].

More recently, in [Smith et *al.* (2008)], an assessment of the geometric and numerical errors while using a shell model was made. They deeply studied three cases: An infinitesimal shell model, another with finite thickness shell model and, the use of a spherical shell. From the mathematical and geometrical analysis of the derived expression for M, it was estated that the errors of using a shell model could reach up to 14% even on days of low ionosphere activity. They alternatively propose a "fix" to Eq. 7.2 based on data from the knowledge of the ratio of total error (percent error p) relative to STEC that they calculate for different shell heights with respect different piercing angles at the given shell height (see Table 4 in [Smith et *al.* (2008)]). From the percent error p, defined as:

$$p = \frac{STEC - \frac{VTEC}{cosX}}{STEC} \cdot 100\% \tag{7.5}$$

their proposed mapping function takes the following form:

$$M = \frac{1}{(1 - (\frac{p}{100}))cosX} \tag{7.6}$$

It should be pointed out that this mapping function relies on a known stratification of the ionosphere. Their final recommendation was to model the

ionosphere three-dimensionally to reach higher accuracies, confirming recommendations in [Hernández-Pajares et *al.* (1999)].

7.3 Shape function normalization

As already pointed out, the hypothesis that the electron density can be expressed by means of a shape function F assuming the height dependency and the VTEC associated to the corresponding horizontal coordinates as reflected in Eq. 4.37 (separability hypothesis), implicitly implies that the integral value of the shape function along the ray path should be one:

$$\int F(h)dh = 1 \tag{7.7}$$

In practice, this is not the case for real shape functions. As shown in Figure 6.7, most of the integrals values are far from the hypothetical value of one. From Figure 6.7, an underdetermination of the integral values is evident. This underdetermination, more than being related with a not fulfillment of the separability hypothesis, presents certain incoherence between the VTEC and the RO profile that, as we will show later, is related with the protonospheric contribution to the VTEC (derived from GPS data) and which is basically missing in the RO derived data. The free electron density should equal to the sum of its main constituent ions:

$$N_e(h) = N_{O^+}(h) + N_{H^+}(h) \tag{7.8}$$

These two density distributions have clearly different scale heights: The scale height for the ionospheric distribution lays approximately between 100 and 150 km while the protonospheric distribution has a scale height typically sixteen times bigger (as we will show later). At LEO satellite heights, the LEO satellite basically "sees" $N_{O^+}(h)$ under an occultation scenario (i.e. negative elevations) and the effective heights that we will derived from RO measurements will account only for this share of the total $N_e(h)$. In order to derive the correct effective height, the contribution from $N_{H^+}(h)$ should be added. Actually, the incompatibility between RO-derived TEC and VTEC is the same between effective heights (as shown later in Section 7.7).

For this reason, each shape function has been normalized to its own integral value i.e. the following integral has been calculated:

$$\int F(h)dh = SF_0 \tag{7.9}$$

and the shape function F has been divided by this value, $\frac{F(h)}{SF_0}$, i.e. normalized, hence forcing the integral of the shape function to become one. In Figure 7.2, the corresponding extrapolated and normalised shape functions to a given RO are provided. Such RO correspond to SAC-C data, during May 4, 2002. After performing the extrapolation and normalization to each

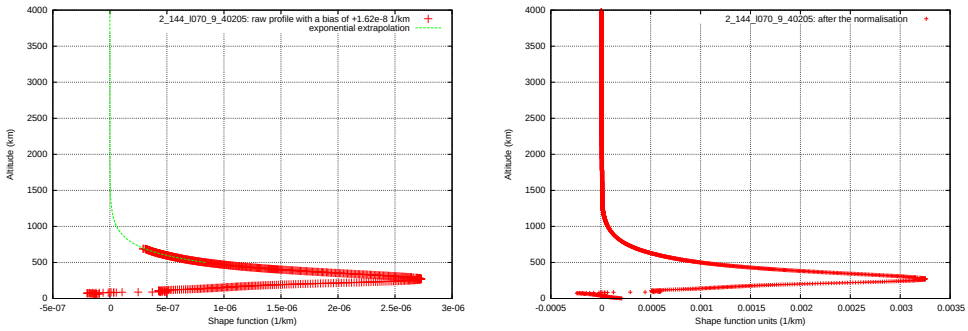

Figure 7.2: *In the left-hand plot, example of normalised shape function corresponding to extrapolated shape function in right-hand plot.*

profile, the longitudinal and latitudinal dependence is mitigated, as well as the dependence regarding to the epoch within the year. In Figure 7.3 several shape functions are depicted once they have been correspondingly extrapolated and normalized. They belong to a set of selected profiles that has been used to deeply study the proposed problem of improving current mapping functions.

Another conclusive parameter showing this lack of dependency is shown in Figure 7.4. In this figure, the slab thickness τ (Eq. 5.1) is represented, which is a first order measure of the shape of the electron density profile. Since we are considering the separability assumption to derive our density profiles (hence, our shape functions), the slab thickness can be also reinterpreted as done in Eq. 5.2, becoming τ the inverse of the shape function evaluated at $hmF2$ for a given profile. From 7.4, it can be determined that in spite of plotting data corresponding to very different ionospheric conditions, locations and times, they all follow the same pattern along the year. Notice that there are higher data dispersion corresponding to local night.

7.4 Analysis of effective heights

At this point, it should be stressed out that, since we are dealing with information from RO events (shape functions), it is $N_{O^+}(h)$ what we can

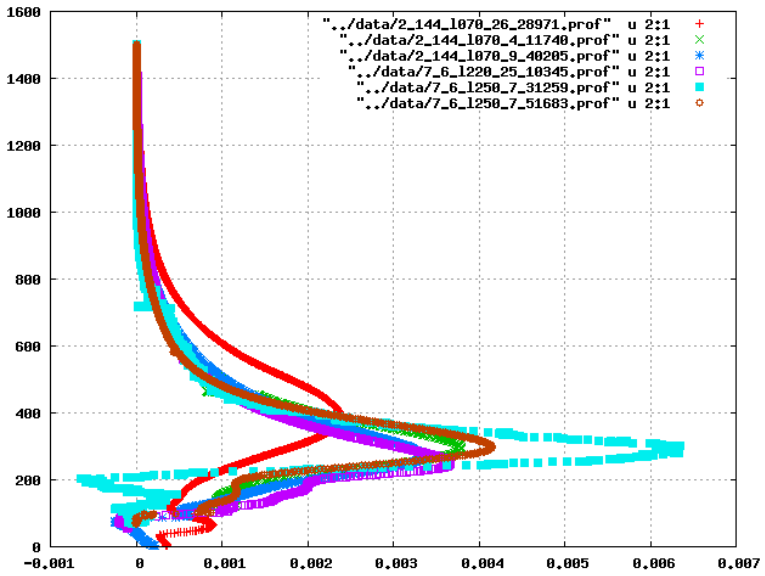

Figure 7.3: *Several examples of entrapolated and normalized shape functions. They correspond to RO retrievals from May 24, 2002 (derived from SAC-C measurements) and January 6, 2007 (from FORMOSAT-3/COSMIC measurements).*

determine from it.

Once the shape functions derived from RO data have been extrapolated and normalized, the mapping function corresponding to a given elevation is simply obtained by tracing a ray with such elevation and calculating the slant integral i.e. the STEC that would be obtained would directly correspond to the mapping function for the given elevation, region and epoch. By tracing rays at different elevations, the corresponding mapping functions would be had (see several examples of these mapping functions in Figure 7.5) and, by means of Eq. 7.4, their effective heights would be obtained. This would give a procedure to calculate a mapping function associated to a given RO profile.

In Figure 7.6, the relationship between effective height and elevation is shown for three shape profiles belonging to the supervised data set in Figure 7.3: two of them belonging to the data set in 2002 (SAC-C) and one to 2007 (FORMOSAT-3/COSMIC). The slab thickness τ (introduced in Chapter 5) is also provided for each profile. It is an important parameter since it is intimately related with the rate of variation of the effective height with respect elevation: the higher the value of τ, the bigger the gradient of effective

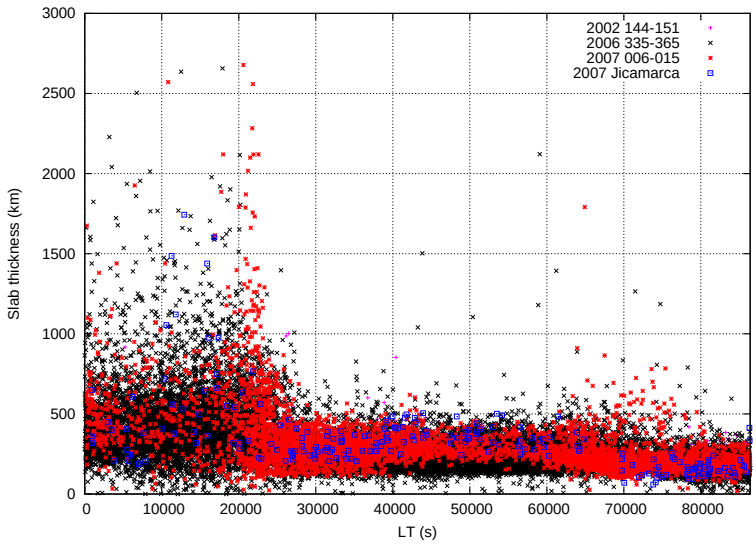

Figure 7.4: *Slab thickness dependency versus local time for different epochs (even different years).*

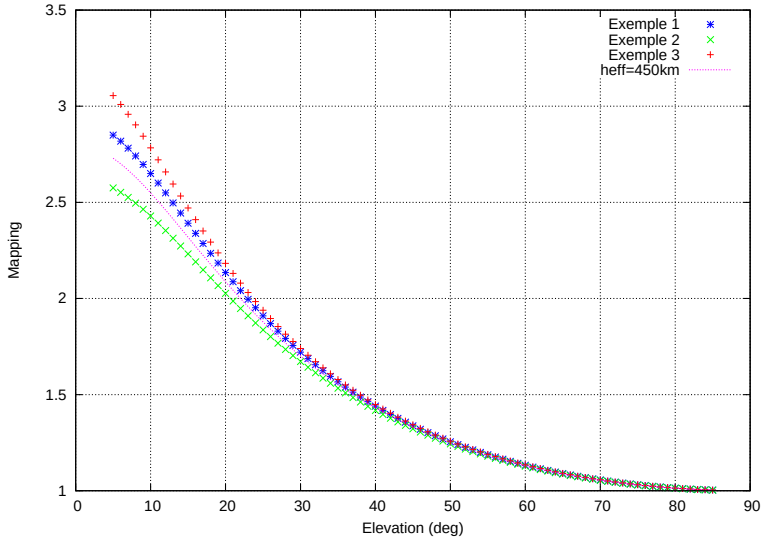

Figure 7.5: *First RO-derived mapping functions: mapping function vs. elevation. The mapping function with effective height set to 450 km is also depicted for comparison.*

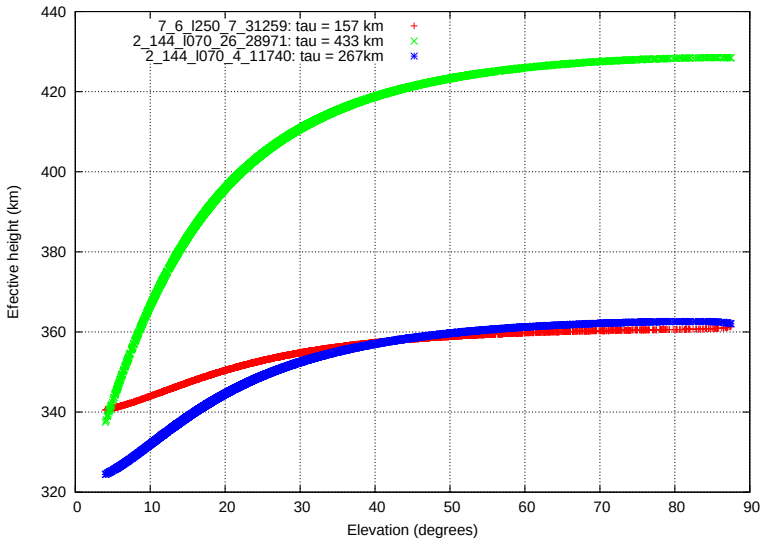

Figure 7.6: *Dependence of the effective height with elevation for three given shape profiles (red, green and blue points with slab thickness of 157, 433 and 267 km, respectively).*

heights with regards elevation. Looking at Figure 7.6, the smallest τ (red line) implies Δh_{eff} of 20 km whereas the biggest τ (green line), Δh_{eff} of 90 km. This fact is evidenced in Figure 7.7, where it has been represented the difference of effective heights at two given elevations (80^o and 30^o) versus slab thickness for several shape profiles from the supervised data set. Moreover, if we pursue to model the ionosphere with a infinitesimal thin shell with one associated effective height, from Figure 7.6, we can see that there is an inherent error in such consideration, due to the dependence to elevation and the gradient in the corresponding heights. In the case of the blue and red curves, the error would be less than 20 km in assigning one effective height but in the case of the green curve, it would be bigger. Nevetheless, the slab thickness τ allow us to evaluate such variation. Figure 7.7 shows that there is a proportionality between the variation in effective heights by elevations versus slab thickness allowing to model such variation.

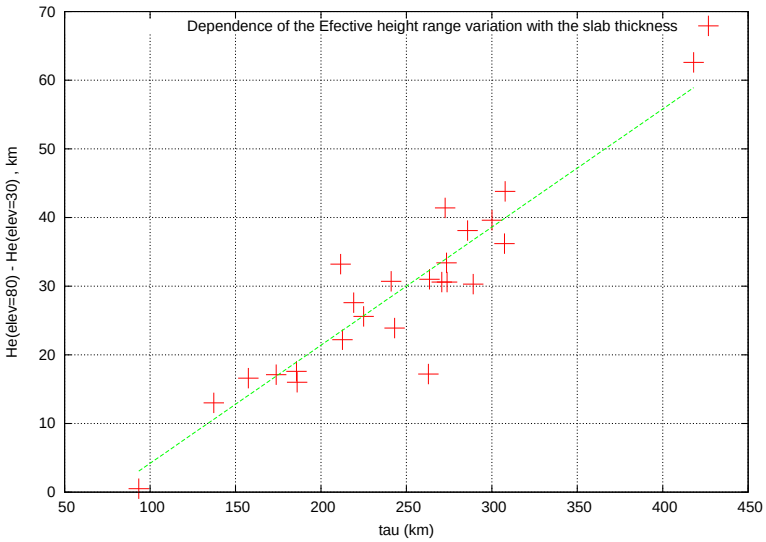

Figure 7.7: *Relationship of the dependence between effective heights and elevations versus slab thickness.*

7.5 Analysis of the interdependency of $hmF2$ and h_{eff}

Independently of Figure 7.6, after an exhaustive study of the data sets[1], a clear relationship between the height of the F2 layer peak, $hmF2$, and the associated effective height, h_{eff}, has been found (see Figure 7.8). In Figure 7.8, one can see the linear dependence of $hmF2$ and h_{eff} for a given elevation angle of 10^o. The linear fit to the data has been included in the plot. By means of this relatioship, provided a value of the peak height of the F2 layer ($hmF2$), one can derive an effective height associated to each RO. And based on this relationship, the proposed mapping funtion is going to be implemented.

[1]Profiles corresponding to May 24 to 31, 2002 retrieved from SAC-C; profiles from December 1 to 31, 2006, profiles from January 6 to 15, 2007 and profiles from the whole year 2007 colocated with Jicamarca DPS from FORMOSAT-3/COSMIC. These sets add up to approximately 18000 profiles, 14400000 observations.

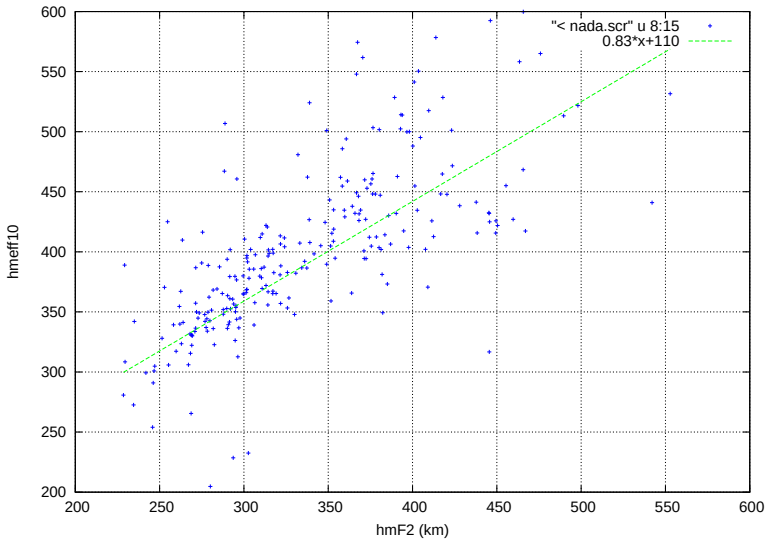

Figure 7.8: *The peak height of the F2 layer $hmF2$ versus derived effective height at an elevation angle of* 10^o.

7.6 Proposed Improved Mapping Function (PIMF)

To try and develop an improved mapping function obtained from shape functions derived by RO data inversion, two options could have been followed:

- If a continuous and uniform distribution of LEO satellites was available (obviously, with the capability to provide GNSS RO data), a map of effective heights could be derived from the shape function profiles, provided they were firstly interpolated and, secondly, normalized.
- Using archive data of the history of $hmF2$. Taking into account that the evolution/distribution of $hmF2$ is well described in several works, if a relationship between $hmF2$ and h_{eff} could be established, then h_{eff} would be derived from the knowledge of $hmF2$.

The latter option is the one that has been pursued in the current study, hence the analysis presented in Section 7.5. Actually, the proposed solution relies on providing more suitable h_{eff} (from $hmF2$ and the relationship with h_{eff}) but keeping the mathematical expression for the mapping function in Eq. 7.2 (h_{eff} as hm).
The Proposed Improved Mapping Function (PIMF) is based on the previous knowledge of the evolution/distribution of $hmF2$. The main program calculates $hmF2$ from CCIR coefficients adapted to our needs from NeQuick

and from here, h_{eff} is provided as final output. The program internally calculates:

- Modified dip latitude (MODIP): In [Rawer (1994)], it was proposed a new coordinate for modeling the F2-layer and the top-side ionosphere, adapted to the real magnetic field, e.g., to the magnetic inclination (dip). This coordinate is now called modified dip or MODIP μ and is defined by the following equation:

$$tan\mu = \frac{I}{cos\phi} \tag{7.10}$$

  where μ is the modip latitude, I is the true magnetic dip usually at a height of 350 km and ϕ is the geographic latitude. MODIP equator is the locus of points where the magnetic dip (or inclination) is 0^o. In the equatorial zone, the lines of constant modip are practically identical to those of the magnetic inclination but as latitude increases they deviate and come nearer to those of constant geographical latitude. The poles are identical to the geographic ones. The MODIP parameter is necessary in order to calculate $M(3000)F2$ coefficients, derived from the 10^{th} Generation of International Geomagnetic Reference Field (IGRF) released by the International Association of Geomagnetism and Aeronomy (IAGA), 10^{th} version of a standard mathematical description of the main magnetic field of the Earth. It is required to be updated every five years 5 years. New update available soon at $http://www.ngdc.noaa.gov/IAGA/vmod/igrf.html$.

- Solar flux ($F10.7$): It is used as the basic indicator of solar activity, and to determine the level or radiation being received from the Sun. The solar flux is closely related to the amount of ionization and hence the electron concentration in the F2 region. For our purposes, $F10.7$ is taken from the file R12.dat (belonging to NeQuick software distribution). Nevertheless, the program allows this index to be introduced as an extra parameter obtained from any other reliable source.

- $M(3000)F2$: these parameters are derived from the subroutine CCIR, which calculates the coefficients of the development of CCIR around the corresponding MODIP).

- $hmf2$: As a first approach, the Shimazaki formulation is going to be used (Eq. 2.12) to derived $hmF2$ from the $M(3000)F2$ parameters (typical overestimate in the day time 15 to 40 km at mid and low latitudes althought it could exceed 60 km at higher latitudes in summer).

But any other reliable formulation to derive $hmf2$ could be used such as Dudeney's (Eq. 2.13).

- h_{eff}: From Section 7.5, the relationship between $hmF2$ and h_{eff} is known. Therefore, knowing $hmF2$, we can derive the corresponding h_{eff}.

7.7 Testing

At this point, now that a new improved mapping function (PIMF) has been suggested based on the analysis of data sets of shape functions, some testing should be conducted in order to validate the proposed solution. Two kinds of data are going to be used:

- Simulated data
- Real data

The design of the different tests has not been trivial since the testing should point out the differences of using one particular effective height (hence, mapping function) versus another choice of effective height for the same conditions. In the next section, the chosen testing is going to be presented.

7.8 Test plan

The combination of GPS observables that is going to be used as the main driver for the testing is the Ionospheric combination LI. Basically, when simultaneous carrier phase observations in both frequencies ($L1$ and $L2$) are subtracted, the satellite-receiver geometrical range and all frequency independent biases are removed. The principal characteristic of LI is that it cancels out the geometric part of the measurement (geometry free linear combination), leaving the ionospheric effect and the instrumental constants (besides multipath and observational noise). The Ionospheric combination between receiver i and satellite j can be expressed as follows, assuming that the win-up is very small in size, and can be corrected or neglected:

$$LI_i^j = \alpha \cdot STEC + DCB_i + DCB^j + b_i^j \tag{7.11}$$

where α is 0.105 $\frac{m}{TECU}$, $STEC$ stands for the electron density integrated along the slant path of the signal from the receiver to the satellite, DCB_i and DCB^j are the so-called differential code biases due to electronic delays

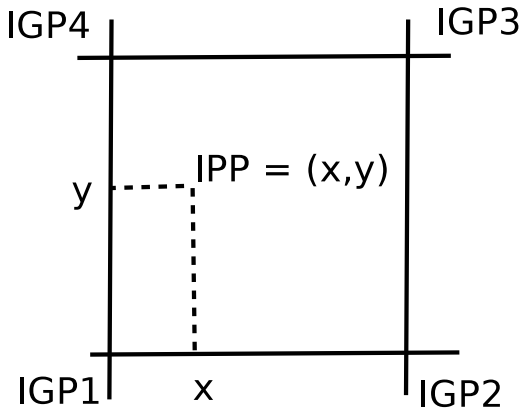

Figure 7.9: *IPP from the studied ray with respect the closest IGPs.*

in the receiver i and satellite j hardware respectively, and b_i^j is a constant related with the carrier phase ambiguities in both frequencies. In this expression, the DCB are explicitly written with respect to Eq. 1.8.

Once a particular receiver station has been chosen to carry out the comparisons, by means of a geodetic program, the phase ambiguity b_i^j can be determined thanks to the very good knowledge of station coordinates and overall modeling:

$$LI_i^j = \alpha \cdot STEC + DCB_i + DCB^j \tag{7.12}$$

The remaining terms DCB_i and DCB^j are always correlated. If we take DCB_i from the receiver as reference, then it can be assumed that DCB_i is zero. Therefore, the expression in Eq. 7.12 becomes:

$$LI_i^j = \alpha \cdot STEC + DCB^j \tag{7.13}$$

In order to solve Eq. 7.13, the data are LI_i^j and the system needs to be inverted assuming:

$$LI_i^j = \alpha \cdot M \cdot TEC + DCB_i + DCB^j \tag{7.14}$$

where TEC is calculated from the Ionospheric Grid Points (IGPs) which are the four closest to the Ionospheric Pierce Point (IPP) of the ray (see Figure 7.9). In practice:

$$STEC = M \cdot (\gamma_1 TEC_1 + \gamma_2 TEC_2 + \gamma_3 TEC_3 + \gamma_4 TEC_4) \tag{7.15}$$

where α_i correspond to the fraction of TEC_i at the ith IGP contributing to the interpolated TEC. The coefficients α_i have the following explicit form when considering the lenght of the grid to be one, corresponding to a second order Taylor expansion):

$$\gamma_1 = (1-x)(1-y) \tag{7.16}$$

$$\gamma_2 = x(1-y) \tag{7.17}$$

$$\gamma_3 = xy \tag{7.18}$$

$$\gamma_4 = (1-x)y \tag{7.19}$$

7.8.1 Simultated data: tests

The main advantage of testing simulated data is that TEC and DCBs are known, therefore it is very straight forward to calculate the error introduced by using the proposed mapping function. For ilustrative purposes, one RO from SAC-C satellite has been selected to present the plots corresponding to the tests. This particular RO took place during May 24, 2002, while tracking PRN 24 around 11h UT.
Figure 7.10 shows the evolution of the effective height with respect elevation. If all the ionosphere was concentrated in a thin shell layer, the effective height would be constant and its value would correspond to the height of such layer. In Figure 7.10, one can see the variation of the effective height with respect elevation reveals the mismodeling of the vertical distribution of TEC, the asymmetry of such distribution. From Figure 7.10 it can also be stated that the variation of the corresponding effective heights to each elevation are less than 50 km. Therefore, in this particular case, the impact of assigning one effective height to all elevations should not be critical provided the selection of such effective height follows some reasonable criteria.

In Figure 7.12, Figure 7.13 and Figure 7.14, the evolution of the error in the TEC and DCBs calculated by using 450, 360 and an adaptative effective height respectively is shown. In these plots, the expected value for the DCBs should be zero and, for graphical matters, one has been substracted to VTEC (it makes the intercomparison easier). When a mistake in the assignment of the effective height is made, there is an incorrect distribution between the values of VTEC and DCBs (see Eq. 7.13). It is clear that using an effective height of 360 km reduces the error in both, TEC and DCBs determination with respect the use of 450 km (which is the effective height used in IONEX global ionospheric maps). This value of 360 km is compliant with the expected value for h_{eff} derived from RO shape functions. If we go one step

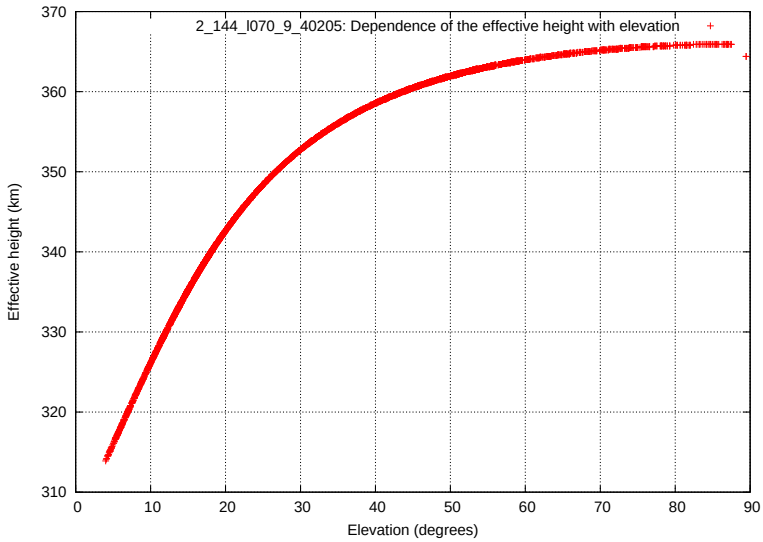

Figure 7.10: *SAC-C RO taken place during May 24, 2002, while tracking PRN 24 around 11h UT. The figure shows the typical dependence of the effective height with respect elevation.*

further an use an adaptative effective height as presented in Figure 7.11, the error is reduced again.

Therefore, if the electronic distribution was as the one provided by occultations, the effective height derived from a single-layer model would be enough.

7.8.2 Real data: tests

The main disadvantage of testing real data is that there is no prior knowledge of the real TEC and DCBs values, forcing new tests to be developed. The testing has been carried out the in-house WARTK software (see for instance [Hernández-Pajares et *al.* (2000b)]). From Eq. 7.13, the test plan for real data can be laid out:

- **Test A**: DCBs test for a given station
- **Test B**: Using $LI_i^j - \alpha \cdot STEC - DCB_i - DCB^j$ (post-fit test)
- **Test C**: Using single differences of LI_i^j minus modeled $\alpha \cdot STEC$ (by means of the corresponding mapping function) between different receiver stations and the same satellite. We will have to confirm the stability of such difference i.e. the difference of DCBs between the two ground stations.

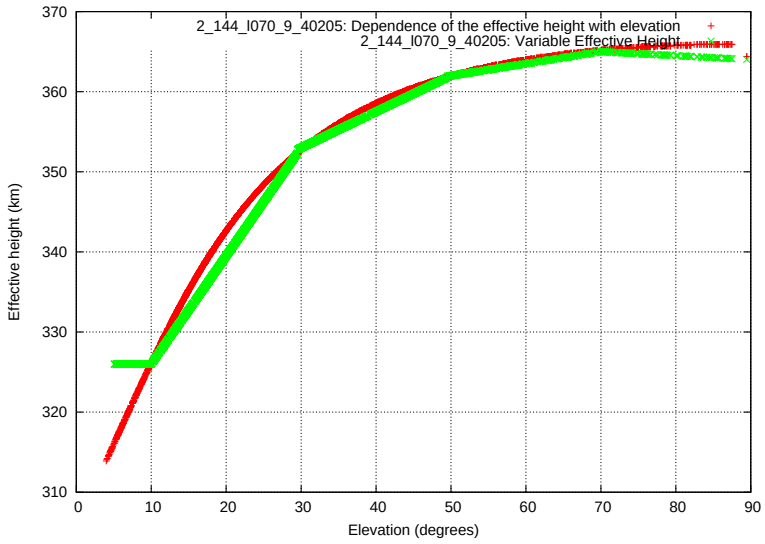

Figure 7.11: *SAC-C RO taken place during May 24, 2002, while tracking PRN 24 around 11h UT. The figure shows the selected variable effective height (green) versus the real depence (red) with respect elevation.*

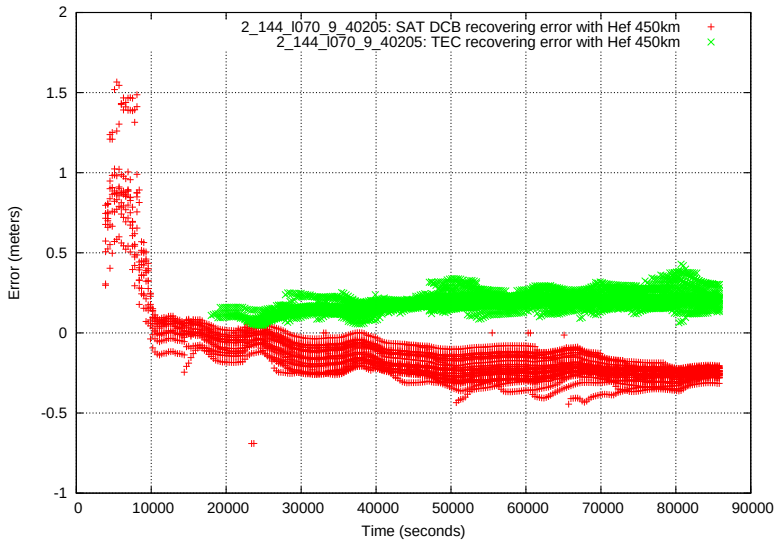

Figure 7.12: *SAC-C RO taken place during May 24, 2002, while tracking PRN 24 around 11h UT. For an effective height set to 450 km, the figure shows the error while recovering TEC (green) and satellite DCBs (red).*

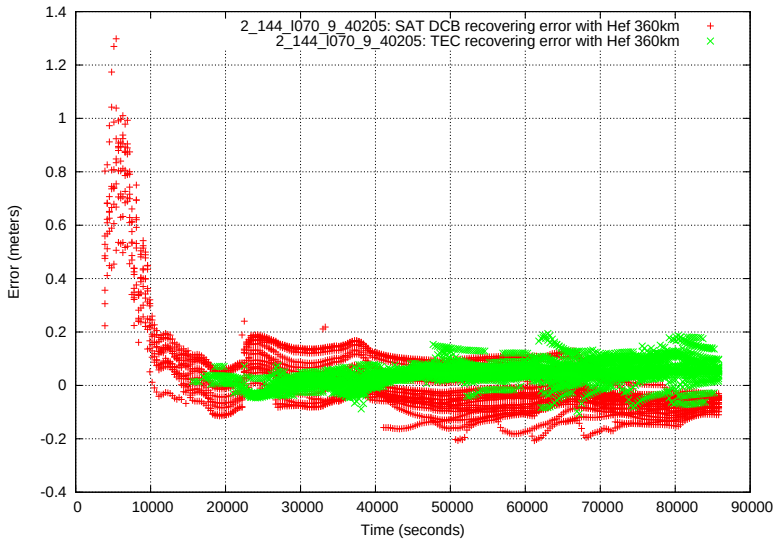

Figure 7.13: *SAC-C RO taken place during May 24, 2002, while tracking PRN 24 around 11h UT. For an effective height set to 360 km, the figure shows the error while recovering TEC (green) and satellite DCBs (red).*

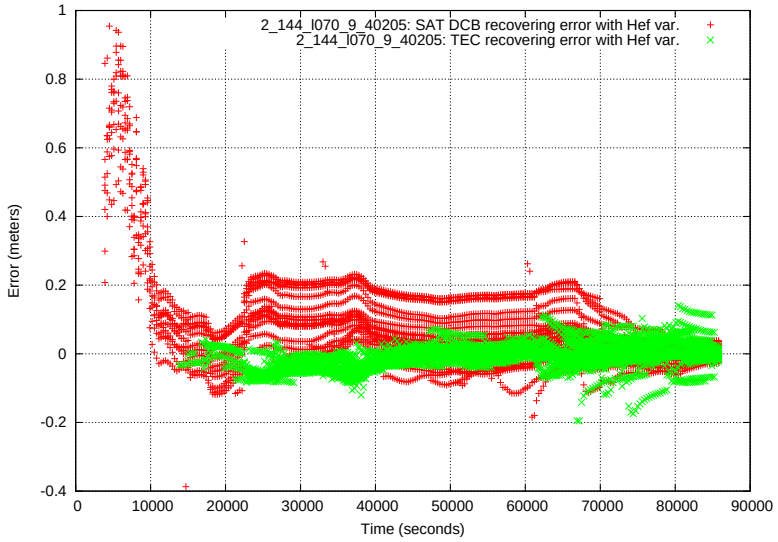

Figure 7.14: *SAC-C RO taken place during May 24, 2002, while tracking PRN 24 around 11h UT. For a case of varible effective height, the figure shows the error while recovering (green) and satellite DCBs (red).*

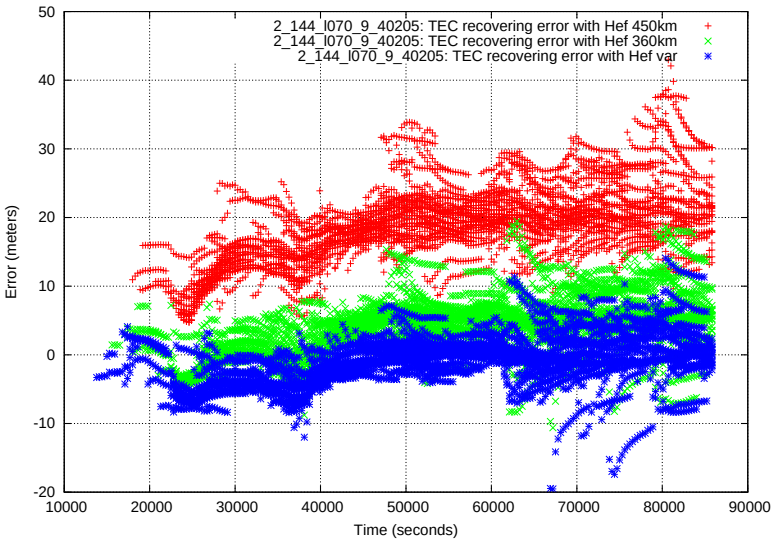

Figure 7.15: *SAC-C RO taken place during May 24, 2002, while tracking PRN 24 around 11h UT. The figure shows the intercorparison of the error while recovering TEC for fixed (450 km and 360 km, red and green) and variable effective height (blue).*

Scenario

The analysed day is January 7, 2007 and shape profiles retrieved from FORMOSAT-3/COSMIC measurements have been used. In Figure 7.16, the distribution of the locations of the F2-layer peak is depicted along with the ground stations used to process the geodesy in order to determine the phase ambiguities b_i^j in Eq. 7.11. Actually, from this global distribution, the data that has been finally chosen come from an area over Canada and from three stations in Europe in the same latitude band (see Figure 7.17). In this area, there is a densification of ground stations which is crucial in order to estimate the ionosphere (these stations are going to be used to solve the ionospheric tomographic model). The list of code names for these stations belonging to the IGS network are: BREW, ALGO, CHUR, WILL, FLIN, SASK, PICL, PRDS, NLIB and, in Europe, BRUS, TLSE, NPLD. The information regarding the maximum height of the F2 layer derived from RO data and, we have guaranteed enough RO around this area in order to be able to estimate $hmF2$. In Figure 7.28, it is depicted the fitting of the value of $hmF2$ versus local time for the region in Figure 7.17.

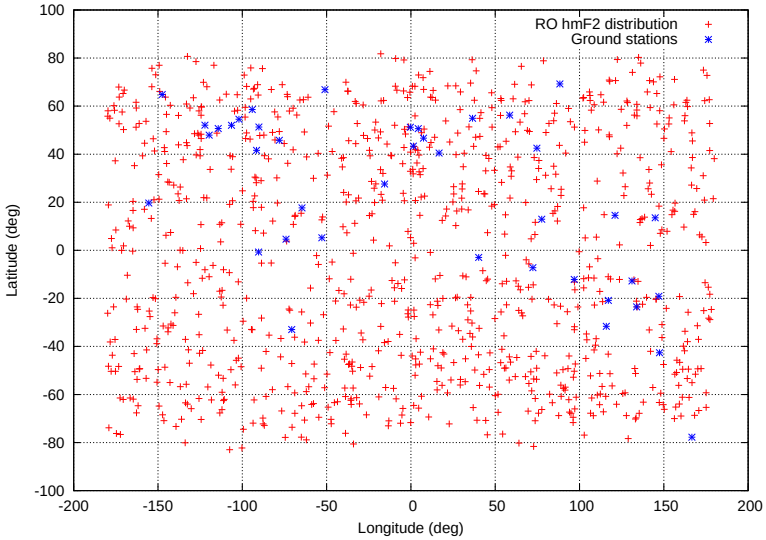

Figure 7.16: *Distribution of RO hmF2 for January 7, 2007 and ground stations used for geodetic processing.*

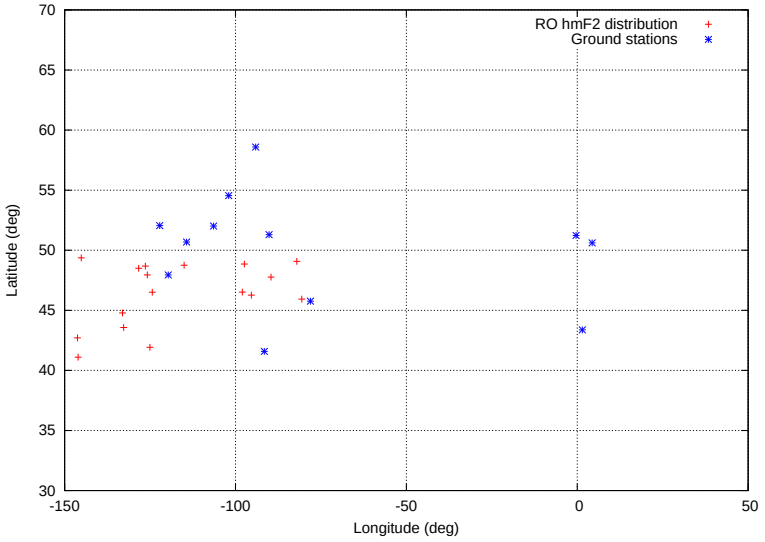

Figure 7.17: *Zoom of the upper distribution of RO hmF2 for January 7, 2007 and ground stations used for geodesic processing.*

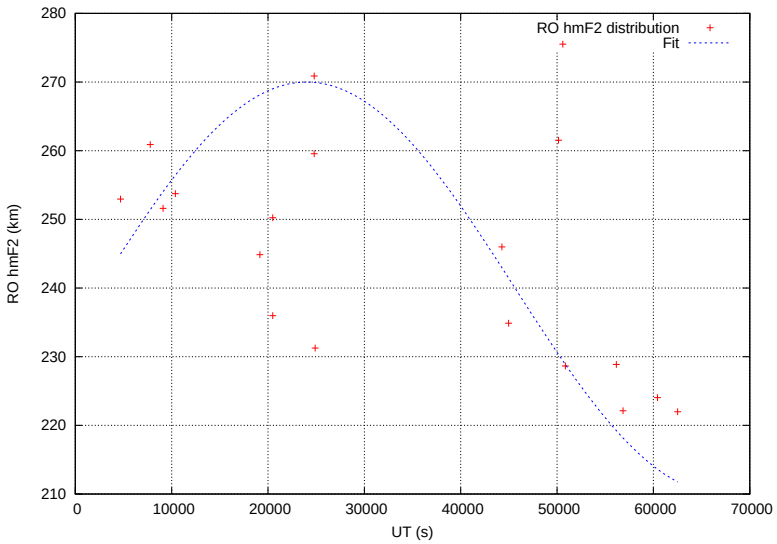

Figure 7.18: *Distribution of RO hmF2 for January 7, 2007 versus UT and curve fitting of hmF2 vesus UT in such region.*

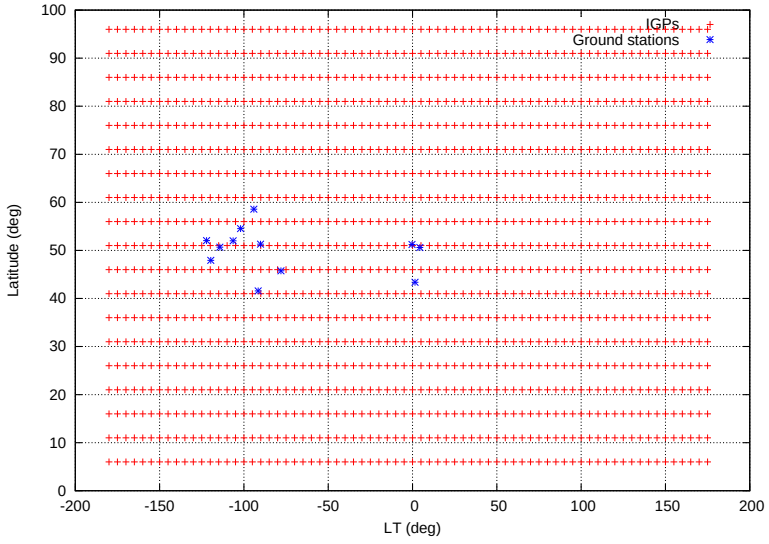

Figure 7.19: *Distribution of IGPs in local time and latitude (sun-fixed frame). A snapshot of the ground station distribution is also depicted.*

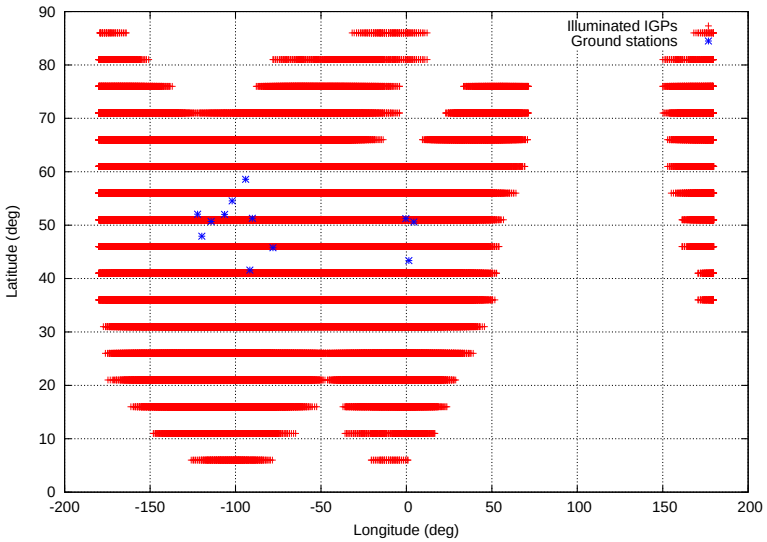

Figure 7.20: *Distribution of illuminated IGPs in longitude and latitude (Earth-fixed frame). The involved ground stations are also depicted.*

Analysis of tests

When performing **Test A**, DCBs should provide a constant value since it should be DCB_j. Therefore, we should expect from real data some noise with a σ. The smaller the σ, the better determination of DCB_j. This is exactly what we can see in Figure 7.21 for simulated data: It depicts the standard deviation of observed STEC subtracted from modeled STEC with respect the PRN number for several effective heights (250, 350, 450 and 550 km). The better performance is, as expected from the results in previous section, for a fixed effective height at 350 km. Therefore, from Figure 7.22, we should be expecting a better performance for 350 km. Nevertheless, the results with real data do not discriminate results as in Figure 7.21. Figure 7.22 seems to indicate 250 km having the best performance followed by the variable height.

When performing **Test B**, $LI_i^j - \alpha \cdot STEC - DCB^j$ becomes what is called a post fit residual. Figure 7.23 depicts the post fit residuals with respect PRN number for several choices of effective heights (250, 350, 450 and 550 km). As expected from simulated data, the best performance is for a fixed effective height at 350 km. Nevertheless, when using real data, Figure 7.24 shows that, again, againts all odds, no effective heights seem to perform significantly better or, at least, it is not clear that the best performance is for an effective height of 350 km.

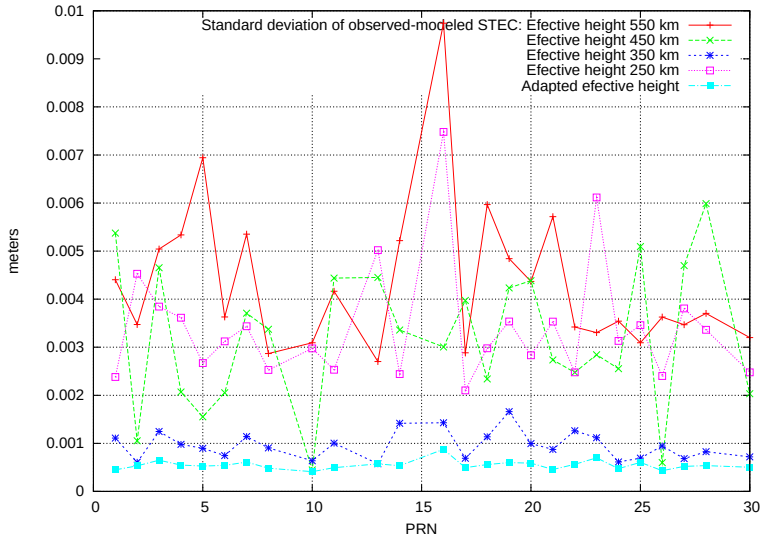

Figure 7.21: *Test A. **Simulated data**. Standard deviation of (observed STEC - modeled STEC) with respect PRN number for several effective heights: 250, 350, 450 and 550 km.*

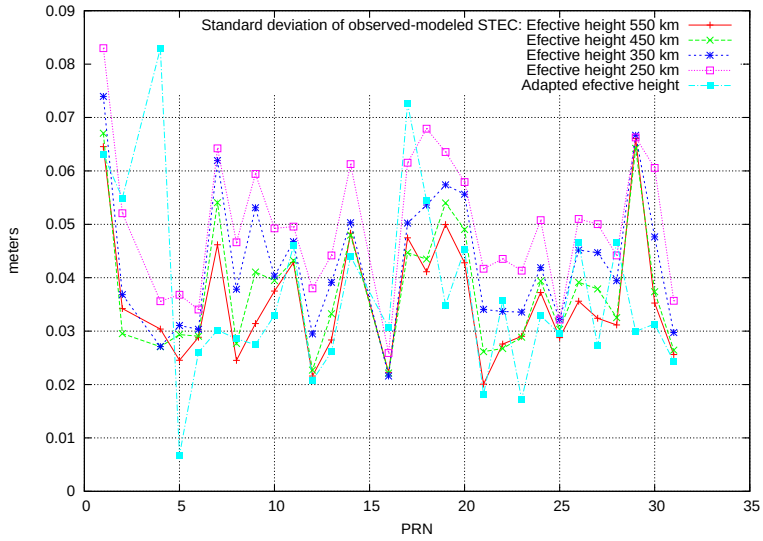

Figure 7.22: *Test A. **Real data**. Standard deviation of (observed STEC - modeled STEC) with respect PRN number for several effective heights: 250, 350, 450 and 550 km.*

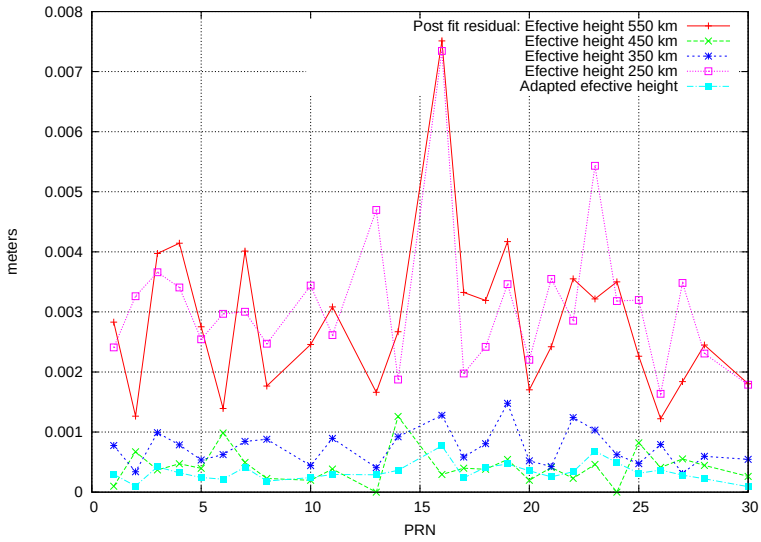

Figure 7.23: *Test B.* ***Simulated data****. Post fit residiuals with respect PRN number for several effective heights: 250, 350, 450 and 550 km.*

When performing **Test C**, the use of single differences of LI_i^j minus modeled $\alpha \cdot STEC$ between different receiver stations and the same satellite should give a constant value (actually, this constant value should correspond to the difference of DCBs for the two stations involved in the single differencing). We have used BREW station as reference to perform the single differences. Figure 7.25 shows the evolution of the single differences with respect time for several choices of effective heights (250, 350, 450 and 550 km) where the best performance, as expected for simulated data, is for a fixed effective height at 350 k. In Figure 7.26, it is not so clear to determine whether there is a much better performance than the others.

Therefore, there are some inconsistencies with the expected results from simulated data when applied to real data. From Figure 7.27, we would be expecting some value for h_{eff} around 500 km (since it is around such value that the minimum rms is found for the post-fits residuals, hence the best choice). Nevertheless, while looking at Figure 7.28, the value for $hmF2$ for that region would correspond to a value belonging to the interval 220 to 270 km, and by means of the realtionship between $hmF2$ and h_{eff} found in the previous chapter, the corresponding expected h_{eff} would be around 300km.

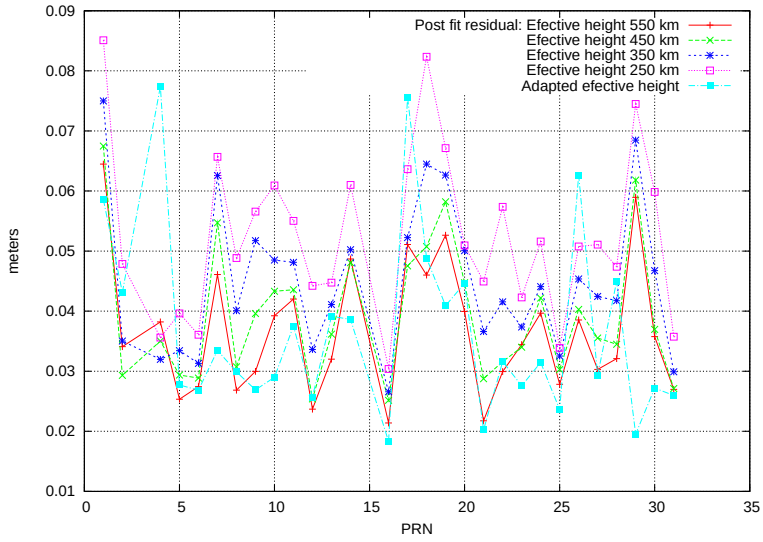

Figure 7.24: *Test B.* ***Real data****. Post fit residuals with respect PRN number for several effective heights: 250, 350, 450 and 550 km.*

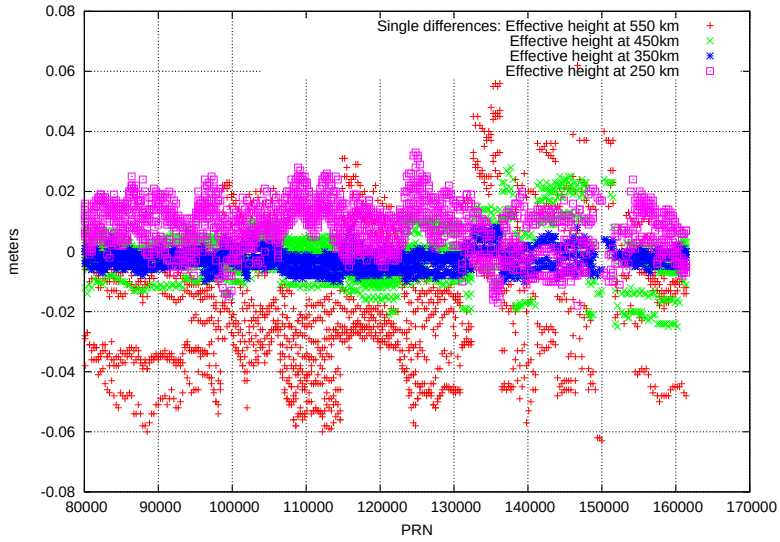

Figure 7.25: *Test C.* ***Simulated data****. Evolution of the single differences of LI_i^j minus modeled $\alpha \cdot STEC$ between different receiver stations and the same satellite with respect time for several choices of effective heights: 250, 350, 450 and 550 km.*

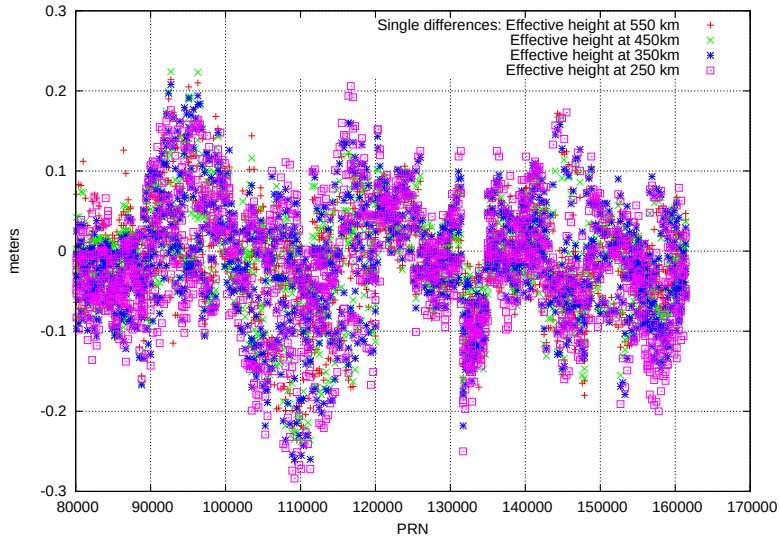

Figure 7.26: *Test C.* ***Real data****. Evolution of the single differences of* LI_i^j *minus modeled* $\alpha \cdot STEC$ *between different receiver stations and the same satellite with respect time for several choices of effective heights: 250, 350, 450 and 550 km.*

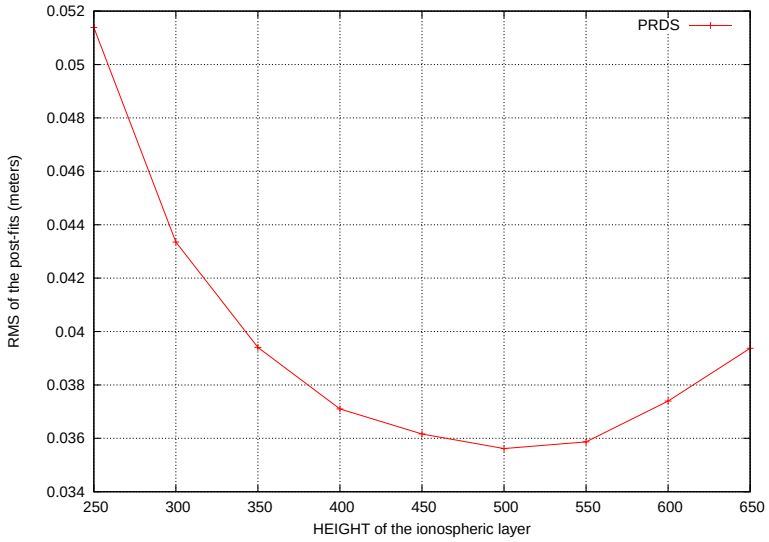

Figure 7.27: *RMS of the post-fits expressed in meters for PRDS IGS station with respect the height of the ionospheric layer.*

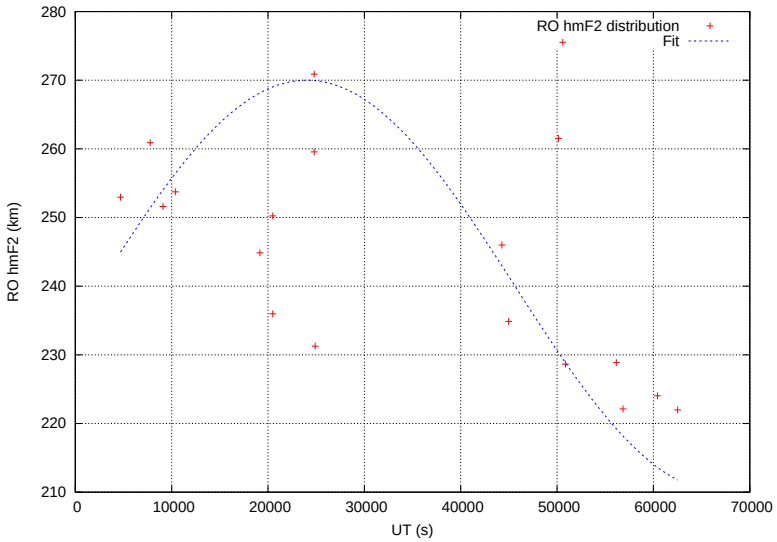

Figure 7.28: *Zoom of the upper distribution of RO hmF2 for January 7, 2007 and ground stations used for geodesic processing.*

7.9 Protonosphere: the key point

The answer to the inconsistencies in previous results lays in the fact that we have not considered the contribution of the protonosphere. As already indicated in Section 7.3 with Eq. 7.8, there are two main contributions to the total electron density $N_e(h)$, $N_{O^+}(h)$ and $N_{H^+}(h)$. One way to understand their influence in the total electron profile is to analytical approximate each of these contributions as an Epstein function:

$$N(h) = N_j(hm)sech^2(\frac{h-hm}{2H_j}) \tag{7.20}$$

Note that this kind of expression becomes an exponential $A \cdot e^{\frac{h-hm}{H_j}}$ when $H_j >> h - hm$ justifying the choice of exponential extrapolation for the shape profiles as described in Chapter 6.
Therefore, we can now express $N_e(h)$ as:

$$N_e(h) = N_{O^+}(hm)sech^2(\frac{h-hm}{2H_{O^+}}) + N_{H^+}(hm)sech^2(\frac{h-hm}{2H_{H^+}}) \tag{7.21}$$

Using the plasma scale height definition:

$$H_j = \frac{kT_j}{m_j g} \tag{7.22}$$

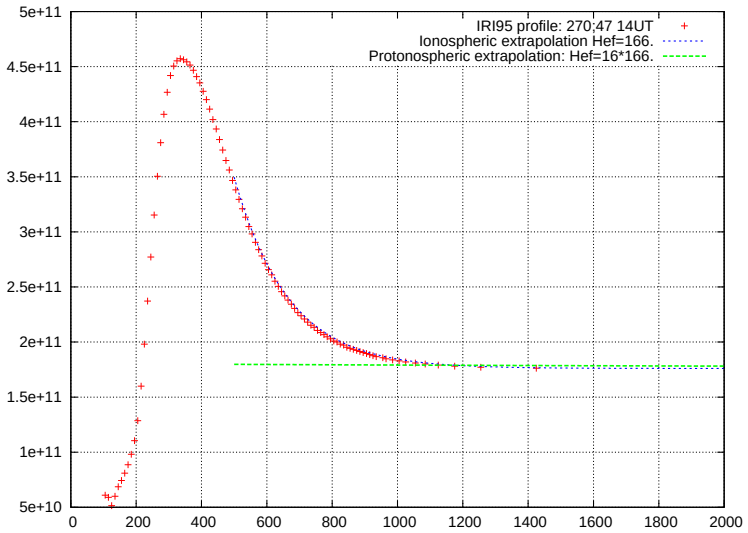

Figure 7.29: *Density profiles from IRI versus extrapolated profile with derived corresponding h_{eff}. The contribution of an effective hight sixteen times bigger is also depicted (emulating the contrubution of the protonosphere).*

we can now rewrite Eq. 7.23 in terms of only one of the constituents ions:

$$N_e(h) = N_{O^+}(hm)sech^2(\frac{h-hm}{2H_{O^+}}) + N_{H^+}(hm)sech^2(\frac{h-hm}{32H_{O^+}}) \qquad (7.23)$$

From here, we can deduce that due to the fact that the 0^+ ion is sixteen times heavier that the H^+ ion, their respective **scale heights** also follow that relationship (see Figure 7.29 and Figure 7.30). Since N_{O^+} is the fraction that we can derive from RO data (from around 700 km height and below), the fraction provided by N_{H^+}, while being smaller, it extends to extremely high heights becoming of crucial importance to account for the remaining TEC above the LEO orbit and when trying to deduce effective heights. Note that even in the case the protonosphere would only contribute to a 10% of the total, since its effective height would be of about 2000 km with respect a 90% contribution of the ionosphere with an effective height of 300 km, it would mean that:

$$300 \cdot 90\% + 2000 \cdot 10\% = 479km \qquad (7.24)$$

the associated effective height would be around 480 km, higher than the one derived from RO only data. The recommendation to consider in N_e with its constituent ions (see Eq. 7.23) is supported by the following conclusive

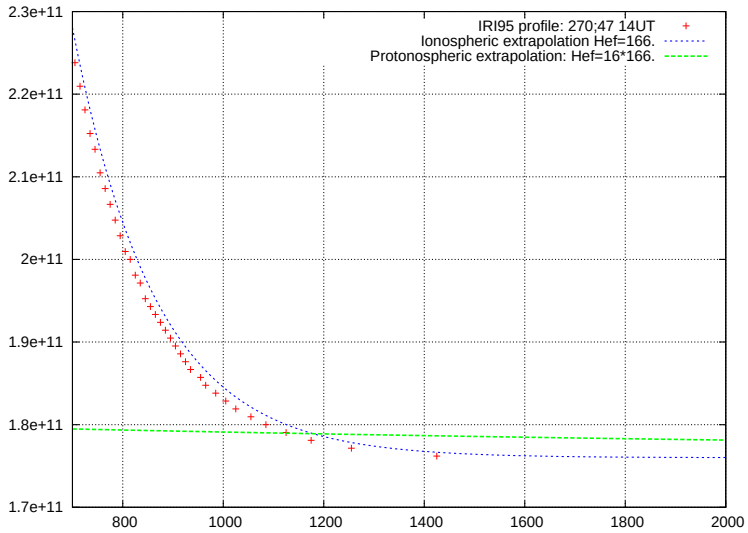

Figure 7.30: *Density profiles from IRI: detail of the higher part of curves in Figure 7.29.*

plots. In Figure 7.31, a two-layer model has been considered, the first layer to account for the ionosphere with a variable height following Eq. 7.28, and another layer to account for the protonospheric contribution with an effective height of about 2000 km (approximately, sixteen times the effective height of the inosphere) and IGP grid as shown in Figure 7.19. In this figure, the TEC that would correspond to the ionospheric contribution is depicted versus the TEC from the protonospheric contribution. What any LEO satellite "sees" would correspond to the ionosperic part (red). If we now tried and deduce the corresponding effective heights associated to Figure 7.31, we would obtain results shown in Figure 7.32. The conclusion from Figure 7.32 is that the effective height (Eq. 7.3 and 7.4) cannot be deduced only from RO data. The values derived from there would only correspond to the lowest layers of the atmosphere (green) in Figure 7.32. Moreover, the variation in effective heights is intimately related with the ratio between ionospheric TEC and protonospheric TEC rather their absolute values, which in the case of the ionosphere (green in Figure 7.32) is very small.

In Figure 7.33, it can be stated that the mean difference between the associated effective heights to elevations of 10^0 and 80^0 is around 200 km. This implies that it is not a very good approach to try and solve the mapping function issue with one constant value of effective height suitable for all elevations. The more reasonable approach would be to use two effective heights: one for the ionospheric contribution and another one for the protonospheric

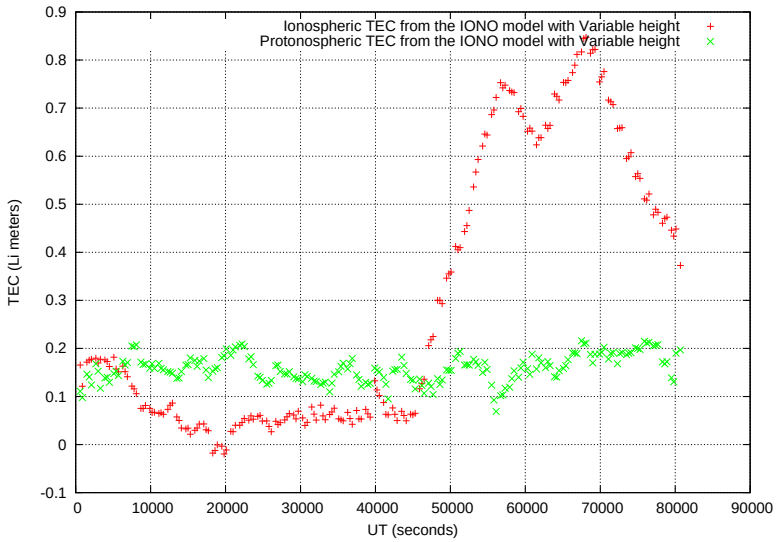

Figure 7.31: *Protonospheric and ionospheric TEC from the IONO model with variable effective height.*

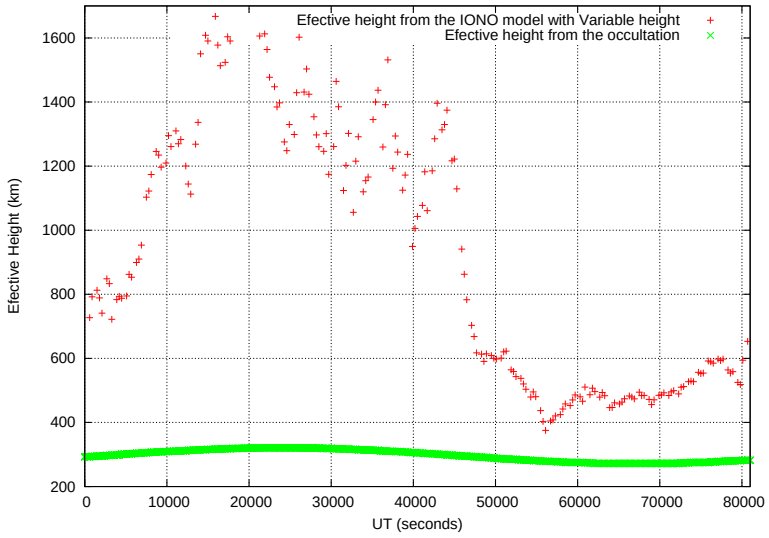

Figure 7.32: *Effective height from IONO model using an effective variable height versus RO-derived effective height.*

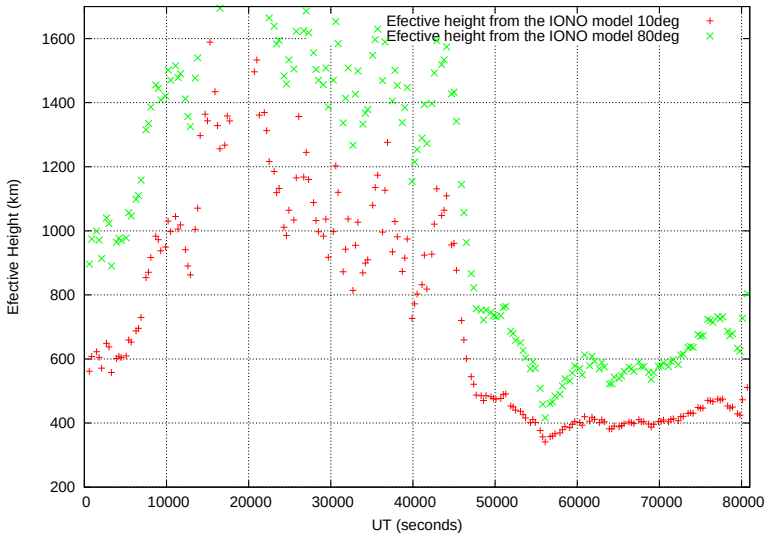

Figure 7.33: *Effective height versus local time for two given elevations:* 10^o *and* 80^0 *deg.*

contribution (in line with the proposal in Eq. 7.25).

7.10 Conclusions and recommendations

The main conclusion from this chapter is that working solely with RO derived data, we are sistematically neglecting the contribution of the protonosphere to the total electron content. With the proposed mapping function based on the analysis of effective heights derived from RO we are only accounting for the ionospheric contribution. The ideal solution for ground-based GNSS data applications would be to use a model with two layers, one for the ionosphere and another one for the protonosphere:

$$STEC = \int_{Ion} N_{O^+} dl + \int_{Prot} N_{H^+} dl = M(H_{eff}) \cdot TEC_{Ion} + M(H_{Prot}) \cdot TEC_{Prot} \tag{7.25}$$

or, if we are looking for high tomographic resolution, to combine RO and topside LEO observations with ground data, as it was done in [Hernández-Pajares et *al.* (1998)]. The information in the following plots have been derived using a one-layer and a two-layer model as suggested in previous section to account for the protonosphere (one layer to account for the ionosphere with a variable height following Eq. 7.28, and another layer to account for the protonosphere with an effective height of about 2000 km and IGP grid 5^ox5^o).

In Figure 7.34, there is an example of VTEC calculation for ground station BREW versus local time. There are significant differences when using a two-layer model.

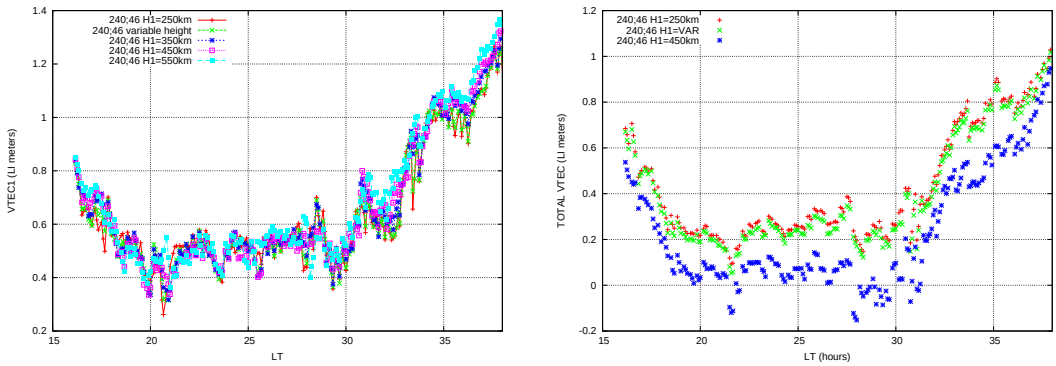

Figure 7.34: *Ionosphere for ground station BREW: VTEC expressed in LI meters versus local time: left, one-layer model, right two-layer model.*

In Figure 7.35, one can see RMS of the post-fits (Test B) expressed in meters for ground station NLIB versus local time: on the right, the RMS values are dramatically reduced. In Figure 7.36, with the one-layer model

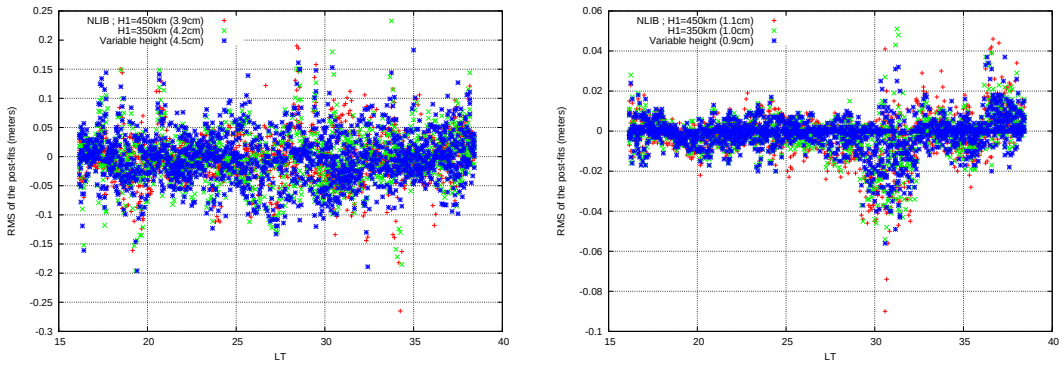

Figure 7.35: *RMS of the post-fits expressed in meters for NLIB versus local time: left, one-layer model, right two-layer model.*

one would conclude that the effective heights lay around 500 km (compatible with expression 7.24) while with the two-layer models these values are around 300 km for the N_{0^+} layer, as derived from RO (see Figure 7.28). In Figure 7.37, the sigma of the single differences (Test C) versus time is dramatically

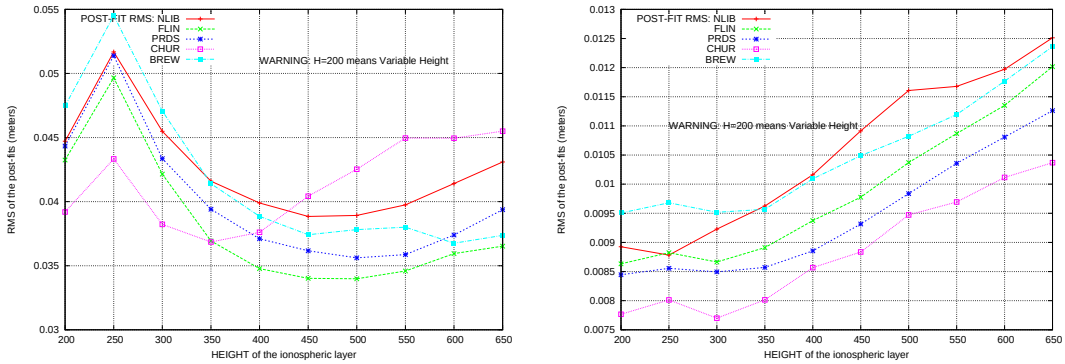

Figure 7.36: *RMS of the post-fits expressed in meters for several stations with respect the height of the ionospheric layer: left, one-layer model, right two-layer model.*

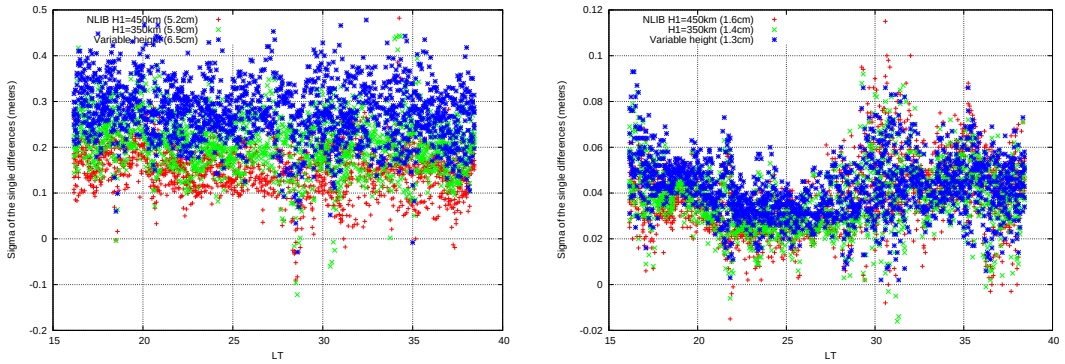

Figure 7.37: *Sigma of the single differences of LI_i^j minus modeled $\alpha \cdot STEC$ between different receiver stations and the same satellite expresssed in meters for NLIB with respect local time: left, one-layer model, right two-layer model.*

reduced for the two-layer model. Note in Figure 7.38, the reduction in sigma values when the two-layer model (right) is used with respect one single-layer model (left). Moreover, in Figure 7.38, the lower sigma (Test C) for the one-layer model corresponds to $hmF2$ around 500 km whereas for the two-layer model, around 300 km.

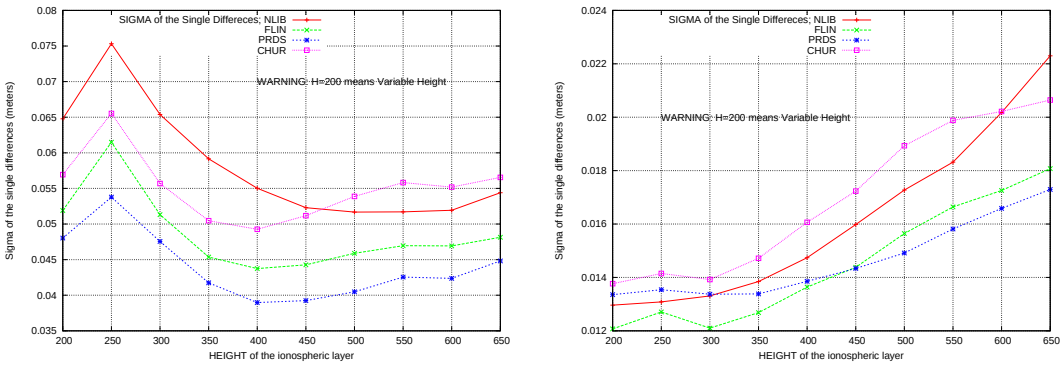

Figure 7.38: *Sigma of the single differences of LI_i^j minus modeled $\alpha \cdot STEC$ between different receiver stations and the same satellite for several stations versus the height of the ionospheric layer: left, one-layer model, right two-layer model.*

Conclusions

Maldigo la poesía concebida como un lujo cultural por los neutrales
que, lavándose las manos, se desentienden y evaden.
Maldigo la poesía de quien no toma partido hasta mancharse.
Cantos íberos- Gabriel Celaya

In this work, the feasibility of the separability implementation to bending angles as main input observable has been shown, completing previous works where separability was implemented for the ionospheric combination observable LI in a very straightforward way, which is not possible when using bending angles. In order to apply separability to the bending angle, a set of approximations have been done allowing to express the bending angle in terms of the change of the refractive index. A novel approach different from double-differencing has been explored. The selected strategy has been to use the fact that the Doppler shift, which causes the ray bending due to rafractivity gradients (hence the bending angle), can be deduced to be proportional to the electron density gradient (see deduction below) under some assumptions.

Clock drift mitigation when working with excess phase in RO scenarios

In order to mitigate clock drifts, it has been proven the equivalence of using the excess phase of the ionospheric free combination (Lc observable) as to double differencing or space-based single differencing with solved clocks at ionospheric heights. Hence, the clock calibration method of this work will be valid for ionospheric radio occultation processing but, for tropospheric retrievals, double differencing will be required. Under this approach, no extra GPS transmitters or LEO receivers but the ones involved in the radio occultation event are required to calibrate the clocks. Consequently, more occultations can be inverted with less data processing and computational

load.In this way, indirectly, it has been confirmed that the ray path difference between L_1 and L_2 is not significative, validating the method with LI used in previous works.

Implementation of the *separability* concept with bending angles as main input

The implementation of separability to bending angles provides an inverting method that could allow its extension to neutral atmosphere, extension that is not feasible when working with occultation data derived from the LI observable (because the tropospheric signature cancels out when forming $LI = L1 - L2$). Several intercomparisons with reference has been carried out to confirm results. Regarding height comparisons, the results for $hmF2$ confirm expected results in previous works which are compatible with the reference error. The global performance confirm the improvement of the separability implementation in Abel inversion (45%) by using the bending angle observable. The equivalence of results obtained with bending angle and LI implementing separability has been shown in terms of $foF2$ and foE frequencies and $hmF2$ heights. This implementation opens the possibility for its extension to troposphere whis is one of the further researchs that could be conducted as a follow up of this thesis.

Upper Ionosphere estimation

Several approaches to account for the upper ionospheric contribution have been tackled, apart from the fact of neglecting such contribution: a climatological model, an exponential extrapolation and condisering the nature of the separability concept. The two former approaches provide a slight improvement in profile determinations that has been tested with high quality reference data (manually calibrated DPS measurements). The latter has suggested some implications that there was some problem underlying the hypothesis of separability and has open a new research line withing the thesis work delt with in the final chapter.

Analysis of mapping functions derived from RO data

In Chapter 7, it has been proposed a way to obtain mapping functions derived from RO profiles. Such mapping functions can be easily derived from usual ionospheric parameters, such as $hmF2$ and the slab thickness τ. For the contribution of this part of the ionosphere, it has been shown that it is capable to account for the total electron content (TEC). However, by working solely with RO derived data, we are systematically neglecting the contribution of the protonosphere to the total electron content. With the initial proposed mapping function based on the analysis of effective heights derived from RO, only the ionospheric contribution is accounted for. The ideal solution for ground-based GNSS data applications would be to use a two-layer model, one to model the ionosphere and another one for the protonosphere, or alternatively, if we are looking for high tomographic resolution, to combine RO and topside LEO observations with ground data. It has been shown that by modelling in such way, the results that were obtained with RO data analysis can be validated. The most important conclusion is that the ratio between ionospheric and protonospheric contribution is the driver for the location of the effective heights.

Bibliography

[Anthes et *al.* (2008)] Anthes R.A., Bernhardt P.A., Chen Y., Cucurull L., Dymond K.F., Ector D., Healy S.B., Ho S.P., Hunt D.C., Kuo Y.H., Liu H., Manning H., McCormick C., Meehan T.K., Randel W.J., Rocken C., Schreiner W.S., Sokolovskiy S.V., Syndergard S., Thompson D.C., Trenberth K.E., Wee T.K., Yen N.L., Seng Z. (2008) The COSMIC/FORMOSAT-3 mission: Early Results, Bull. Amer. Met. Soc. 89, pp. 313-333, doi: 10.1175/BAMS-89-3-313

[Aragon-Angel (2008)] Aragon-Angel, M.A. (2008) New Technique to Improve the Electron Density Retrieval Accuracy: Application to FORMOSAT-3/COSMIC Constellation, ION GNSS 2008, 16th-19th September 2008, Savannah (Georgia), USA

[Aragon-Angel et *al.* (2009)] Aragon-Angel, A., M., Hernández-Pajares, M., Juan, M., Sanz, J. (2009) Obtaining more accurate electron density profiles from bending angle with GPS occultation data: FORMOSAT-3/COSMIC constellation, Advances in Space Research, Vol. 43, Issue 11(2), pp. 1694-1701, doi:10.1016/j.asr.2008.10.034

[Aragon-Angel et *al.* (2009)] Aragon-Angel, A., M. Hernández-Pajares, J.M. Juan, J. Sanz (2009) Improving the Abel transform inversion using bending angles from FORMOSAT-3/COSMIC, GPS Solutions, Springer Berlin/Heidelberg, ISSN 080-5370 (Print) 1521-1886 (Online), DOI:10.1007/s10291-009-0147-y

[Bilitza et *al.* (1979)] Bilitza, D., N.M. Sheik, R. Eyfrig (1979) A global model for the height of the F2 peak using M(3000) values from the CCIR. Telecomm. J. 46, pp. 549-553

[Blewit (1989)] Blewitt G (1989) Carrier phase ambiguity resolution for the global positioning system applied to geodetic baselines up to 2000 km, J Geophys Res 94(B8): 10187-10203

[Born and Wolf (1980)] Born M., Wolf E. (1980) Principles of optics, Pergamon Press

[Bracewell (2000)] Bracewell, R.N. (2000) The Fourier Transform and its Applications, 3rd ed. Boston, McGraw-Hill

[Bradley and Dudeney (1973)] Bradley P.A., J.R. Dudeney (1973) A simple model of the vertical distribution of electron concentration in the ionosphere, J. Atmos. Terr. Phys., 35, pp. 2131-2146

[Breed and Goodwin (1997)] Breed A.M., Goodwin, G.L. (1997) Ionospheric slab thickness and total electron content determined in Australia, Radio Science 32 4, pp. 1635-1643

[Brekke (1997)] Brekke, A. (1997) Physics of the upper polar atmosphere, Wiley-Praxis Series in Atmospheric Physics, John Wiley & Sons

[Brunini et *al.* (2004)] Brunini, C., Meza, A., Azpilicueta, F., Van Zele, A., Gende, M., Diaz, A. (2004) A new ionosphere monitoring technology based on GPS, Astrophysics and Space Science 290, pp. 415-429

[Coco et *al.* (1991)] Coco, D.S., Coker, C., Dahlke, S.R., Clynch, J.R. (1991) Variability of GPS satellite differential group delays biases, IEEE Transactions on Aerospace and Electronic Systems 27, pp. 931-938

[Comité Consultatif International des Radiocommunications (1967)] Comité Consultatif International des Radiocommunications (1967) CCIR Atlas of Ionospheric Characteristics, Report 340-4, International Telecommunications Union, Geneva

[Cueto et *al.* (2004)] Cueto M., Coisson P., Radicella S.M., Ciraolo L., Herraiz M. (2004) Including the Gallagher plasmaspheric model in the NeQuick ionospheric model, Geophysical Research, vol.6, 00244

[Davies (1990)] Davies K. (1990) Ionospheric Radio, Chapter 5, IEE Electromagnetic Waves Series, Vol. 31, Peter Peregrinus Ltd

[Dudeney (1983)] Dudeney J.R. (1983) The accuracy of simple methods for determining the height of the maximum electron concentration of the F2-layer from scaled ionospheric characteristics, J. Atmos. Terr. Phys. (45), pp. 629-640

[Fjeldbo et *al.* (1971)] Fjeldbo, G., Kliore, A., Eshelman, V. (1971) The neutral atmosphere of venus as studied with the mariner v radio occultation experiments. Astron. J. 76, pp. 123-140

[García-Fernández (2004)] García Fernández M. (2004) Contributions to the 3D ionospheric sounding with GPS data, UPC, B.45104-2004/84-688-8156-2

[Garcia-Fernández et *al.* (2003)] Garcia-Fernández, M., Hernández-Pajares, M., Juan, M., Sanz, J. (2003) Improvement of ionospheric electron

density estimation with GPSMET occultations using Abel inversion and VTEC information, Journal of Geophysical Research, Vol. 108, No. A9, 1338, doi:10.1029/2003JA009952

[Hajj and Romans (1998)] Hajj, G.A., Romans, L.J. (1998) Ionospheric electron density profiles obtained with the Global Positioning System: Results from the GPS/MET experiment, Radio Science, volume 33, number 1, pp. 175-190

[Hajj et *al.* (2004)] Hajj G.A., Ao C.O., Iijima B.A., Kuang D., Kursinski E.R., Mannucci A.J., Meehan T.K., Romans L.J., de la Torre Juarez M., Yunck T.P. (2004) CHAMP and SAC-C Atmospheric Occultation Results and Intercomparisons, J Geophys Res 109(D6) ,Â ISSNÂ 0148-0227, pp.Â D06109.1-D06109.24

[Hernández-Pajares et *al.* (2006)] Hernández-Pajares, M., Juan J.M., Sanz J. (2006) Real time MSTIDs modelling and application to improve the precise GPS and GALILEO navigation, Proceedings of the Institute of Navigation, pp. 1358-1368, Fort Worth, Texas

[Hernández-Pajares et *al.* (2000a)] Hernández-Pajares, M., Juan J.M., Sanz J. (2000) Improving the Abel inversion by adding ground data LEO radio occultations in the ionospheric sounding, Geophysical Research Letters, Vol. 27, 2743-2746

[Hernández-Pajares et *al.* (1999)] Hernández-Pajares M., Juan, J.M., and J. Sanz (1999) New Approaches in Global Ionospheric Determination Using Ground GPS Data, Journal of Atmospheric and Solar-Terrestrial Physics, Vol 61, 1237-1247

[Hernández-Pajares et *al.* (1998)] Hernández-Pajares, M., Juan, J.M., Sanz,J., Sole J.G. (1998) Global observation of the ionospheric electronic response to solar events using ground and LEO GPS data, Journal of Geophysical Research-Space Physics, Vol.61, pp.1237-1247

[Hernández-Pajares et *al.* (2002)] Hernández-Pajares, M., Juan J.M. , Sanz J., Colombo O.L. (2002) Improving the real-time ionospheric determination from GPS sites at Very Long Distances over the Equator, Journal of Geophysical Research, V107, p1296-1305

[Hernández-Pajares et *al.* (2001)] Hernández-Pajares, M., Juan, J.M., Sanz,J., O.L. Colombo (2001) Tomographic modeling of GNSS ionospheric corrections: Assessment and real-time applications, ION GPS 2001, Salt Lake, USA

[Hernández-Pajares et *al.* (2000b)] Hernández-Pajares, M., Juan, J.M., Sanz,J., O.L. Colombo (2000) Application of ionospheric tomography

to real-time GPS carrier-phase ambiguities resolution, at scales of 400-1000 Km and with high geomagnetic activity, Geophysical Research Letters, Vol. 27, No. 13, pp. 2009-2012

[Hernández-Pajares et *al.* (2005)] Hernández-Pajares, M., J. M. Juan, J. Sanz, M. García-Fernandez (2005) Towards a more realistic ionospheric mapping function, XXVIII URSI General Assembly, Delhi

[Ho et *al.* (1995)] Ho, C.M., Wilson, B.D., Mannucci, A.J., Lindqwister, U.J., Yuan, D.N. (1995) A comparative study of ionospheric total electron content measurements using global ionospheric maps of GPS, TOPEX radar, and the Bent model, Radio Science 32, 1499-1512

[Hochegger et *al.* (2000)] Hochegger G., Nava B., Radicella S., Leitinger R. (2000) A family of Ionospheric Models for Different Uses, Phys. Chem. Earth 25(4), pp. 307-310

[Hoffmann-Wellenhof et *al.* (2004)] Hoffmann-Wellenhof, B., H. Lichtenegger, J. Collins (2004) GPS: Theory and Practice (Fourth Edition), Springer-Verlag, Wien, New York

[IERS (2008)] International Earth Rotation and Reference Systems Service (2008) Central Bureau, IERS Annual Report 2006, Edited by Wolfgang R. Dick and Bernd Richter, Frankfurt am Main: Verlag des Bundesamts für Kartographie und Geodäsie, in print

[ITU-R (2000)] NeQuick Software for ITU-R rec. pp. 371-8, available at the website hhtp://www.itu.int/ITU-R/software/study-groups/rsg3/databanks/ionosph/Rec531/

[Jones and Gallet (1965)] Jones, W. B., R. M. Gallet (1965) The Representation of Diurnal and Geographic Variations of Ionospheric Data by Numerical Methods, Telecomm. J. 29, 129, 1962, and 32, 18

[Kliore et *al.* (1964)] Kliore, A., Hamilton, T., Cain, D. (1964) Determination of Some Physical Properties of the Atmosphere of Mars from Changes in the Doppler Signal of a Spacecraft on an Earth Occultation Trajectory, Technical Report 32-674, Jet Propulsion Laboratory, Pasadena, California

[Klobuchar et *al.* (1993)] Klobuchar, J. A., Basu, S., Doherty, P. (1993) Potential limitations in making absolute ionospheric measurements using ciual frec]uency radio waves from GPS satellites, Proceedings of the Seventh International Ionospheric Effects Symposium, J. Goodman, cd., Alexandria, VA

[Komjathy and Hernández-Pajares (2004)] Komjathy, A., M. Hernández-Pajares (2004) The IGS Global TEC maps: Present and Future, National Radio Science Meeting, Boulder, CO, USA

[Lanyi and Roth (1988)] Lanyi, G.E., Roth, T. (1988) A comparison of mapped and measured total ionospheric electron content using Global Positioning System and beacon satellite observations. Radio Science 23 (4), pp. 483-492

[Lei et *al.* (2007)] Lei J, Syndergaard S, Burns AG, Solomon SC, Wang W, Zeng Z, Roble RG, Wu Q, Kuo YH, Holt JM, Zhang SR, Hysell DL, Rodrigues FS, Lin CH (2007) Comparison of COSMIC ionospheric measurements with ground-based observations and model predictions: preliminary results, J Geophys Res 112, A07308, doi: 10.1029/2006JA012240

[Leick (1994)] Leick A. (1994) GPS satellite surveying, Ed. Wiley-Interscience Publication

[Liu et *al.* (1978)] Liu A.S. (1978) On the Determination and Investigation of the Terrestrial Ionospheric Refractive Indices Using GEOS-3/ATS-6 Satellite-to-Satellite Tracking Data; Final Report, NASA-CR-156848, November 1

[Marin et *al.* (2001)] Marin, D., Mikhailov, A. V., Morena, B. A., Herraiz, M. (2001) Long-term hmF2 trends in the Eurasian longitudinal sector from the ground-based ionosonde observations, Ann. Geophys., 19, 761-772

[McNamara et *al.* (1987)] McNamara, L.F., B.W. Reinisch, J.S. Tang (1987) Values of hmF2 deduced from automatically scaled ionograms. Adv. Space Res. 7 6, pp. 53-56

[Melbourne (2004)] Melbourne W.G. (2004) Radio Occultations Using Earth Satellites: A Wave Theory Treatment, Jet Propulsion Laboratory, California Institute of Technology

[Ogaja and Satirapod (2007)] Ogaja, C., Satirapod, C. (2007) Analysis of high-frequency multipath in 1-Hz GPS kinematic solutions, GPS Solutions, Springer-Verlag

[Parkinson and Spilker (1996)] Parkinson, B.W., Spilker Jr., J.J. (1996) Global Positioning System: Theory and applications. Volumes I & II, American Institute for Aeronautics and Astronautics Inc.

[Orus et *al.* (2002)] Orus R., M. Hernandez-Pajares, J.M. Juan, J. Sanz, M. Garcia-Fernandez (2002) Performance of different TEC models to pro-

vide GPS ionospheric corrections, Journal of Atmospheric and Solar-Terrestrial Physics, Vol. 64, pp. 2055-2062

[Orus et *al.* (2003)] Orus R., M. Hernandez-Pajares, J.M. Juan, J. Sanz, M. Garcia Fernandez (2003) Validation of the GPS TEC maps with topex data, Adv. Space Res. 31 (3), pp. 621-627

[Parkinson and Spilker (1996)] Parkinson, B.W., Spilker Jr., J.J. (1996) Global Positioning System: Theory and Applications, Volume I, pp. 485-496

[Pavelyev et *al.* (1997)] Pavelyev A., Zakharov A., Kucherjavenkov A., Molotov E., Siderenko I., Kucherjavenkova I., Pavelyev D. (1997) Propagation of Radio Waves Reflected from Earth's Surface at Grazing Angles between a Low-Orbit Space Station and a Geostationary Satellite, Journal of Communications Technology and Electronics, vol. 42, no. 1, pp. 51-57

[Piggot and Rawer (1978)] Piggot, W., Rawer, K. (1978) URSI Handbook of ionogram intereation and reduction, World Data Center A for Solar-Terrestrial Physics

[Radicella and Leitinger (2001)] Radicella, S.M., Leitinger, R. (2001) The evolution of the DGR approach to model electron density profiles, Adv. Space Res., Vol. 27, Issue 1, pp. 35-40

[Rawer (1994)] Rawer K. (1994) Problems arising in empirical modeling of the terrestrial ionosphere, Adv. Space Res. 14 (12), pp. 7-16

[Rishbeth et *al.* (2000)] Rishbeth H., K.J.F. Sedgemore-Schulthess, Th. Ulich (2000) Annual and semiannual variations in the height of the ionospheric F2-layer, Annales Geophysicae, 18 (3), pp. 285-299

[Rocken et *al.* (2000)] Rocken, C., Kuo, Y.H., Schreiner, W., Hunt, D., Sokolovsky, S. (2000) COSMIC System Description, Special issue of Terrestrial, Atmospheric and Oceanic Science, 11(1), pp. 21-52

[Schaer et *al.* (1998)] Schaer, S., W. Gurtner, J. Feltens (1998) IONEX: The IONosphere Map EXchange. Format Version 1, Proceedings of the IGS AC Workshop

[Seeber (1992)] Seeber, G. (1992) Satellite Geodesy, Walter de Gruyter, Inc.

[Shimazaki (1955)] Shimazaki T. (1955) World daily variability in the height of the maximum electron density of the ionospheric F2-layer, J. Radio Res. Lab. (Japan), 2, pp. 85-97

[Schreiner et *al.* (1999)] Schreiner, W.S., Sokolovskiy, S.V., Rocken, C. (1999) Analysis and validation of GPS/MET radio occultation data in the ionosphere, Radio Science, Volume 34, Number 4, pp. 949-966

[Smith et *al.* (2008)] Smith, D. A., E. A. Araujo-Pradere, C. Minter, T. Fuller-Rowell (2008), A comprehensive evaluation of the errors inherent in the use of a two-dimensional shell for modeling the ionosphere, Radio Sci., 43, RS6008, doi:10.1029/2007RS003769

[Syndergaard (1999)] Syndergaard, S. (1999) Retrieval analysis and methodologies in atmospheric limb sounding using the GNSS radio occultation technique, Danish Metereological Institute Scientific Report, Danish Meteorolgical Institute, Copenhagen, Denmark, 99/6

[Titheridge (1998)] Titheridge, J. (1998) The real heigth analysis of ionograms: A generalized formulation, Radio Science 23(5), pp. 831-849

[Tricomi (1985)] Tricomi, F.G. (1985) Integral equations, Dover Publ., New York

[Tsai et *al.* (2001)] Tsai, L., Tsai, W., Schreiner, W., Berkey, F., Liu, J. (2001) Comparisons of GPS/MET retrieved ionospheric electron density and ground based ionosonde data, Earth Planets Space 53, pp. 193-205

[Tsedilina and Weitsman (1992)] Tsedilina, Ii. Ii,, Weitsman, O. B. (1992) Influence of the inhomogencous ionosphere on the CJPS determination of satellite and user coordinates, 43rd Ccmgress of the International Astronautical Federation, Washington D.C.

[Wells (1987)] Wells D. (1987) Guide to GPS positioning, Canadian GPS associates, Frederickton

[Wickert et *al.* (2002)] Wickert, J., G. Beyerle, G.A. Hajj, V. Schwieger, Ch. Reigber (2002) GPS radio occultation with CHAMP: Atmospheric profiling utilizing the space-based single difference technique, Geophys. Res. Lett., 29, 8, 10.1029/2001GL013982

[Wickert et *al.* (2001)] Wickert, J., Ch. Reigber, G. Beyerle, R. König, C. Marquardt, T. Schmidt, L. Grunwaldt, R. Galas, T.K. Meehan, W.G. Melbourne, K. Hocke (2001) Atmosphere sounding by GPS radio occultation: First results from CHAMP, Geophys. Res. Lett., 28, pp. 3263-3266

[World Data Center-A (2003)] World Data Center-A (2003) Rutheford Appleton Laboratory, http://www.wdc.rl.ac.uk

[Zhang et *al.* (1999)] Zhang S. R., S. Fukao, W. L. Oliver (1999) Data modeling and assimilation studies with the MU radar, J. Atmos. Solar-Terr. Phys., 61, pp. 563-583

[Yakovlev et *al.* (1996)] Yakovlev O., Matyugov I., Vilkov I.A. (1996) Radio-Wave Phase and Frequency Fluctuations as Observed in Radio Occultation Experiments on the Satellite-to-Satellite Link, Journal of Communications Technology and Electronics, vol. 41, no. 11, pp. 993-998

Appendix A

NeQuick model for Galileo single frequency users

Yo creía que quería ser poeta, pero en el fondo quería ser poema...
Jaime Gil de Biedma

A.1 Optimisation description of the NeQuick model for Galileo

The European Galileo satellite system, currently being built by the European Union (EU) and European Space Agency (ESA), will provide a highly accurate, guaranteed global positioning service under civilian control besides being inter-operable with the pre-existing GPS and GLONASS systems. Galileo signals will also be affected by the atmosphere of the Earth as GPS signals are (see Section 2.3). For a single frequency receiver, the main source of error is the ionosphere. As a first approximation, these effects could be considered to be produced by the free electrons of the ionosphere [Davies (1990)] and more than 99% of this advance/delay could be explained by a term inversely proportional to the squared frequency of the signal. This first approximation allows the correction of such term by using simultaneous measurements in both frequencies ($f1$ and $f2$) computing the ionosphere free combination Lc for precise positioning. But for a GNSS single-frequency receiver, the STEC correction must be provided to users. In this context, there are several models that could be used to take into account this ionospheric term. The chosen model to generate the ionospheric correction coefficients for the Galileo navigation message is the NeQuick model and, the following procedure should be followed (as proposed by AG-IONO expert team).
The first achievement is to optimise the NeQuick model as a function of the effective ionization level (Az) to the observed STEC values at the selected monitor stations. The Az parameter ($F10.7$ corrected including the latitudinal dependence) is the driver for the model optimization to the reference measurements from the ground stations. For every station, all the satellite links are taken into account and the sum of squares of observed minus

computed STEC are calculated:

$$(\Delta STEC)^2 = \sum |STEC_{Observed}(Az) - STEC_{Modeled}(Az)|^2 \qquad (A.1)$$

$STEC_{Observed}$ values from each IGS monitor station to every satellite in view are needed.
The next step is to minimize $(\Delta STEC)^2$ as a function of the Az parameter, to find the optimum Az and thus defining the daily Az value for the station. From Eq. A.1, the expected shape is a parabola with a unique minimum. As a proof of this assumption, Expression A.1 was computed and plotted as a function of the Az parameter for all the IGS. A typical example is shown in Figure A.1.

From the daily Az values for every station, a global daily Az function of

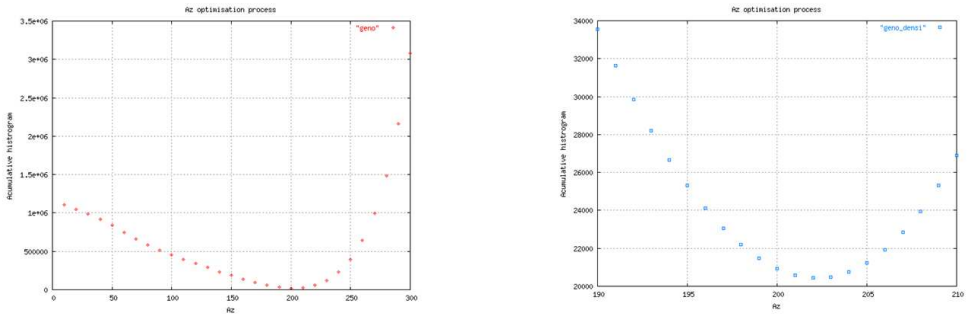

Figure A.1: $(\Delta STEC)^2$ *as a function of the Az parameter for IGS station marker name "geno". Right plot depicts a zoom on the minimum in left plot.*

MODIP is found. This function is a second order polynomial described by three coefficients:

$$A_z = a_0 + a_1 \cdot \mu + a_2 \cdot \mu^2 \qquad (A.2)$$

where:

$$tan\mu = \frac{I}{cos\phi} \qquad (A.3)$$

and μ stands for the modified dip or MODIP, I for the true magnetic dip and ϕ for the geographic latitude. The coefficients a_0, a_1, a_2 are transmitted to the user in the navigation broadcast message.

A.2 Performance analysis of the NeQuick model for Galileo

The performance of the proposed model to correct the ionospheric delay for Galileo single frequency users is going to be analyzed. In order to do so, $STEC_{Observed}$ data are needed. Two different sources are going to be used: STEC values from IFAC-CNR (Istituto di Fisica Applicata "Nello Carrara") and from IGS ÀGIMs provided by UPC. $STEC_{Modeled}$ values along each ray path from receiver to satellite will be calculated using the NeQuick model, as a function of the Az parameter following the descripion in Section A.1. This procedure has been implemented at intervals of 24 hours and at a sampling rate of 20 minutes for IFAC data and 15 minutes for data from GIMs. The results are going to be tested versus the following TEC sources:

- **Comparison with TOPEX**: The aim of this preliminary work is to show the performance of different approaches to the calculation of the Galileo-like ionosphere corrections for a GNSS single-frequency user. The reference consists of the TOPEX/Poseidon data. These data come from an altimetric satellite, at a mean height of about 1330 km. Among other sensors, it has a dual transmitter-receiver in C-band (5.5 GHz) and Ku-band (13.6 GHz), that provide TEC with accuracies, including systematic biases, of about 2-3 TECU [Ho et *al.* (1995)]. For our comparisons, the bias and rms of the models have been computed regarding the TOPEX data as:

$$BIAS = \langle TEC_{TOPEX} - TEC_{Modeled} \rangle \tag{A.4}$$

$$RMS = \sqrt{(\langle TEC_{TOPEX} - TEC_{Modeled} \rangle)^2} \tag{A.5}$$

  where TEC_{TOPEX} is the TOPEX TEC and $TEC_{Modeled}$ is the TEC calculated using the NeQuick model under the selected approach. In order to determine how well a single frequency user can correct the ionospheric delay, the NeQuick model has been compared with the TOPEX data for several approaches.

- **Comparison with differential ionospheric values after fixing phase ambiguities**: It is evident in Eq. A.1 that the $STEC_{Observed}$ used as an input, plays a crucial role in the optimization of the Az parameter, thus in the calculation of the ionospheric corrections for Galileo. The Wide Area Real Time Kinematics (WARTK) technique has been used to test the precision of the STEC used as input by

comparing with differential ionospheric values after fixing phase ambiguities. This technique uses two programs in parallel, a geodetic and an ionospheric one [Hernández-Pajares et *al.* (2001)], in order to fix the phase ambiguities to their integer values in the fixed stations, providing an accurate ionospheric correction to roving users. It uses the fact that the coordinates of the fixed stations are known, then, it is possible to fix the Bc ambiguity (free ionospheric combination ambiguity) to its correct value with a few cm error with the geodetic program. In addition, the ionospheric program runs, in parallel estimating precise ionosphere that allows the computation of a double difference STEC accurate enough. Then mixing both results it is possible to fix the carrier phase ambiguities, and then, to extract a double difference STEC, with a millimeter accuracy. In fact, the differential ionospheric corrections provided by WARTK after fixing ambiguities is less than 0.1 TECU, also for permanent stations separated by thousands of km, including equator, Solar Maximum and high geomagnetic conditions [Hernández-Pajares et *al.* (2002)].

Data set description: The chosen day of study is March 3^{rd}, 2000. The Kp index for this day is smaller than 2 thus the requirement to use only data from an unperturbed geomagnetic period is guaranteed. This is necessary to estimate the validity of the computed model coefficients. Two different IGS monitor station distributions have been selected to perform the comparison: an initial set of 26 available receivers (left side of Figure A.2) mostly distributed in the Northern middle region and a better globally distributed dataset of 25 stations (right side of Figure A.2). This second set of IGS stations has been chosen closest to the potential location for Galileo monitor stations in order to evaluate the NeQuick model as close as possible to the conditions of the Galileo system.

Several approaches have been explored such as different distribution of the monitor stations, different integration heights, an alternative way of deducing the Az values, and different input STEC values in order to study their impact on the results. They are displayed for every approach considering all latitudes and immediately after for latitude 40^o to have a hint of the performance for our geographical situation. There are also depicted plots with a track of the TOPEX/Poseidon satellite versus the calculated values with the studied approach.

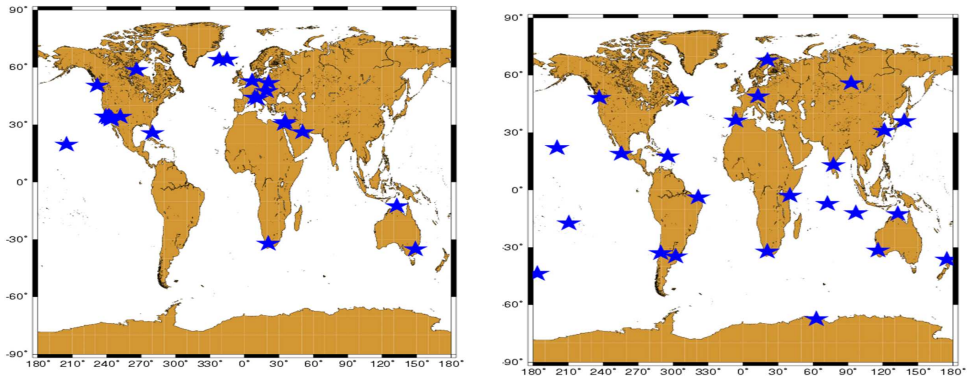

Figure A.2: *Selected distribution of IGS stations.*

Table A.1: *Results for different geographical distributions. The RMS and BIAS are both expressed in TEC units (TECU).*

	RMS	% ERR	BIAS	Obs.	$VTEC_{mean}$
IGS good distribution	16.42	42.9	11.23	51082	38.24
Latitude 40^o	16.44	37.8	13.18	5047	43.54
IGS without chur	17.09	44.7	12.15	51082	38.24
Latitude 40^o	17.31	39.8	14.30	5047	43.54
IGS with chur	18.25	47.7	13.56	51082	38.24
Latitude 40^o	18.73	43.0	16.03	5047	43.54

A.2.1 Results: Influence of the geographical distribution of the monitor stations

The next table shows the results for the two depicted distributions of stations in Figure A.2. On the left distribution, one of the stations (receiver marker name: chur) had not data for the whole day and the global performance is significantly affected by considering or not this station in the calculation. The STEC data used as input are from IGS maps in the three cases.

These results show that the quality of the performance is sensitive to the geographical distribution of input GNSS stations providing input STEC. The criterion for the station location choice should be to avoid uneven geographical distribution of stations.

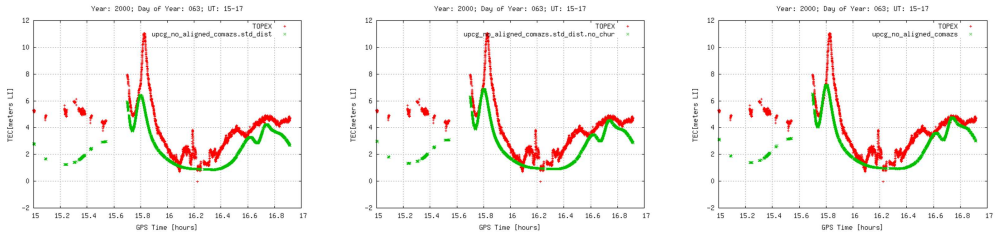

Figure A.3: *On the left-hand plot, even distribution with chur vs. TOPEX data. In the center plot, even distribution without chur vs. TOPEX data. On the right-hand plot, uneven distribution vs. TOPEX data.*

Table A.2: *Results for different ceiling heights. The RMS and BIAS are both expressed in TEC units (TECU).*

	RMS	% ERR	BIAS	Obs.	$VTEC_{mean}$
1300 km	15.95	41.6	10.48	51082	38.24
Latitude 40^o	15.75	36.2	12.25	5047	43.54
$\sim$ 20000 km	16.40	42.9	11.21	51082	38.24
Latitude 40^o	16.42	37.7	13.15	5047	43.54

A.2.2 Results: Influence of the NeQuick plasmaspheric modeling

When considering the integration of the TEC along the receiver-satellite link, two integration heights have been chosen: on one hand, integrating up to the satellite current height and on the other hand, fixing the ceiling-height at 1300 km. This will give an assessment of the contribution of the plasmaspheric component of the NeQuick model to the final results. The STEC data used as input are from IGS maps in both cases.

The modeling of the plasmaspheric component (which is being improved by [Cueto et *al.* (2004)] has an influence in the performance: slightly better using NeQuick just to 1300 km (41.6%) in front of using to the GPS satellite height of 20200 km (42.9%).

A.2.3 Results: NeQuick model versus data driven model

Two quite different ionospheric modeling are compared: the Galileo baseline model (NeQuick fed with approximately 25 stations data, adequate for real-

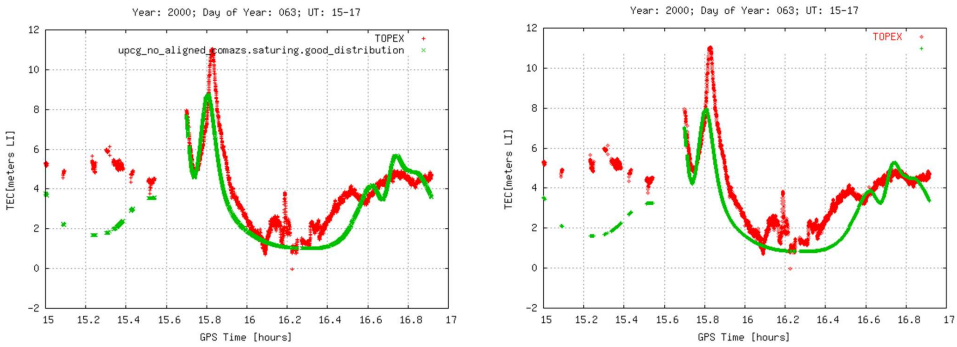

Figure A.4: *Ceiling-height at satellite position vs. TOPEX data and ceiling-height 1300 km vs. TOPEX data.*

Table A.3: *Results for the NeQuick model vs. IONEX. The RMS and BIAS are both expressed in TEC units (TECU).*

	RMS	% ERR	BIAS	Obs.	$VTEC_{mean}$
IONEX	11.34	29.4	-2.32	51082	38.24
Latitude 40^o	5.72	13.1	-2.11	5047	43.54
IGS good distribution	14.50	37.9	6.96	51082	38.24
Latitude 40^o	13.05	30.0	7.96	5047	43.54

time use) and the IGS ionosphere maps (computed only from GPS data, but including more than 100 stations, although not suitable nowadays for real-time use).

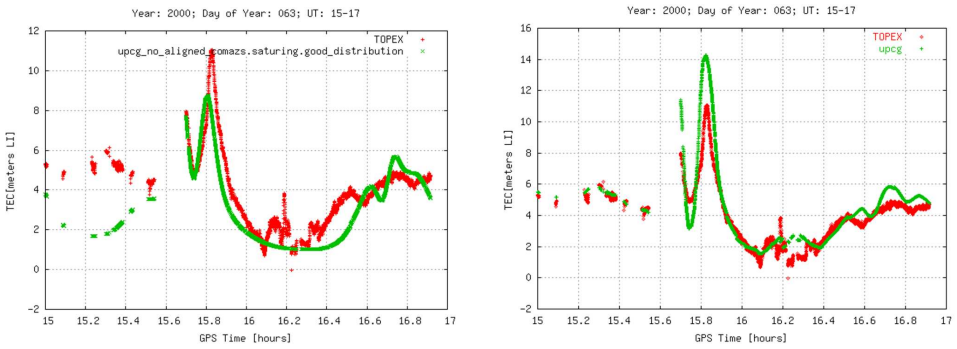

Figure A.5: *Uneven distribution vs. TOPEX data and IONEX vs. TOPEX data.*

The IGS ionosphere global maps show a better performance as it could

Table A.4: *Results for the NeQuick model vs. the Klobuchar model. The RMS and BIAS are both expressed in TEC units (TECU).*

	RMS	% ERR	BIAS	Obs.	$VTEC_{mean}$
IGS good distribution	14.50	37.9	6.96	51082	38.24
Latitude 40^o	13.05	30.0	7.96	5047	43.54
Klobuchar	15.63	40.9	5.98	51082	38.24
Latitude 40^o	11.78	27.0	-4.01	5047	43.54

be expected.

A.2.4 Results: NeQuick model versus Klobuchar model

The Klobuchar model is a so-called ionospheric single-layer model, meaning that the ionosphere is approximately reduced to an infinitesimal thin layer modelling the vertical electron content of the ionosphere (see Chapter 7). The model allows an approximation of the propagation delay for signals, which cross the ionosphere in vertical direction. At night times the delay is set to a constant value of 5 ns, at day times the delay is modelled by a cosine function of the local time. Amplitude and period of the cosine function are dependent on the geomagnetic latitude of the sub-ionospheric point. These quantities can be computed by the use of 8 coefficients uploaded daily to the satellites and broadcast to the user. A detailed description of the model can be found in the public GPS ICD document [Radicella and Leitinger (2001)]. The literature states that the Klobuchar model includes only 50 % of the ionospheric delays. The full algorithm for this ionospheric correction model Klobuchar is given by [Radicella and Leitinger (2001)].

The Klobuchar model broadcasted by the GPS navigation message provides worst results at global scale for the NeQuick approach shown: 41% in front of 38% of NeQuick (adjusted with 25 globally well distributed stations). On the other hand, the results for this day of study indicate that Klobuchar performs better for mid-latitudes.

A.2.5 Results: Alternative calculation of Az

An alternative way of optimizing Az is explored in this work, consisting on an independent optimization per each satellite-receiver link instead of one daily optimization. This procedure is faster in terms of calculation time.

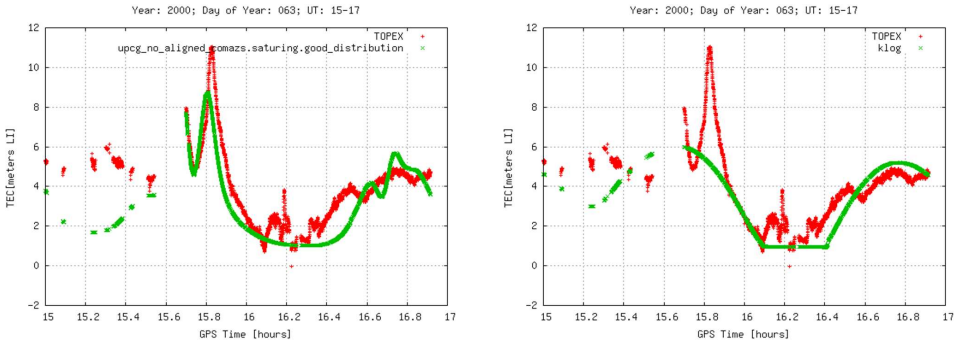

Figure A.6: *NeQuick vs. TOPEX data and Klobuchar vs. TOPEX data.*

Table A.5: *Results for the standard vs. ray-by-ray optimization procedures. The RMS and BIAS are both expressed in TEC units (TECU).*

	RMS	% ERR	BIAS	Obs.	$VTEC_{mean}$
Standard procedure	16.40	42.9	11.21	51082	38.24
Latitude 40^o	16.42	37.7	13.15	5047	43.54
Ray-by-ray optimization	16.67	43.6	11.59	51082	38.24
Latitude 40^o	16.79	38.6	13.63	5047	43.54

Table A.5 shows that it is slightly worst (43.6% in front of 42.9%). Nevertheless, this fast approach provides the capability to study the Az evolution in terms of local time (see Figure 8 for IGS -left- and IFAC -right- input STEC) in front of the global-per-station Az adjustment. It can be observed in Figure A.7 a quite compatible Az during the daytime and important discrepancies in the night. The three coefficients determining the Az variation with MODIP were designed to be broadcasted to the user in the navigation message updated at least once every 24 hours. The evolution of Az with local time in Figure A.7 could indicate the need to reduce the interval between broadcasts to 12 or even 6 hours.

A.2.6 Results: Influence of different input STECs sources

Two different input STEC reference have been compared: STEC values from IFAC and from IGS Ionospheric maps.

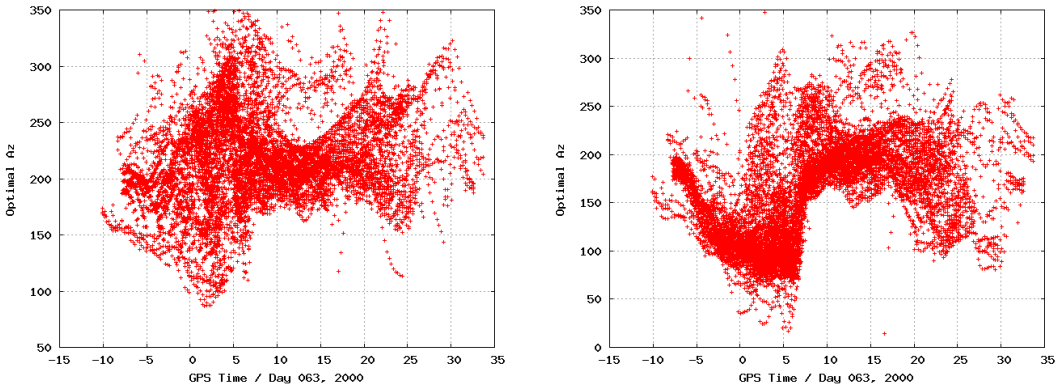

Figure A.7: *Az evolution in terms of local time (IGS and IFAC input reference STEC).*

Table A.6: *Results for IGS input STECs vs. IFAC input STECs. The RMS and BIAS are both expressed in TEC units (TECU).*

	RMS	% ERR	BIAS	Obs.	$VTEC_{mean}$
IGS input STECs	15.83	41.1	1.89	51082	38.24
Latitude 40^o	11.55	26.5	1.76	5047	43.54
IFAC input STECs	16.67	43.6	11.59	51082	38.24
Latitude 40^o	16.79	38.6	13.63	5047	43.54

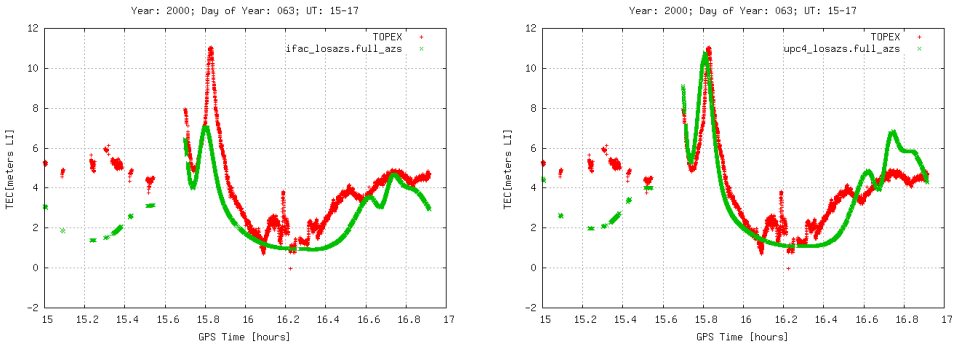

Figure A.8: *IFAC input STEC vs. TOPEX data and IGS input STEC vs. TOPEX data.*

The approach is sensitive to the input STECs: during this day, the IGS input STECs perform better from both the TOPEX vertical ionospheric and the differential ionospheric assessments as indicates A.9.

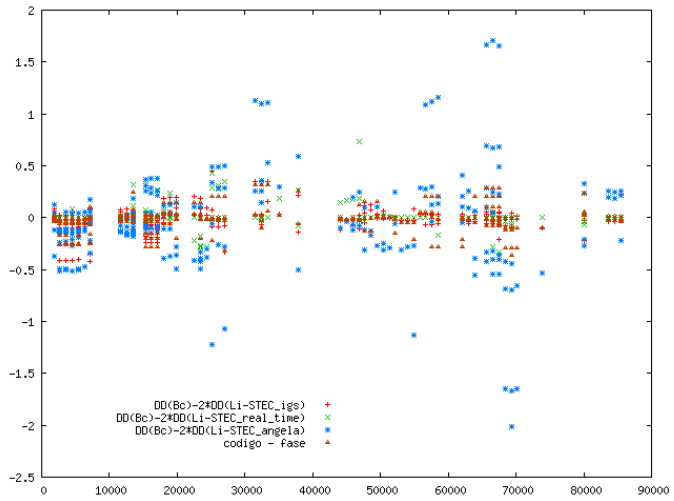

Figure A.9: *In blue, differential ionospheric error using IFAC STECs and, in red, differential ionospheric error using IGS IONEX STECs.*

A.3 Conclusions

The first results of the performance of the Galileo-like ionospheric corrections for single frequency users have been shown computed by adjusting the NeQuick model to ionospheric observations of different nature in a set of worldwide distributed GPS stations of the IGS network. The main performance metrics used have been the comparison to dual-frequency TOPEX altimeter observations. Such observations, gathered on the March 3^{rd}, 2000 under Solar Maximum conditions, are worldwide distributed over the oceans, and typically far from GPS stations. The main conclusions of this preliminary study are referred to the sensitivity of the quality of the Galileo-like ionospheric corrections to:

- The geographical distribution of the monitoring reference stations. The performance improves with a better globally geographical distribution of stations.

- Maximum allowable ceiling height: limiting it performs better, being compatible with the potential improvements to be done in the plasmaspheric NeQuick modeling reported by several authors.

- A certain explored NeQuick approach seems to perform slightly better than the Klobuchar model (with eight broadcasted coefficients) at

global scale, and worst than the only-data IGS ionospheric maps (computed from more than 100 receivers, instead of 25).

- Input STEC quality to adjust NeQuick (IGS Ionospheric Maps performs better for the selected day).

Furthermore, an alternative way of adjusting Az has been tested that could be useful for exploring the consistence of the daily Az adjustment approach, and open the possibility to a potential increase of the temporal resolution of the broadcast of the coefficients a_0, a_1, a_2. These performance tests and preliminary results (obtained from one single day of data) should be extended to a significant period of time. The study should consider the error from the user point of view, with the predicted a_0, a_1, a_2 values broadcasted for the following day.